Università degli Studi di Cagliari

DOTTORATO DI RICERCA

in Ingegneria Strutturale

Ciclo XXVII

TITOLO TESI

A New Class of Auxetic Lattices

Settore scientifico disciplinare di afferenza

ICAR/08 SCIENZA DELLE COSTRUZIONI

Presentata da:	Luigi Cabras
Coordinatore Dottorato:	Prof. Francesco Ragnedda
Tutor:	Prof. Michele Brun
Relatore:	Prof. Michele Brun

Esame finale anno accademico 2013 – 2014

Acknowledgements

I gratefully acknowledge M.I.U.R.(Ministero dell'Istruzione, dell'Università e della Ricerca) for the financial support of a PhD scholarship. I would like to thank the Department of Mathematical Sciences of the University of Liverpool for its hospitality during the research period abroad. I remember with affection the small Italian community in Liverpool, the Brun family, my friends Giorgio Carta, Felice Giaccu and Stewart Haslinger, now Italian by adoption. Special thanks go to my supervisor Prof. Michele Brun for his essential and permanent support during these three years, for the idea behind the research activity, its development and the careful contribution to the editing of this thesis.

Contents

List of Figures

List of Tables

Symbols

Roman symbols

Symbol	Name	Unit
A	Cross-sectional area of the crossbeam	$[mm^2]$
E^*	Effective Young's modulus of the lattice	$[N/mm^2]$
E	Young's modulus of the crossbeam material	$[N/mm^2]$
J	Second moment of inertia of the crossbeam	$[mm^4]$
k_L	Stiffness of the longitudinal spring	[N/m]
k_R	Stiffness of the rotational spring	[Nm/rad]
K^*	Effective bulk modulus of the lattice	$[N/mm^2]$
K	Bulk modulus of the crossbeam material	$[N/mm^2]$
$\mathbf{m}$	Direction vector	
M	Bending moment in the crossbeam	[Nm]
M^R	Spring moment	[Nm]
$\mathbf{n}$	Direction vector	
N	Axial force in the crossbeam	[N]
p	Length of arm of the crossbeam	[m]
S^L	Spring force	[N]
$\mathbf{S}$	Compliance matrix	
$\mathbf{t}$	Direction vector	

Greek symbols

Symbol	Name	Unit
α	Angle that identifies the type of planar lattice	[rad]
α_1	Dimensionless axial stiffness ratio parameter	
α_2	Dimensionless bending stiffness ratio parameter	
α_3	Dimensionless axial stiffness ratio parameter	
α_4	Dimensionless bending stiffness ratio parameter	
β	Polar angle that identifies $\mathbf{n}$	[rad]
β_1	Dimensionless anisotropy factor	
β_{cub}	Dimensionless Zener anisotropy factor	
γ	Angle characterizing the configuration of the lattice	[rad]
$\overline{\varepsilon}_{11}$	Macroscopic strain in x_1 direction	
$\overline{\varepsilon}_{22}$	Macroscopic strain in x_2 direction	
η	Dimensionless thermal ratio parameters	
θ	Angle that identifies $\mathbf{m}$	[rad]
λ_c	Coefficient of thermal expansion of the crossbeam material	[1/K]
λ_t	Coefficient of thermal expansion of the truss material	[1/K]
λ_A^*	Effective area coefficient of thermal expansion of the lattice	[1/K]
λ_L^*	Effective linear coefficient of thermal expansion of the lattice	[1/K]
μ^*	Effective shear modulus of the lattice	$[N/mm^2]$
μ	Shear modulus of the crossbeam material	$[N/mm^2]$
ν^*	Effective Poisson's modulus	$[N/mm^2]$
ν	Poisson's modulus of the crossbeam material	$[N/mm^2]$
ρ^*	Relative density of the lattice	
$\overline{\sigma}_{11}$	Macroscopic axial stress in x_1 direction	$[N/mm^2]$
$\overline{\sigma}_{22}$	Macroscopic axial stress in x_2 direction	$[N/mm^2]$
ϕ	Azimuthal angle that identifies $\mathbf{n}$	[rad]
ψ	Internal angle between the crossbeam of the lattice	[rad]
ω	Dimensionless area ratio	

Preface

The constitutive properties of material derive from its internal structure. Its internal structure refers to its crystal structure, at the atomic length scale, and to the micro-structure at the so called meso-scale. The meso-scale may range from $10^{-9}m$ to $10^{-2}m$ length scale for composite materials and micro electro-mechanical systems to $10^{0}m - 10^{1}m$ for civil engineering structures. At the microstructural level the behaviour is described with sufficiently good approximation by continuum and structural theories of mechanics (or thermo-mechanics) depending on the prevalent or combined continuum or discrete character of the micro-structure. Clearly the macroscopic behaviour depends on the constitutive behaviour of the single phases and on their distribution at the micro-structural level. The capability to create and design new type of micro-structures may lead to innovative macroscopic behaviours which can not be obtained by standard materials. When we speak about unusual properties we can think to those strange materials that when they are compressed they contract in the perpendicular direction. Quantitatively, this property is measured by a negative Poisson's ratio. Scientists have been aware of materials with negative Poisson's ratio for over a century, but only recently they have directed their attention to their study, motivated both by the curiosity about this unusual property and by their possible practical applications. The first article published about a synthetic auxetic material appeared in the journal Science in 1987, with the title 'Foam structures with a negative Poisson's ratio', see [1]. After this original article, which was a forerunner, these materials were called anti-rubber by J. Glieck of the New York Times, auxetic materials by K. Evans and co-workers in Exeter and F. Scarpa and co-workers in Bristol, they

were even called dilational materials by the mathematician G. Milton of the University of Utah. In the rest of the work when we refer to materials with negative Poisson's ratio we will call them 'auxetic materials'. There are many analytical and numerical models developed by researchers with the aim to describe auxetic existing materials or useful to propose new ones. The models we are going to propose make possible to obtain extreme values of Poisson's ratio, that is arbitrary close to -1 for isotropic materials. The organization of the thesis follows approximately what has been the development of the research. The thesis is divided in three chapters focused on different aspects of the mechanical and thermal behavior of auxetic lattices. The introduction of each chapter is dedicated to the presentation of the problem, that will be rigorously studied in the central body, and to a brief overview about existing models and possible engineering applications. In the first chapter we present three two-dimensional auxetic lattices, an hexagonal and a triangular ones with isotropic mechanical behavior, and a square one with cubic behavior. Their mechanical elastic moduli are given in analytical form and to conclude the chapter we report the experimental evidence that the Poisson's ratio of the square lattice subjected to an uniaxial tension approaches -1. Aware that a two-dimensional representation, although accurate, is a simplification of reality, we have extended our study to three-dimensional lattices in view of possible engineering applications. In the second chapter it is introduced a cubic micro-structure, that is based on the same principles of the plane square version. The three-dimensional lattice keeps the cubic behavior of the square plane lattice, the anisotropic elastic character of the material is reflected on the effective elastic moduli which depend on the direction. The results are given in numerical way, since an analytical approach was particularly complicated because of the difficulties introduced by the three-dimensionality of the problem. In the second part of the chapter the structure of the lattice is conveniently modified to guarantee an isotropic behaviour, maintaining a negative Poisson's ratio. In addition to have the unusual property of being auxetic, the proposed lattices, both the plane ones and the three-dimensional ones, have another unusual feature, they have a 'tailorable' coefficient of thermal expansion. Based on the geometrical configuration and on the characteristics of the constituent materials, the effective coefficient of thermal expansion of the lattices may be positive, null, or negative. This fact makes them particularly interesting from a practical point of view since the behavior of a structure, due to thermal changes, is a sensible problem in several engineering fields. In the third chapter a complete analytical analysis of the thermal response

of the lattices is given and an experiment on the hexagonal plane lattice, carried out at the laboratory for Physical Modeling of Structures and Photoelasticity of the 'University of Trento', proves the peculiarity to achieve negative coefficient of thermal expansion.

Chapter 1

Lattices with Negative Poisson's ratio

1.1 Introduction

Poisson's Ratio, usually represented by the lower case Greek ν, is defined as the ratio of transverse contraction strain to longitudinal extension strain with respect to the direction of stretching force applied.

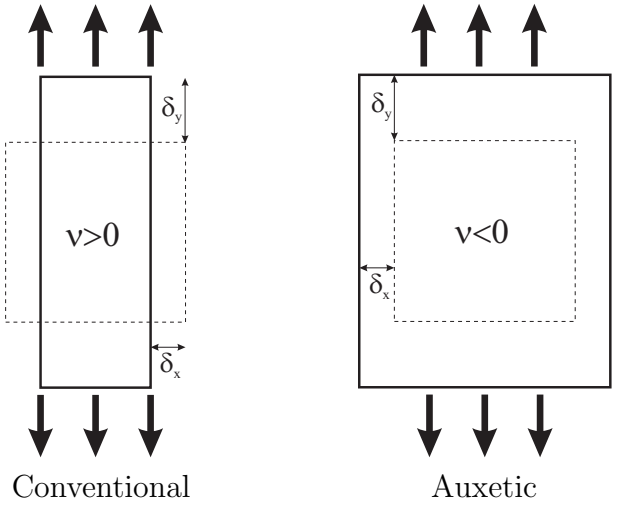

FIGURE 1.1: Scheme of Poisson's ratio mechanism. (a) Conventional material. (b) Auxetic material.

The definition of Poisson's ratio contains a minus sign, since tensile deformation is considered positive and compressive deformation is considered negative, so that

normal materials have a positive Poisson's ratio. Although normal materials contract when they are stretched there are particular materials that expand laterally when stretched longitudinally showing a negative Poisson's ratio, they are usually named 'auxetic materials'. The term 'auxetic' comes from the Greek word '$\alpha\upsilon\xi\epsilon\sigma\iota\zeta$' (auxesis: increase, grow) and was first used by K. Evans et al. [2] (see also [3]), when they first fabricated the micro-phorous polyethylene with negative Poisson's ratio, to indicate materials that expand in the direction perpendicular to the applied tensile stress, and contract for perpendicular compressive stress. For isotropic materials may be shown that $-1 \leq \nu \leq \frac{1}{2}$ in three dimension and $-1 \leq \nu \leq 1$ in two dimension, instead the values of ν for anisotropic materials could be beyond the limits of isotropic materials. The Poisson's ratio ν has also important consequences for other aspects of the behavior of materials, it is an indication of the mechanical property of a medium to deform mainly deviatorically or isotropically, as described by the ratio K/μ of the bulk to the shear modulus, ranging from a so-called 'rubbery' behaviour at the upper limit of ν to a 'dilatational' behaviour at the lower limit of ν [4]. Usually the most materials resist a change in volume as determined by the bulk modulus K more than they resist a change in shape, as determined by the shear modulus μ, the values of K are typically larger than the values of μ. By changing the micro-structure of a material in such a way that the Poisson's ratio ν is lower, the values of K and μ can be altered if the Young's modulus E is kept constant. Naturally, decreasing the value of ν to zero or below would result a high shear modulus μ relative to the bulk modulus K that can be obtained. The relations, for isotropic material, between E, μ,K, and ν are as follows:

$$K = \frac{E}{2(1-\nu)} \quad \text{in 2D, and} \quad K = \frac{E}{3(1-2\nu)} \quad \text{in 3D} \tag{1.1a}$$

$$\mu = \frac{E}{2(1+\nu)} \quad \text{in 2D and 3D .} \tag{1.1b}$$

Combining previous eqns. (1.1), the following is obtained:

$$\frac{3K}{2\mu} = \frac{1+\nu}{1-2\nu} \quad \text{in 2D, and} \quad \frac{K}{\mu} = \frac{1+\nu}{1-\nu} \quad \text{in 3D.} \tag{1.2}$$

A graphical depiction of this relationship is shown in Fig. 1.2:

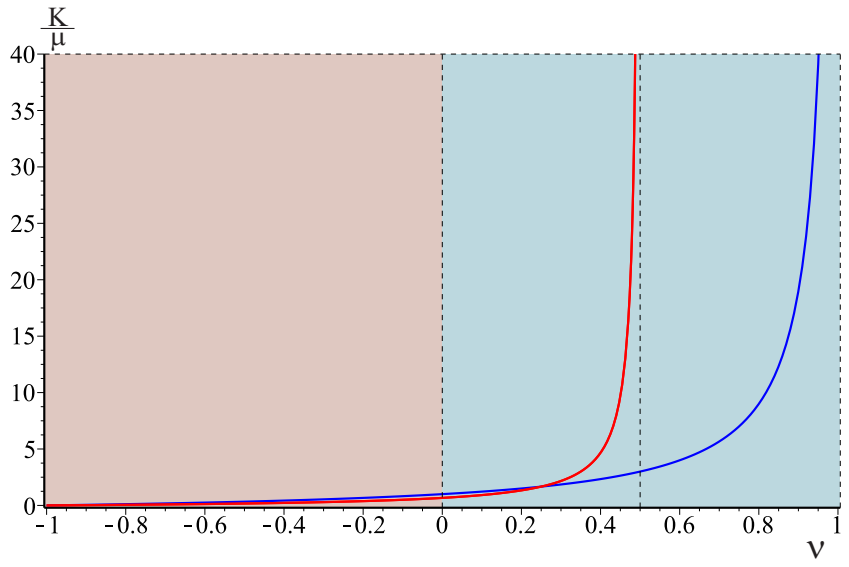

FIGURE 1.2: Relation between K, μ and ν.

To have the Poisson's ratio $\nu < 0$ in 3D, the value of the bulk modulus must be less than the shear modulus. Rubber, most liquids and granular solids are almost incompressible ($K/\mu \gg 1$, $\nu \to 1/2$), while examples of extremely compressible materials ($K/\mu \ll 1$, $\nu < 0$) are re-entrant foams [1, 5] and several molecular structures [6, 7, 8]. Materials with negative Poisson's ratio are important in practical applications for civil and aeronautical engineering, defence equipments, smart sensors, filter cleaning and biomechanics; in recent years the number of patent applications and publications has increased exponentially. Auxetic systems perform better than classical materials in a number of applications, due to their superior properties. They have been shown to provide better indentation resistance [9, 10, 11]; the material flows in the vicinity of an impact as a result of lateral contraction accompanying the longitudinal compression due to the impact loading. Hence the auxetic material densifies in both longitudinal and transverse directions, leading to increase indentation resistance, as schematically shown in Fig. 1.3. This behavior has also been correlated to the atomic packing [12], which has been found to be proportional to the Poisson's ratio, and to the densification mechanism under high contact pressure [13]. In an isotropic material, indentation resistance is roughly proportional to the ratio $E/(1-\nu^2)$, E is the Young's modulus and ν the Poisson's ratio, meaning that the resistance can be strongly increased, even with respect to an incompressible material, when the Poisson's ratio is below $-1/2$. Resistance to damage is also associated with the capacity of negative Poisson's ratio materials to distribute internal energy over a larger region

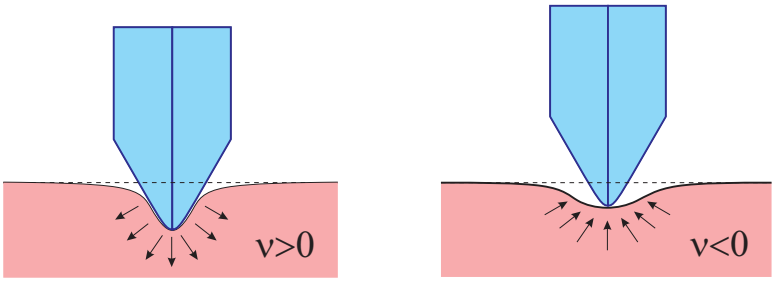

FIGURE 1.3: Indentation resistance.

as opposed to common materials which, in presence of stress concentrators as point forces or geometrical singularities, accumulate internal energy in a neighborhood of the concentrator leading to possible damage of the material and consequent failure. Compared with conventional materials, auxetic materials have increased fracture toughness, showing high crack resistance, because they expand and close up the crack when being pulled apart. If we consider the critical tensile stress for fracture of a solid of surface tension T with a plane circular crack of radius r, it is proportional to $\pi ET/(2r(1-\nu^2))$. So when ν approaches -1 the material becomes very tough. In this sense, auxetic materials can be applied to improve protective materials or energy absorbing materials [14]. Furthermore, they can be also applied as a efficient membrane filter with variable permeability [15, 16], fasteners [17, 18], shape memory materials [19] and acoustic dampeners [20, 21]. They have the ability to form dome-shaped structures when bent [1, 22] undergoing double (synclastic) curvature, as opposed to the saddle shape (anticlastic curvature) that non-auxetic materials adopt when subject to out-of-plane bending moments, as shown in Fig. 1.4. Another useful example to illustrate the benefits

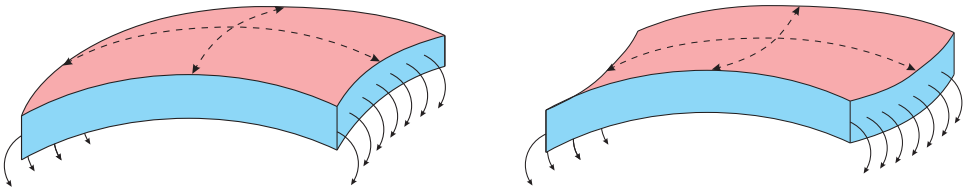

FIGURE 1.4: Synclastic curvature and anticlastic curvature in structure subjected to bending.

of the control of the Poisson's ratio, and in particular to have values close to -1, is shown schematically in Fig. 1.5. It depicts a fixed axisymmetric plate subject

to a concentrated load and to a distributed load. The deflection d of the plates depends on the Poisson's ratio, indeed:

$$\begin{aligned} d &= \frac{3(1-\nu^2)}{4\pi}\frac{Pr^2}{Eh^3} && \text{for concentrated load,} \\ d &= \frac{3(1-\nu^2)}{16}\frac{qr^4}{Eh^3} && \text{for distributed load,} \end{aligned} \tag{1.3}$$

and in particular when ν tends to -1 it tends to zero.

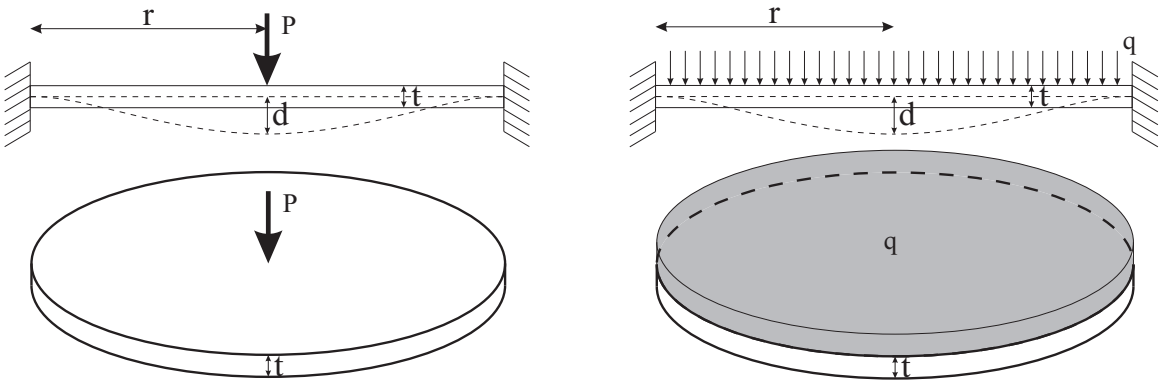

FIGURE 1.5: Deflection of a fixed axisymmetric plate subjected to a concentrated load or a distributed load

Furthermore, auxetic materials have better acoustic and vibration properties over their conventional counterparts [23, 24, 25, 26]. We can summarize in Table 1.1 some applications with the respective fields.

Area	**Applications**
Medical	Bandage, wound pressure pad, dental floss, artificial blood vessel, drug delivery, surgical sutures
Industry	Shock absorber, sound absorber, packaging materials, fishnet, stress decay, reinforcement fibers, seat cushions, filter fastener
Sensors and actuators	Piezoelectric devices, sensor
Aerospace	Curved body part, aircraft nose-cones, wing panels
Protection	Crash helmet, bullet proof vest,protective clothes, car bumpers, shin pad, knee pad

TABLE 1.1: Engineering applications of auxetic materials.

There are several natural materials that have been discovered to possess negative Poisson's ratio: iron pyrites [27], arsenic and bismuth [28], cadmium [29], several cubic and face-centered cubic rare gas solids along a specific crystallographic direction [7] and also biomaterials such as cow teat skin [30] and load-bearing cancellous bones [31].

Conceptually auxetic structures have been known since 1944 [27], but the first artificial experimental samples concerning a re-entrant structures, firstly proposed by Almgren [32] and Kolpakov [33], were presented in 1987 by Lakes [1]. Since then, different geometrical structures and models were proposed and analyzed trying to reproduce some observed features in auxetic materials, ranging from the macroscopic to microscopic and to the molecular levels. Extended reviews can be found in [34, 35, 36], here we give particular attention to the most interesting models in term of mechanics. Their classification is based on mechanical considerations, almost all of them are based on a simple mechanism that is treated as a unit cell leading to a global stiffening effect. Among the most important classes of such auxetic structures there are:

- 2 and 3 D re-entrant structures
- chiral structures
- rotating rigid/semi-rigid units
- angle-ply laminates
- hard molecules
- microporous polymers and liquid crystalline polymers

One of the earliest models used to describe these special materials, is based on re-entrant structures. In fact the macroscopic auxetic cellular structures in the form of two-dimensional re-entrant honeycombs were firstly suggested by Gibson et al.(1982). The adjective re-entrant here means an angle in a polygon greater than 180^o and thus pointing inwards, as shown in Fig. 1.6(a). A traditional two-dimensional re-entrant model used to describe the behaviour of foams with conventional and auxetic honeycombs is shown in Fig. 1.6, and the Poisson's ratio is given by:

$$\nu = \frac{\sin(\theta)(\frac{h}{l} + \sin(\theta))}{\cos^2(\theta)} \tag{1.4}$$

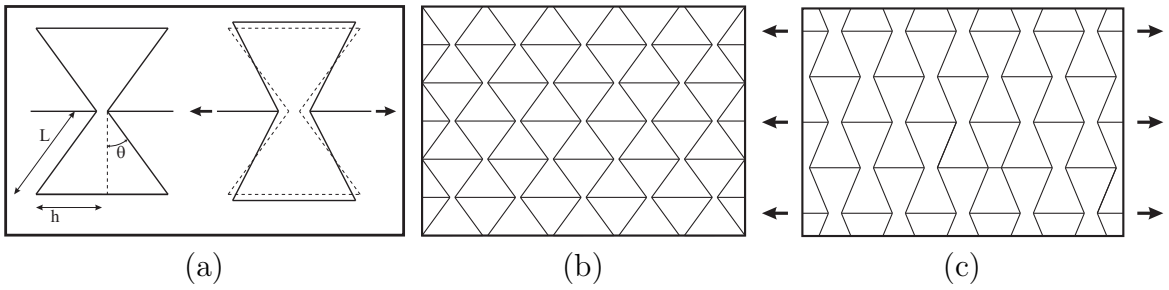

FIGURE 1.6: Scheme of re-entrant structure by Gibson and Ashby [37]. (a) Hexagonal re-entrant unit cell. (b) Hexagonal re-entrant lattice. (c) Expanded hexagonal re-entrant lattice.

Over the years, many more sophisticated models have been proposed [37, 38, 39, 40, 41, 42, 43, 44, 45, 46]). Fig. 1.7 shows two idealised networks of cells: an 'intact' version, Fig. 1.7(b), and a 'cut' version, Fig. 1.7(c), with some ribs removed or broken.

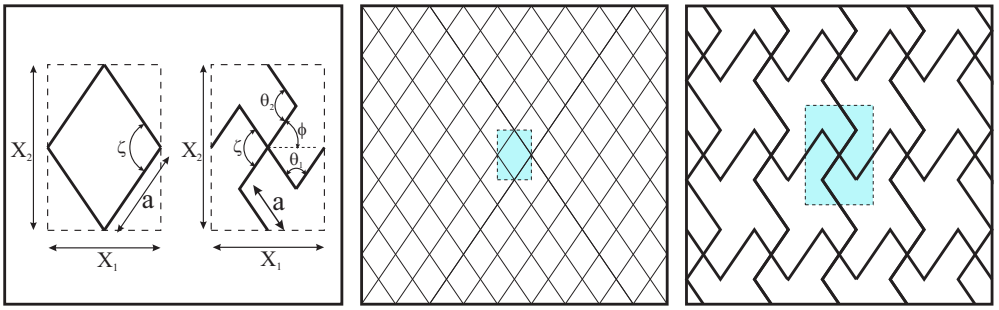

FIGURE 1.7: Scheme of re-entrant structure by Smith et al. [47]. (a) Conventional and re-entrant unit cells. (b) Intact lattice. (c) Cut lattice.

In the intact version the cells deform by hinging at the base of the ribs, and the ribs do not flex or stretch; furthermore the cell with four intact ribs is much stiffer than the other one. Thus the intact unit cell deforms solely through a change in the ζ, whereas in the unit cell of the cut version the joints with angle θ_i, with $i = 1, 2$ are spring hinges with spring constants $k\theta_i$ which are such that $k\zeta >> k\theta_i$. Thus we may assume that when the network is loaded in the OX_i direction it deforms solely through changes in the θ_i angles and the unit cell remains rectangular. The value of Poisson's ratio, for the two cases, is given by:

$$\begin{aligned} \nu &= \tan^2(\frac{\zeta}{2}) && \text{for intact version,} \\ \nu &= -\tan(\phi)\tan(\zeta - \phi) && \text{for cut version.} \end{aligned} \tag{1.5}$$

Another model based on a chiral structure was proposed by Prall and Lakes [48], the researchers in this area use the adjective 'chiral' to mean a physical property to spin. In this kind of structures, the basic unit is formed by connecting straight ligaments to central nodes which may be circles or rectangles or other geometrical forms. The whole chiral structures are then formed by joining together the chiral units. The auxetic effects are achieved through wrapping or unwrapping of the ligaments around the nodes in response to an applied force. According to the theoretical and experimental investigations performed by Prall and Lakes, the Poisson's ratio ν of a chiral structure for in-plane deformations, with flexible ribs and rigid node, can be tailored to be around -1. The model is summarized in Fig. 1.8,

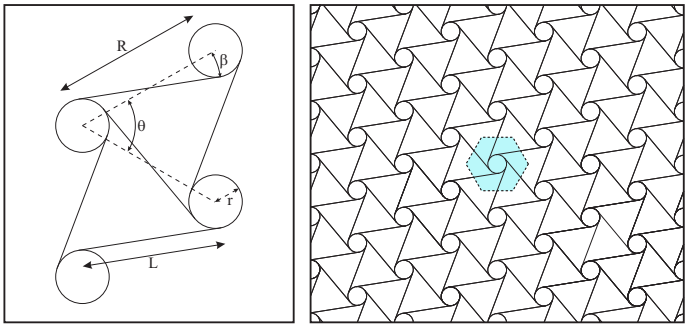

FIGURE 1.8: Chiral structure proposed by Prall and Lakes in [48]

and its Poisson's ratio can be calculated as:

$$\nu = \frac{4(t/L)^2}{(t/L)^4 \cos^2\beta + 1 - \cos^2\beta + 3(t/L)^2} - 1 \tag{1.6}$$

More recently, Ruzzene and Spadoni have considered the behavior of such chiral structures by introducing the flexibility of the nodes. Its static and dynamic behaviour has been studied in the context of the generalized micro-polar theory of elasticity [49, 50, 51]. Other models, see for example [52, 53, 54], derive the auxetic behavior by the rotation of rigid or semi-rigid shapes (triangle, squares, rectangles and tetrahedron) when loaded, in Fig. 1.9(a) the case of equilateral triangle; this kind of structures has been developed to produce the auxetic behaviour in micro- and nano-structures; three-dimensional models in the linear [55, 56] and non linear [57] regimes were also proposed. For a model made with isosceles triangles, shown in Fig. 1.9(b), Poisson's ratio is:

$$\nu = \frac{b\cos(\alpha + \frac{\theta}{2}) + a\cos(\frac{\theta}{2})}{\tan(2\alpha + \frac{\theta}{2})b\sin(\alpha + \frac{\theta}{2}) + a\sin(\frac{\theta}{2})} \tag{1.7}$$

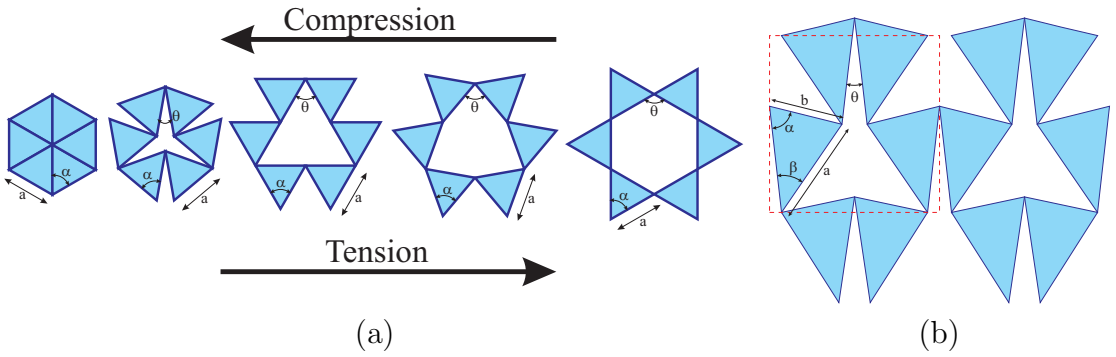

FIGURE 1.9: Rotating triangular models by Grima et al. [52, 53]. (a) Auxetic lattice made with equilateral triangles. (b) Unit cell made with isosceles triangles.

A different approach is followed in [58, 59, 60], Bathurst and Rothenburg formulate the incremental response of an assembly of elastic spheres from an isotropic distribution of contacts around a particle, while Wojciechowski suggested that solids consisting of non-convex hexagonal molecules may be auxetic. They modelled a linear elastic contact problem between two spheres, considering the two forces: $f_n = k_n d_n$ e $f_t = k_t d_t$, where $\mathbf{f}$ is the force between two contacting spheres due to relative displacement d of their centres, and n and t indicate normal and tangential components respectively. The parameters k_n and k_t are then the normal and tangential linear elastic constants and the interaction ratio λ, is defined by $\lambda = k_t/k_n$. The Poisson's ratio of such assembly is:

$$\nu = \frac{1-\lambda}{3+\lambda} \quad \text{in 2D, and} \quad \nu = \frac{1-\lambda}{4+\lambda} \quad \text{in 3D.} \tag{1.8}$$

When λ increases above unity the Poisson's ratio becomes negative. Koenders in [61], evaluated the Poisson's ratio in case of non isotropic distribution of the spheres, and he obtained:

$$\nu = \frac{(1-\lambda)\sin^2 2\psi}{4\cos^4\psi + \lambda \sin^2 2\psi}, \tag{1.9}$$

where ψ is the internal angle between the spheres. In Fig. 1.10, from the Gaspar's work [62], it is shown a unit cell that is designed to act as a circular disc with the desired interaction ratio of $\lambda > 1$. The five black arms are the five mechanically active components; everything else is designed to be comparatively rigid.

The auxetic behavior can be achieved at a macroscopic or micro-structural level, or even at the meso-scopic and molecular levels, models were developed to simulate

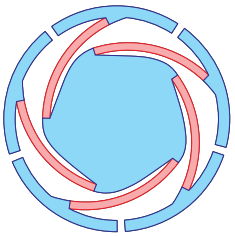

FIGURE 1.10: Granular structure by Gaspar [62]

polymeric structure or anisotropic fibrous composites. The first auxetic microporous polymeric material was investigated by Evans and Caddock (1989), see [63]. It was an expanded form of PTFE (Polytetrafluoroethylene), which has a highly anisotropic behaviour with $\nu = -12$ in particular directions. The auxetic effect is due to its complex micro-structure which consists of nodules interconnected by fibrils. If a tensile load is applied, the fibrils cause lateral nodule translation through their rotations, leading to a negative Poisson's ratio. The characteristics of this type of structure can be interpreted by a simple two-dimensional model, as shown in Fig. 1.11:

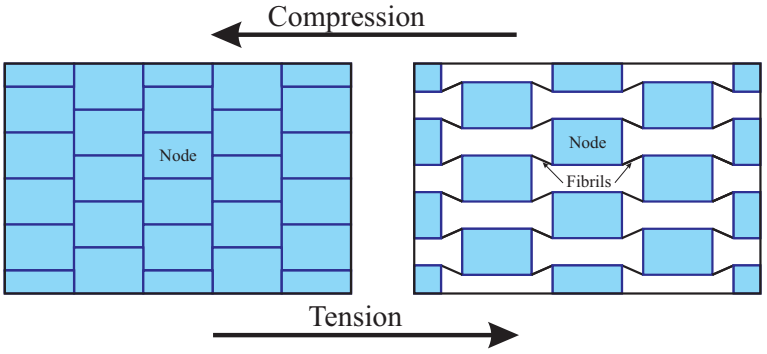

FIGURE 1.11: Scheme of polymeric structure undergoing tensile loading, by Liu and Hu [64]

Several cases of negative Poisson's ratios have been discovered in the analysis of anisotropic fibrous composites. In some laminates composed of fibrous layers it is theoretically possible to achieve a negative Poisson's ratio as small as -0.21 in the direction perpendicular to the layers by control of the stacking sequence. In other laminates, one can achieve a negative Poisson's ratio in some directions in the plane of the laminate, again by control of the stacking sequence. In these composites there is a high degree of anisotropy and the negative Poisson's ratio only occurs in some directions; in some cases only over a narrow range of orientation angle between the applied load and the fibers. In [65] a negative Poisson's ratio effect

is possible in composite where the inclusions have a star-like shaped cross section with sides containing re-entrant corners, as in Fig. 1.12.

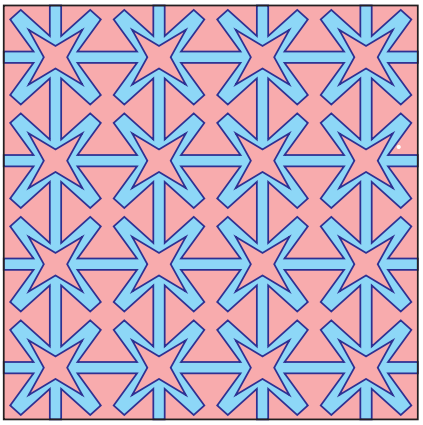

FIGURE 1.12: Periodic fiber-reinforced composite with star-shaped encapsulated inclusions proposed by Theocaris et al. [65].

Lakes [66] has presented innovative hierarchical laminate structures which give rise to intentional negative Poisson's ratios combined with mechanical isotropy in two dimensions or in three dimensions. By appropriate choice of constituent properties one can achieve Poisson's ratios approaching the lower limit of -1. A different approach, than those seen, uses topology optimization [67, 68, 69] and periodic tessellation [70] to obtain auxetic micro-structures. There are less examples of auxetic materials with continuous micro-structure: the design of a family of two-dimensional, two-phase composite with Poisson's ratios arbitrarily close to -1 is given in [4]. Successively, in the seminal paper [71], it is shown that every combination of positive-definite effective constitutive tensor can be obtained from a two-phase composite and particular attention is given to multi-rank laminates. In that paper the important concept of $n-$mode materials, indicating the number of easy modes of deformation, is also introduced; such a concept has strict analogies with the number of degrees of freedom in a mechanism of partially constrained structure, which is common in structural mechanics. After this brief review of the most common models proposed in literature, in this chapter we introduce a novel lattice family with three different realizations that leads to a Poisson's ratio arbitrarily close to the thermodynamic limit corresponding to $\nu = -1$. The effect is achieved by the superposition of clockwise and anti-clockwise internal rotations leading to a macroscopic non-chiral effect. In Section 1.2 we detail the kinematic of the mechanical system for three types of periodic lattices and in Section 1.3 we determine analytically the macroscopic constitutive properties of these structures.

The dependence of the effective properties on the constitutive and geometrical parameters of the micro-structure is presented in Section 1.4 and a comparative analysis with hexagonal, triangular and square honeycombs is also performed. Lastly in Section 1.5 we present experimental evidence of the negative Poisson's ratio $\nu = -0.9931 \pm 0.0025$ achievable.

1.2 Model of periodic lattice with auxetic macroscopic behavior

The micro-structured media fall within the class of uni-mode materials as shown in [71], [72] (Chap. 30) and [73, 74]. In our plane linear elastic systems a single eigenvalue of the effective elasticity matrix is very small (approaching zero) and the other two are very large. As common to all isotropic and cubic materials having Poisson's ratio approaching -1 the only easy mode of deformation is the dilatation (plane dilatation in a two-dimensional system). Here, we focus on three affine materials, two isotropic and one cubic, presented in Section 1.1. The kinematic analysis of a single radially foldable structure is used to determine the Poisson's ratio of the perfect lattice and its class. Here we use the term perfect to indicate that the lattice is composed of rigid elements.

1.2.1 Kinematic of radially foldable structure

We consider the angulated element $\overline{ABC}$, shown in grey in Fig. 1.13. This element represents two arms of a single cross-shaped structure that will be assembled with a second one to create the unit cell. The rigid element $\overline{ABC}$ is supposed to roto-translate with a single degree of freedom where A moves along the Ox_1-axis and C moves along the axis inclined by the angle α with respect to the Ox_1-axis. In analysing the trajectory of the central point B, we also follow the more general formulation given in [75, 76]. In Fig. 1.13, p is the length of the two arms, ψ the internal angle between them and α is the angle between the two straight lines along which the points A and C are constrained to move. B is the 'coupler' point of the linkage. The equation for the one-parameter trajectory followed by the point B is obtained by fixing the values of the geometric variables p, ψ, α; then, the position of B is determined by the angle γ.

The coordinates of points A, B and C are (see Fig. 1.13)

$$\begin{aligned} A &\equiv (x_1 - p\cos\gamma,\, x_2 - p\sin\gamma), \quad B \equiv (x_1,\, x_2), \\ C &\equiv (x_1 + p\cos(\pi - \psi + \gamma),\, x_2 + p\sin(\pi - \psi + \gamma)). \end{aligned} \tag{1.10}$$

Then, the 'coupler' point B is constrained to move within the rotated ellipse

$$C_1 x_1^2 + C_2 x_2^2 + C_{12} x_1 x_2 + C = 0, \tag{1.11}$$

where

$$\begin{aligned} C_1 &= p^2 \tan^2 \alpha, \\ C_2 &= p^2 \left(2 + \tan^2 \alpha - 2\cos\psi + 2\tan\alpha \sin\psi\right), \\ C_{12} &= -2p^2 \left(\tan^2 \alpha \sin\psi - \tan\alpha \cos\psi + \tan\alpha\right), \\ C &= -p^4 (\tan\alpha \cos\psi + \sin\psi)^2. \end{aligned} \tag{1.12}$$

Note that, for a single linkage, angles α and ψ are independent.

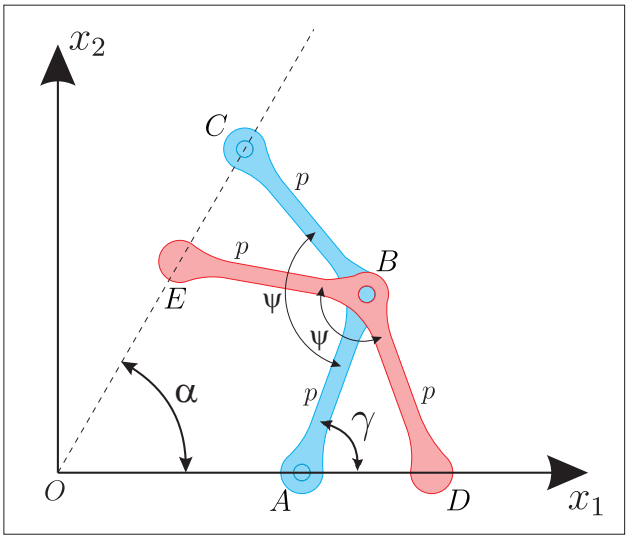

FIGURE 1.13: Pair of linkages movable with a single degree of freedom γ. The two rigid linkages $\overline{ABC}$ and $\overline{EBD}$ are shown in red and blue, respectively. They are constrained at the 'coupler' point B to have the same displacement. Points A and D and E and C can only move along straight lines.

When we couple the movement of the linkage $\overline{ABC}$ with the linkage $\overline{EBD}$, we obtain a relation between angles α and ψ. The two linkages share the same coupler curve (1.11) at their common point B at which they are connected by means of a hinge. This implies the condition

$$\alpha = \pi - \psi. \tag{1.13}$$

Consequently, in the trajectory equation (1.11)

$$C_1 = p^2 \tan^2\psi, \quad C_2 = p^2\frac{(1-\cos\psi)^2}{\cos^2\psi},$$
$$C_{12} = -2p^2\left(1-\frac{1}{\cos\psi}\right)\tan\psi, \quad C = 0, \tag{1.14}$$

yielding

$$x_2 = \frac{\sin\psi}{1-\cos\psi}x_1. \tag{1.15}$$

The common coupler curve for the two linkages is aligned with the radial line $\overline{OB}$ and to avoid crossover with other pairs in a polar arrangement of the fully radially foldable linkage the angle γ has to satisfy the bounds

$$\alpha - \eta \leq \gamma \leq \pi - \eta, \tag{1.16}$$

where $\eta = B\widehat{A}C = B\widehat{D}E = (\pi-\psi)/2$.

We consider three geometries: hexagonal ($\alpha = \pi/3$) Fig. 1.14(a), square ($\alpha = \pi/2$) Fig. 1.14(b) and triangular ($\alpha = \pi/6$) Fig. 1.14(c). The two-arms linkages are assembled in order to create radially foldable structures. Different configurations are shown in Figs.1.14(d)-(f), for the hexagonal, square and triangular structures, respectively; the 'coupler' point for each pair of linkages moves radially and the corresponding Poisson's ratios are equal to -1. The relative position of the point B with respect to the centre O of the structure, shown in the right column of Figs.1.14(d)-(f) as a function of the angle parameter γ, shows that the maximum volumetric expansion increases when we move from the triangular to the square and, then, to the hexagonal case.

1.2.2 Construction of periodic lattice

The two-arms linkages presented in Section (1.2) are assembled in order to create the kinematically compatible periodic structures shown in Fig. 1.15. The micro-structures are composed of cross-shaped elements with arms of the same length. The number of arms in each cross-shaped element are 3, 4 and 6 for the hexagonal, square and triangular geometries, respectively. A couple of cross-shaped elements is built where the two crosses are disposed in two different planes; in Fig. 1.13 they are indicated in blue and red. Each couple is mutually constrained to have

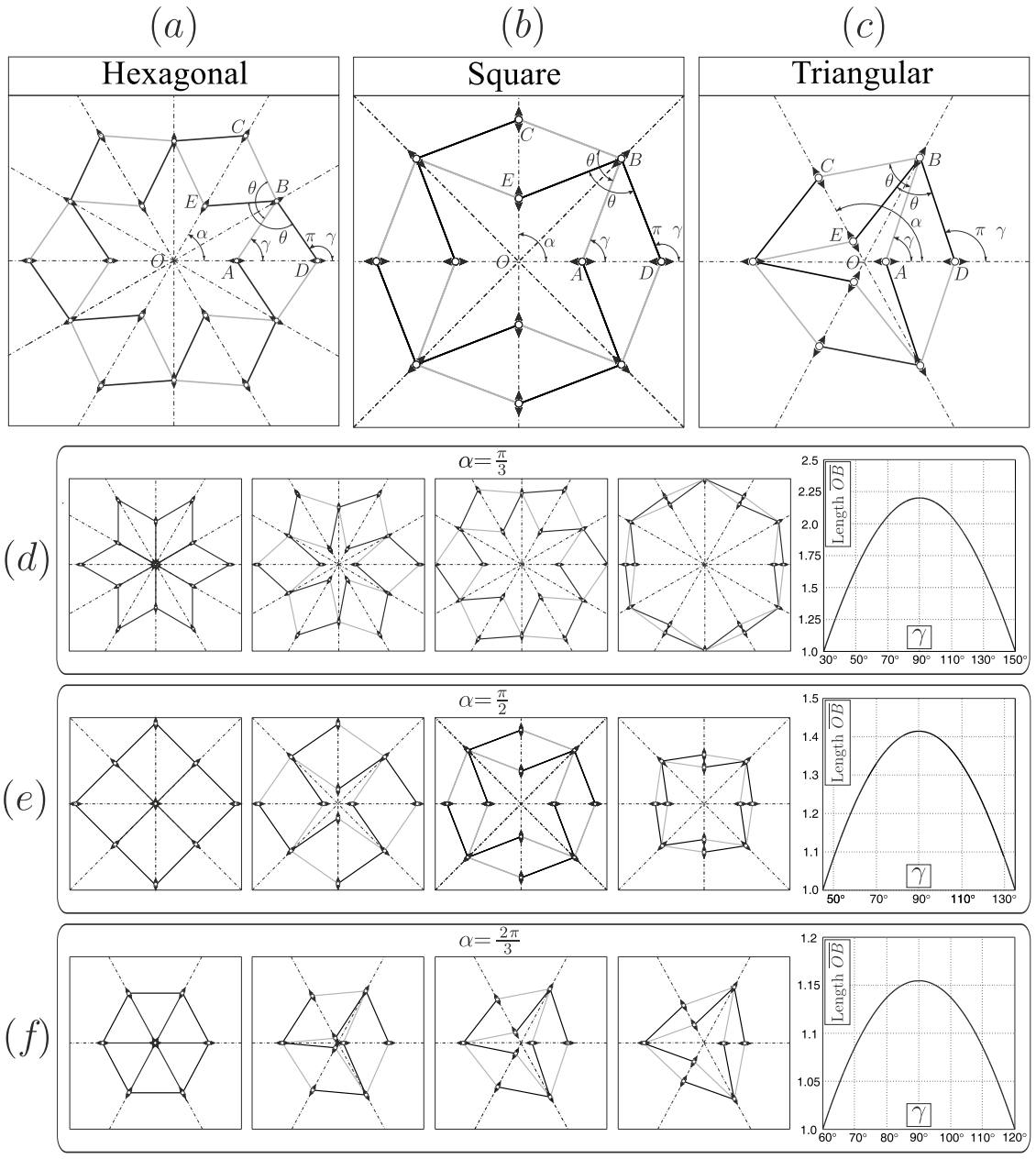

FIGURE 1.14: Radially foldable structures. The Poisson's ratio is equal to -1. (a) $\alpha = \pi/3$, hexagonal structure composed of six couples of rigid two-arms linkages. (b) $\alpha = \pi/2$, square structure. (c) $\alpha = 2\pi/3$, triangular structure. (d-f) Configurations of the single degree of freedom unit cells at different values of the geometrical parameter γ for the hexagonal, square and triangular structures, respectively. The radial distance $\overline{OB}$ ($p = 1$) as a function of γ is also given.

the same displacement at the central point where a hinge is introduced. Different couples are then constrained by internal hinges at the external end of each arm. In the next section we will also introduce some springs to provide stability of the constitutive behaviour.

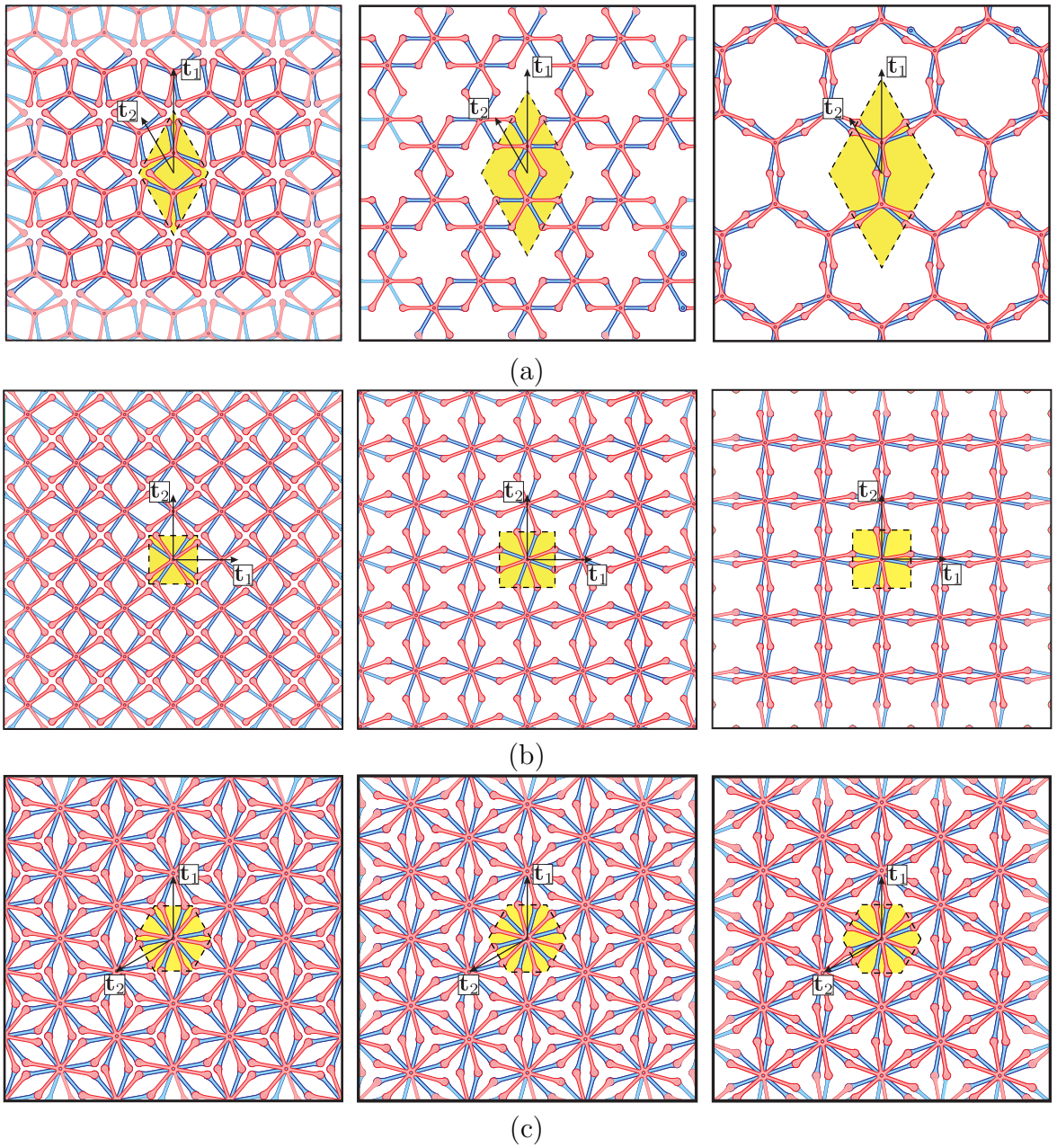

FIGURE 1.15: Periodic micro-structures. (a) Hexagonal, (b) square and (c) triangular geometries. Three different configurations, for different values of γ, are shown for each geometry. The unit cells are also indicated. The yellow dashed regions are the unit cells of the Bravais lattice where $\mathbf{t}_1$ and $\mathbf{t}_2$ are the primitive vectors.

The periodic structures have a Bravais periodic lattice [77] consisting of points

$$\mathbf{R} = n_1\mathbf{t}_1 + n_2\mathbf{t}_2 \tag{1.17}$$

where $n_{1,2}$ are integers and $\mathbf{t}_{1,2}$ the primitive vectors spanning the lattice. The three different geometries described in Fig. 1.15 correspond to the fundamental centered rectangular (rhombic), square and hexagonal Bravais lattices, respectively. We note that a micro-structure similar to the square lattice was proposed by O. Sigmund in [68]. In [68] the micro-stuctured media was obtained following an optimization procedure. Following the systematic analysis for finite deformation as in [73, 74] we show here that the lattice is a uni-mode material. Let

$$\mathbf{T} = \begin{bmatrix} \mathbf{t}_1 & \mathbf{t}_2 \end{bmatrix} \tag{1.18}$$

be the 'lattice matrix'. During the deformation the primitive vectors undergo an affine transformation and the matrix $\mathbf{T}$ describes a motion starting at $t = t_0$, with $\gamma(t_0) = \gamma_0$. At time t the deformation gradient is described by

$$\mathbf{F}(t, t_0) = [\mathbf{T}(t)][\mathbf{T}(t_0)]^{-1} \tag{1.19}$$

and the associated Cauchy-Green tensor is a path

$$\mathbf{C}(t, t_0) = [\mathbf{F}(t, t_0)]^T[\mathbf{F}(t, t_0)] = [\mathbf{T}(t_0)]^{-T}[\mathbf{T}(t)]^T[\mathbf{T}(t)][\mathbf{T}(t_0)]^{-1} \tag{1.20}$$

beginning at $\mathbf{C}(t_0, t_0) = \mathbf{I}$. Note that any other possible Bravais lattice is associated with the same path (1.20).

In particular we have the following cases.

- Hexagonal lattice (rhombic Bravais lattice as in Fig. 1.15(a)):

$$\mathbf{T}(t) = p\,\sin\gamma \begin{pmatrix} 0 & -\sqrt{3} \\ 6 & 3 \end{pmatrix}, \quad \mathbf{T}(t_0) = p\,\sin\gamma_0 \begin{pmatrix} 0 & -\sqrt{3} \\ 6 & 3 \end{pmatrix}, \tag{1.21}$$

  and

$$\mathbf{C}(t, t_0) = \left(\frac{\sin\gamma}{\sin\gamma_0}\right)^2 \mathbf{I}. \tag{1.22}$$

- Square lattice (square Bravais lattice as in Fig. 1.15(b)):

$$\mathbf{T}(t) = 2\,p\,\sin\gamma\,\mathbf{I}, \quad \mathbf{T}(t_0) = 2\,p\,\sin\gamma_0\,\mathbf{I}. \tag{1.23}$$

and

$$\mathbf{C}(t, t_0) = \left(\frac{\sin\gamma}{\sin\gamma_0}\right)^2 \mathbf{I}. \tag{1.24}$$

- Triangular lattice (hexagonal Bravais lattice as in Fig. 1.15(c)):

$$\mathbf{T}(t) = 2\,p\,\sin\gamma \begin{pmatrix} 0 & -\sqrt{3}/2 \\ 1 & -1/2 \end{pmatrix}, \; \mathbf{T}(t_0) = 2\,p\,\sin\gamma_0 \begin{pmatrix} 0 & -\sqrt{3}/2 \\ 1 & -1/2 \end{pmatrix} \tag{1.25}$$

and

$$\mathbf{C}(t, t_0) = \left(\frac{\sin\gamma}{\sin\gamma_0}\right)^2 \mathbf{I}. \tag{1.26}$$

Then, we conclude that the three materials are unimode, since the possible paths $\mathbf{C}(t, t_0)$, for any Bravais lattice, lie on the same one-dimensional curve.

1.3 Effective Properties of the Periodic Auxetic Lattice

In this section we derive the effective constitutive parameters of the lattices. A perfect lattice would clearly have zero in-plane bulk modulus and unbounded shear moduli. In order to estimate the macroscopic behaviour for a real lattice, we consider the elastic behaviour of the elements of the lattice and we compute the effective constitutive behaviour as a function of the constitutive behaviour of the single constituents and of the micro-structure. To ensure stability we introduce extensional or rotational elastic springs that can also mimic the effect of friction in a loading branch or model elastic hinges (see Fig. 1.16 for the hexagonal lattice).

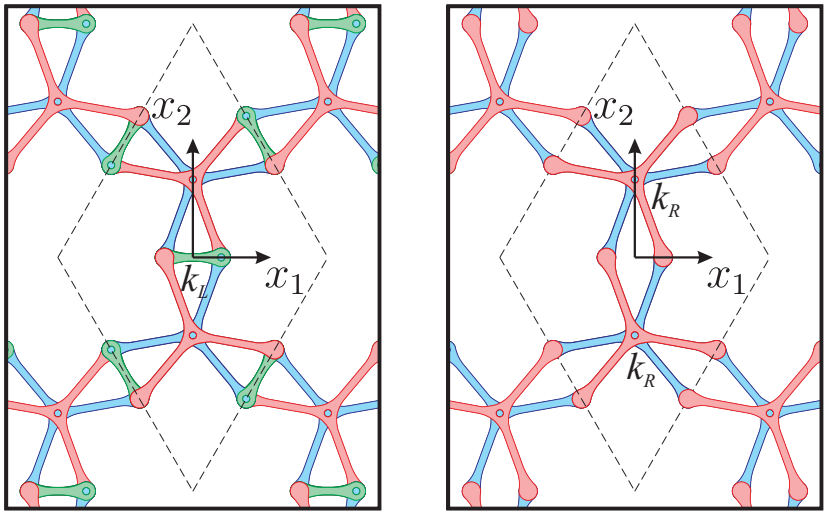

(a) (b)

FIGURE 1.16: Hexagonal lattice reinforced with elastic springs. (a) Longitudinal springs of stiffness k_L. (b) Rotational spring of stiffness k_R. The dashed area represent a typical unit cell of the periodic elastic system.

For simplicity we restrict the attention to macroscopic linear elasticity. The linearised behaviour depends nonlinearly on the reference configuration determined by γ_0, that will be indicated as γ in the following for ease of notation. The hexagonal and triangular lattices have three-fold symmetries and basic considerations on the symmetry group of the material lead to the conclusion that the constitutive behaviour is isotropic (in the plane of deformation). Similar considerations, based on the tetragonal symmetry of the square lattice, lead to the conclusion that the square lattice is cubic. Therefore, it will be necessary to compute two effective elastic constants for the isotropic structures and three for the cubic one. Stability constrains the in-plane Poisson's ratio to range between -1 and $+1$. Effective

properties are denoted as K^* (bulk modulus), E^* (Young's modulus), μ^* (shear modulus) and ν^* (Poisson's ratio) and macroscopic stress and strain as $\overline{\sigma}$ and $\overline{\varepsilon}$, respectively.

1.3.1 Analysis of the hexagonal lattice

The analytical derivation of the macroscopic properties for the periodic hexagonal lattice is given. The structure is composed of slender crosses and classical structural theories can be conveniently applied to analyse the response of the elastic system. In particular, each arm of a single cross-shaped element is modelled as an Euler beam undergoing flexural and extensional deformations. Each beam has Young's modulus E, cross-sectional area A and second moment of inertia J. Additional springs have longitudinal stiffness equal to k_L or rotational stiffness equal to k_R (see Fig. 1.16). We also introduce the non-dimensional stiffness ratio parameters $\alpha_1 = k_L p/(EA)$, $\alpha_2 = k_L p^3/(EJ)$, $\alpha_3 = k_R/(pEA)$ and $\alpha_4 = k_R p/(EJ)$. The lattice structure is invariant to 60^o, we remark that structural invariance to 60^o rotations (hexagonal symmetry) gives rise to a mechanical condition of transverse isotropy, that is, isotropy in plane. To feature the structural behaviour of the lattices we need to determine two elastic moduli. The compliance matrix $\mathbf{S}$ is shown in 1.27:

$$\mathbf{S} = \begin{bmatrix} s_{11} & s_{12} & 0 \\ s_{12} & s_{11} & 0 \\ 0 & 0 & s_{11} - s_{12} \end{bmatrix} = \begin{bmatrix} \frac{1}{E^*} & \frac{-\nu^*}{E^*} & 0 \\ \frac{-\nu^*}{E^*} & \frac{1}{E^*} & 0 \\ 0 & 0 & \frac{1+\nu^*}{E^*} \end{bmatrix} \tag{1.27}$$

Since the elastic behavior is isotropic, we have $E_1^* = E_2^* = E^*$, $\nu_{12}^* = \nu_{21}^* = \nu^*$. Macroscopic stresses are computed averaging the resultant forces on the boundary of the unit cell. Periodic boundary conditions have been applied on the boundary of the unit cell so that displacements are periodic and forces are anti-periodic. Additional constraints are introduced to prevent rigid body motions. To solve the structure we apply the Principle of Virtual Work (PVW) (see, for example [78], Chap. 15, §326). In the following, we apply the PVW in two steps: in the first we find the internal actions (bending moments M, shear forces V, axial forces N and spring forces S^L and moments M^R) of the structure searching for the kinematic admissible configuration in the set of statically admissible ones (*Flexibility Method*) and in the second step we compute the macroscopic displacements. This procedure

has the advantage of maintaining a sufficiently simple analytical treatment. We point out that all the results have been also verified numerically implementing a finite element code in Comsol Multiphysics®.

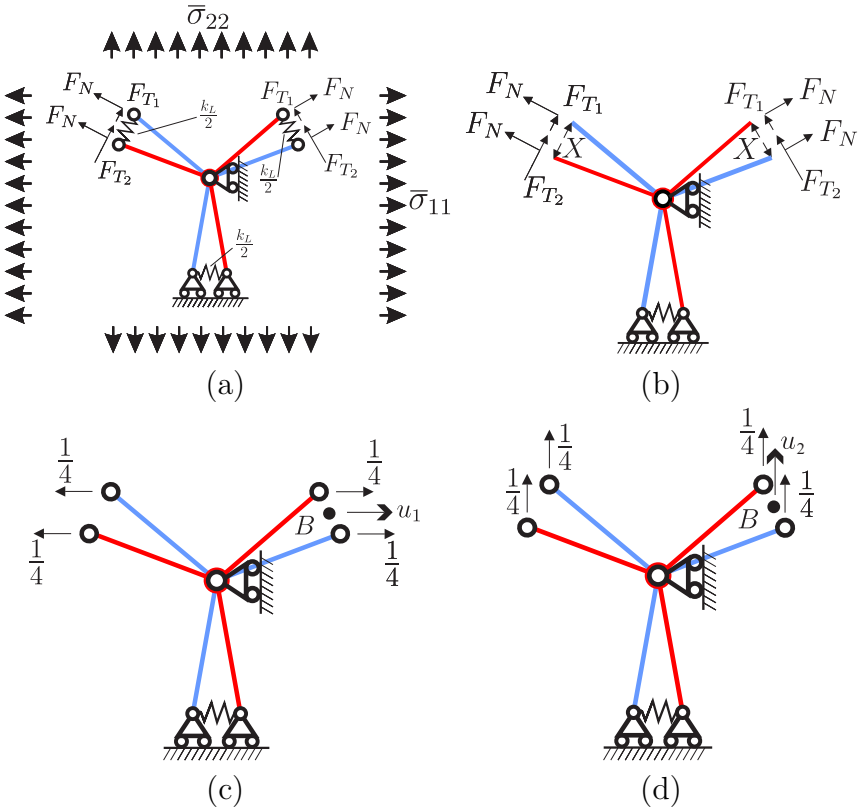

FIGURE 1.17: Application of the Principle of Virtual Work. Hexagonal lattice reinforced with longitudinal springs. (a) Simplified structure analysed for the computation of the effective properties. The applied forces F_N and F_{T_1} and F_{T_2}, with $F_T = (F_{T_1} + F_{T_2})/2$ correspond to macroscopic stresses components as in (1.34). (b) Disconnected statically determined structure introduced for the determination of the internal actions (M, N, S^L). (c) Statically determined structure adopted for the computation of the horizontal displacement u_1 of the point B. (d) Statically determined structure adopted for the computation of the horizontal displacement u_2 of the point B.

We consider the elastic structure as in Fig. 1.17(a), subjected to known normal and tangential external forces, corresponding to a macroscopic stress having components $\overline{\sigma}_{11}$ and $\overline{\sigma}_{22}$ different from zero. We define an equivalent statically determined (or isostatic) system disconnecting two springs and introducing the dual static parameter as unknown X, equal for the two springs, as shown in Fig. 1.17(b). Then, the general field of tension Ξ ($\Xi = M, V, N, S^L, M^R$) in equilibrium with the external loads is:

$$\Xi = \Xi_0 + X\Xi_1 \tag{1.28}$$

where Ξ_0 is the solution of the static scheme in equilibrium with the external loads and $X = 0$; while the field Ξ_1 is the solution of the static scheme in equilibrium with zero external loads (autosolution of the problem) and $X = 1$. The kinematic constraints, suppressed in the isostatic structure, are restored imposing the kinematic compatibility equation. The equation describes the virtual work done by the statically admissible actions Ξ due to the kinematically admissible displacements and deformations associated to Ξ_1 that determines the values of the unknown X and uniquely defines the elastic solution of the problem, i.e.,

$$X = -\frac{\sum_{beam}\int_0^p \left(M_0\frac{M_1}{EJ} + N_0\frac{N_1}{EA}\right)d\xi + \sum_{spring} S_0^L\frac{S_1^L}{k_L/2}}{\sum_{beam}\int_0^p \left(M_1\frac{M_1}{EJ} + N_1\frac{N_1}{EA}\right)d\xi + \sum_{spring} S_1^L\frac{S_1^L}{k_L/2}} = \\ = \left(F_N - \frac{\sqrt{3}(1+\alpha_1)}{3+3\alpha_1\cos^2\gamma+\alpha_2\sin^2\gamma}F_T\right)\cot\gamma, \tag{1.29}$$

where $F_T = (F_{T_1} + F_{T_2})/2$. We note that for sufficiently slender beam structures, the contribution due to the shear deformation is negligible compared to that due to flexural and axial deformations and, therefore, it has been neglected. We reconstruct the distribution of internal actions by a linear combination of partial diagrams of N and M and of the spring forces S^L, as functions of external forces F_N and $F_T = (F_{T1} + F_{T_2})/2$:

$$\begin{cases} N = N_0 + XN_1, \\ M = M_0 + XM_1, \\ S^L = S_0^L + XS_1^L. \end{cases} \tag{1.30}$$

Applying the PVW for the second time, we calculate the displacement of point B at the centre of the spring as shown in Fig. 1.17(c). To this purpose we consider the real structure as kinematically admissible, and an isostatic structure subjected to horizontal and vertical forces of magnitude equal $1/4$ as statically admissible, so that the virtual external works coincide exactly with the horizontal and vertical displacements of the point B, u_1 and u_2, respectively. In particular the PVW equations have the form

$$u_i = \sum_{beam}\int_0^p \left(M_i^*\frac{M}{EJ} + N_i^*\frac{N}{EA}\right)d\xi + \sum_{spring} S_i^{L*}\frac{S^L}{k_L/2}, \quad (i = 1, 2), \tag{1.31}$$

where (M_i^*, N_i^*, S_i^{L*}) $(i = 1, 2)$ are the internal actions of the statically admissible

structure subjected to forces applied in direction x_i $(i = 1, 2)$. The corresponding displacements are

$$\begin{aligned} u_1 &= A_1\, F_N + B_1\, F_T, \\ u_2 &= A_2\, F_N + B_2\, F_T, \end{aligned} \tag{1.32}$$

where

$$\begin{aligned} A_1 &= \frac{\sqrt{3}(\alpha_1 + \cos^2\gamma)}{2\sin^2\gamma\, k_L}, \\ B_1 &= \frac{9\cos^2\gamma(\cos^2\gamma\sin^2\gamma - 1)\alpha_1^2 - 9\cos^2\gamma(\cos^2\gamma + 1)\alpha_1}{6\sin^2\gamma(3 + 3\alpha_1\cos^2\gamma + \alpha_2\sin^2\gamma)k_L} \\ &\quad + \frac{6\cos^2\gamma\sin^4\gamma\,\alpha_1\alpha_2 + \sin^6\gamma\,\alpha_2^2 + 3\sin^4\gamma\,\alpha_2 - 9\cos^4\gamma}{6\sin^2\gamma(3 + 3\alpha_1\cos^2\gamma + \alpha_2\sin^2\gamma)k_L}, \end{aligned}$$

$$\begin{aligned} A_2 &= 3\frac{3\sqrt{3}\cos^2\gamma\,\alpha_1^2 + \sin^2\gamma\,\alpha_1\alpha_2 + 3(1 + \cos^4\gamma)\alpha_1}{2\sin^2\gamma(3 + 3\alpha_1\cos^2\gamma + \alpha_2\sin^2\gamma)k_L} \\ &\quad + 3\frac{\cos^2\gamma\sin^2\gamma\,\alpha_2 + 3\cos^2\gamma}{2\sin^2\gamma(3 + 3\alpha_1\cos^2\gamma + \alpha_2\sin^2\gamma)k_L}, \\ B_2 &= -\sqrt{3}\frac{9\cos^2\gamma(\cos^2\gamma\sin^2\gamma + 1)\alpha_1^2 + 6\sin^2\gamma(\cos^2\gamma\sin^2\gamma + 1)\alpha_1\alpha_2}{6\sin^2\gamma(3 + 3\alpha_1\cos^2\gamma + \alpha_2\sin^2\gamma)k_L} \\ &\quad - \frac{9(2 - \cos^2\gamma\sin^2\gamma)\alpha_1 + \sin^6\gamma\,\alpha_2^2 + 3(1 - \cos^4\gamma)\alpha_2 + 9\cos^2\gamma}{6\sin^2\gamma(3 + 3\alpha_1\cos^2\gamma + \alpha_2\sin^2\gamma)k_L}. \end{aligned} \tag{1.33}$$

Details of the computations are reported in Appendix A. Eqns. (1.32) are explicit linear relations between the forces F_N and F_T associated with macroscopic stresses

$$\overline{\sigma}_{11} = \frac{\sqrt{3}F_N + F_T}{3p\sin\gamma}, \quad \overline{\sigma}_{22} = \frac{\sqrt{3}F_N - 3F_T}{3p\sin\gamma} \tag{1.34}$$

and displacement of the point B associated with macroscopic strains

$$\overline{\varepsilon}_{11} = \frac{2u_1}{\sqrt{3}p\sin\gamma} = 2\frac{A_1F_N + B_1F_T}{\sqrt{3}p\sin\gamma}, \quad \overline{\varepsilon}_{22} = \frac{2u_2}{3p\sin\gamma} = 2\frac{A_2F_N + B_2F_T}{3p\sin\gamma}. \tag{1.35}$$

Solving eqns. (1.35) in terms of F_N and F_T and substituting the result into eqn. (1.34) leads to the macroscopic constitutive relation between the macroscopic stress $\overline{\sigma}$ and macroscopic strain $\overline{\varepsilon}$. Clearly, appropriate choices of the forces F_N and F_T can be considered in order to set to zero some components of the stress.

1.3.1.1 Hexagonal lattice with longitudinal springs

The Poisson's ratio ν^* of the hexagonal lattice is:

$$\nu^*_{H_L} = \frac{\overline{\sigma}_{22}\overline{\varepsilon}_{11} - \overline{\sigma}_{11}\overline{\varepsilon}_{22}}{\overline{\sigma}_{11}\overline{\varepsilon}_{11} - \overline{\sigma}_{22}\overline{\varepsilon}_{22}} = \frac{c_1\alpha_1^2 + c_2\alpha_2^2 + c_3\alpha_1\alpha_2 + c_4\alpha_1 + c_5\alpha_2 + c_6}{c_7\alpha_1^2 + c_2\alpha_2^2 + c_8\alpha_1\alpha_2 + c_9\alpha_1 + c_{10}\alpha_2 - c_6} \tag{1.36}$$

where

$$\begin{aligned}
&c_1 = 9\cos^2\gamma(\cos^4\gamma - \cos^2\gamma + 2), && c_2 = -\sin^6\gamma,\\
&c_3 = 3\sin^2\gamma(2\cos^4\gamma - 2\cos^2\gamma + 1), && c_4 = 9(2\cos^4\gamma + \cos^2\gamma + 1)\\
&c_5 = -3(2\cos^4\gamma - 3\cos^2\gamma + 1), && c_6 = 18\cos^2\gamma,\\
&c_7 = 9\cos^2\gamma(\cos^4\gamma - \cos^2\gamma - 2), && c_8 = 3\sin^2\gamma(2\cos^4\gamma - 2\cos^2\gamma - 3),\\
&c_9 = -9(2\cos^4\gamma - \cos^2\gamma + 3), && c_{10} = -3\sin^2\gamma(2\cos^2\gamma + 1).
\end{aligned} \tag{1.37}$$

The effective in-plane bulk modulus is

$$K^*_{H_L} = \frac{1}{2}\frac{\overline{\sigma}_{11} + \overline{\sigma}_{22}}{\overline{\varepsilon}_{11} + \overline{\varepsilon}_{22}} = \frac{\sqrt{3}\sin^2\gamma\, k_L}{6(\cos^2\gamma + \alpha_1)}. \tag{1.38}$$

Consequently, the Young's modulus of the hexagonal lattice with extensional springs is

$$\begin{aligned}
E^*_{H_L} &= \frac{\overline{\sigma}_{11}^2 - \overline{\sigma}_{22}^2}{\overline{\sigma}_{11}\overline{\varepsilon}_{11} - \overline{\sigma}_{22}\overline{\varepsilon}_{22}} = 2K^*_{H_L}(1 - \nu^*_{H_L})\\
&= \frac{4\sqrt{3}k_L\sin^2\gamma(3 + 3\cos^2\gamma\,\alpha_1 + \sin^2\gamma\,\alpha_2)}{-c_7\alpha_1^2 - c_2\alpha_2^2 - c_8\alpha_1\alpha_2 - c_9\alpha_1 + c_{10}\alpha_2 + c_6},
\end{aligned} \tag{1.39}$$

where the constants c_2, c_{6-10} are given in eqn. (1.37) and the shear modulus is given by

$$\begin{aligned}
\mu^*_{H_L} &= \frac{1}{2}\frac{\overline{\sigma}_{11} - \overline{\sigma}_{22}}{\overline{\varepsilon}_{11} - \overline{\varepsilon}_{22}} = \frac{1 - \nu^*_{H_L}}{1 + \nu^*_{H_L}}K^*_{H_L}\\
&= \frac{(3 + 3\cos^2\gamma\,\alpha_1 + \sin^2\gamma\,\alpha_2)\sqrt{3}\,k_L}{9\cos^4\gamma\,\alpha_1^2 + \sin^4\gamma\,\alpha_2^2 + 3(1 + 2\sin^2\gamma\,\cos^2\gamma)\alpha_1\alpha_2 + 9\,\alpha_1 + 3\,\alpha_2}.
\end{aligned} \tag{1.40}$$

1.3.1.2 Hexagonal lattice with rotational springs

In presence of rotational rather than longitudinal springs, the structure is statically determined and the effective constitutive parameters are the following

$$
\begin{aligned}
\nu^*_{H_R} &= \frac{3(1-2\cos^2\gamma)\alpha_3 - (1-2\cos^2\gamma)\alpha_4 + 18\cos^2\gamma}{3(-3+2\cos^2\gamma)\alpha_3 - (1+2\cos^2\gamma)\alpha_4 - 18\cos^2\gamma}, \\
K^*_{H_R} &= \frac{\sqrt{3}\,(k_R/p^2)}{2(3\sin^2\gamma\,\alpha_3 + \cos^2\gamma\,\alpha_4 + 9\cos^2\gamma)}, \\
E^*_{H_R} &= \frac{8\sqrt{3}\,(k_R/p^2)}{3(3-2\cos^2\gamma)\alpha_3 + (1+2\cos^2\gamma)\,\alpha_4 + 18\cos^2\gamma}, \\
\mu^*_{H_R} &= \frac{2\sqrt{3}\,(k_R/p^2)}{\alpha_4 + 3\,\alpha_3},
\end{aligned}
\tag{1.41}
$$

where we remember that $\alpha_3 = k_R/(EA\,p)$ and $\alpha_4 = (k_R\,p)/(EJ)$.

1.3.2 Analysis of the triangular lattice

The isotropic triangular lattice structures with longitudinal and rotational springs are given in Figs. 1.18(a)-(b). In this case the compliance matrix **S** is equal to that shown in 1.27. We consider the elastic structure as in Fig. 1.19(a), subject to normal and tangential external forces supposed to be known and corresponding to a macroscopic stress $\bar{\sigma}_{11}$ and $\bar{\sigma}_{22}$. We define an equivalent statically determined system disconnecting two springs and introducing the dual static parameter as unknown X, equal for the two springs, as shown in Fig. 1.19(b).

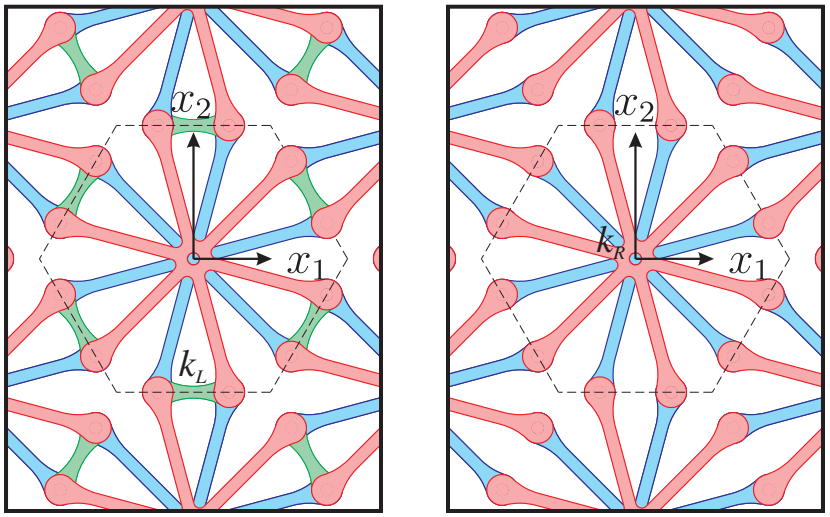

(a) (b)

FIGURE 1.18: Triangular lattice reinforced with elastic springs. (a) Longitudinal springs of stiffness k_L. (b) Rotational spring of stiffness k_R. The dashed area represent a typical unit cell of the periodic elastic system.

The deformed configurations of the isostatic equivalent structure violate the internal constraint in the two springs suppressed in the structure made isostatic.

Such kinematic constraints must be restored imposing the kinematic compatibility equation that determines the values of the unknown X and uniquely defines the elastic solution of the problem, as follows:

$$X = -\frac{\sum_{beam}\int_0^p \left(M_0\frac{M_1}{EJ} + N_0\frac{N_1}{EA}\right)d\xi + \sum_{spring} S_0^L \frac{S_1^L}{k_L/2}}{\sum_{beam}\int_0^p \left(M_1\frac{M_1}{EJ} + N_1\frac{N_1}{EA}\right)d\xi + \sum_{spring} S_1^L \frac{S_1^L}{k_L/2}} = \\ = \frac{F_N[(3\cos^2\gamma - 1)\alpha_1 + \sin^2\gamma\alpha_2 + 2] + F_V(1+\alpha_1)}{\sin^2\gamma\alpha_2 + 3\cos^2\gamma\alpha_1 + 3}\cot\gamma, \qquad (1.42)$$

where $F_T = (F_{T_1} + F_{T_2})/2$.

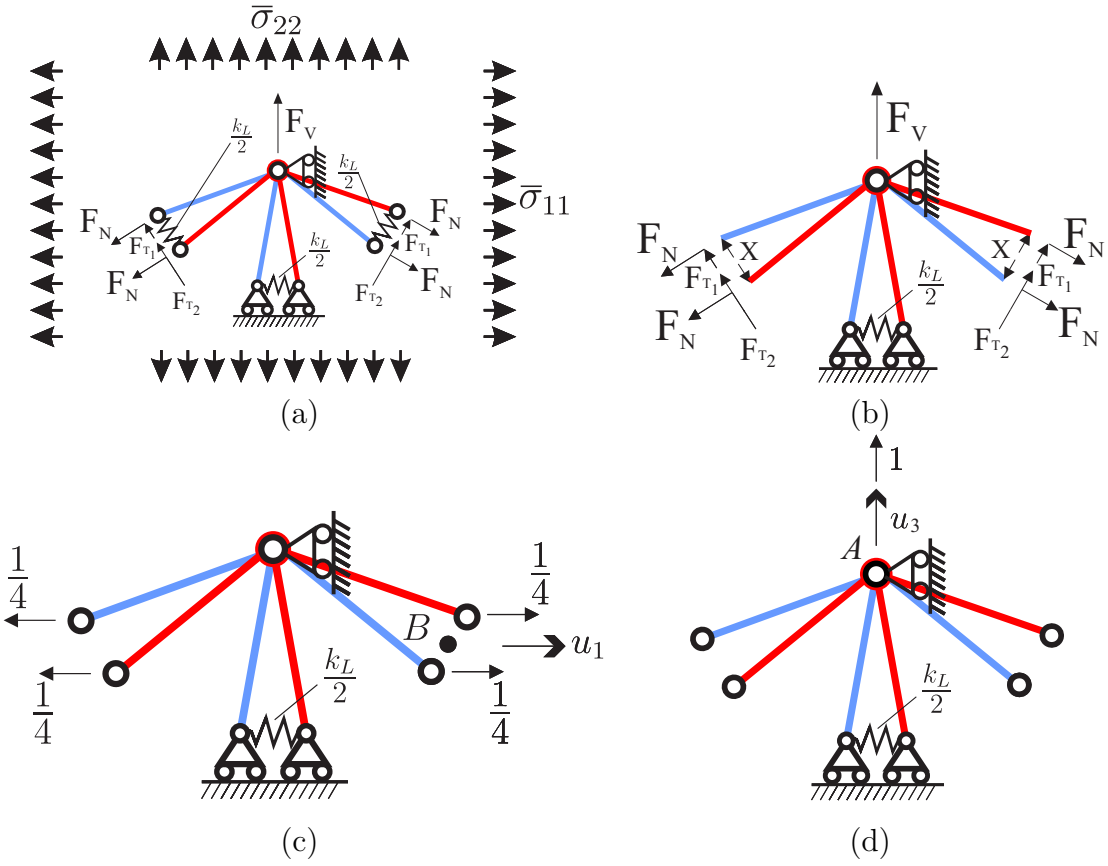

FIGURE 1.19: Application of the Principle of Virtual Work. Lattice reinforced with longitudinal springs. (a) Simplified structure analyzed for the computation of the effective properties. The applied forces F_N, F_V, F_{T1} and F_{T2} correspond to macroscopic stresses components $\bar{\sigma}_1 1$ and $\bar{\sigma}_2 2$. (b) Disconnected statically determined structure introduced for the determination of the internal actions (M,N,S^L). (c-d) Statically determined structure adopted for the computation of the displacement of the points A and B

We reconstruct the distribution of internal actions by a linear combination of partial diagrams of N and M and of the spring forces S^L, as functions of external forces F_N, $F_T = (F_{T1} + F_{T2})/2$ and F_V. Applying a second time the PVW we

compute the displacement of the point A and B (center of the spring) as shown in Figs.1.19(c)-(d). To do this we consider as kinematically admissible structure the real structure and as statically admissible structure, an isostatic structure subjected to horizontal and vertical forces of magnitude equal 1/4, respectively, so that the virtual external works coincide exactly with the horizontal and vertical displacement of the point B (u_1 and u_2 in Fig. 1.19(c)), and we calculate the displacement of the point A (u_3 in Fig. 1.19(d)) considering a vertical force of unitary magnitude, so that the virtual external works coincide exactly with the vertical displacement of the point A. In particular the PVW equations have the form:

$$u_i = \sum_{beam} \int_0^p \left(M_i^* \frac{M}{EJ} + N_i^* \frac{N}{EA} \right) d\xi + \sum_{spring} S_i^{L*} \frac{S^L}{k_L/2}, \quad (i = 1, 2 \quad and \quad 3), \tag{1.43}$$

where M_i^*, N_i^* and S_i^{L*} (with i=1, 2 and 3) are the internal actions of the statically admissible structures subjected to forces applied in the point B in horizontal and vertical direction, and the internal actions of the statically admissible structure subjected to a vertical forces applied in the point A in vertical direction. The corresponding displacement are:

$$\begin{aligned} u_1 &= A_1\, F_N + B_1\, F_T + C_1\, F_V, \\ u_2 &= A_2\, F_N + B_2\, F_T + C_2\, F_V, \\ u_3 &= A_2\, F_N + B_2\, F_T + C_3\, F_V, \end{aligned}$$

where A_{1-3}, B_{1-3}, C_{1-3} are coefficients arising from the integrations. Details of the computations are reported in Appendix A. Eqns. (1.44) are explicit linear relations between the forces F_N, F_T and F_V associated to macroscopic stresses

$$\overline{\sigma}_{11} = \frac{\sqrt{3}F_N - F_T}{p \sin\gamma}, \quad \overline{\sigma}_{22} = \frac{4F_V + 2\sqrt{3}F_T + 2F_N}{2\sqrt{3}p \sin\gamma} \tag{1.44}$$

and displacement of the point B associated with macroscopic strains

$$\begin{aligned} \overline{\varepsilon}_{11} &= \frac{2u_1}{\sqrt{3}p \sin\gamma} = 2\frac{A_1F_N + B_1F_T + C_1F_V}{\sqrt{3}p \sin\gamma}, \\ \overline{\varepsilon}_{22} &= \frac{u_3}{p \sin\gamma} = 2\frac{A_3F_N + B_3F_T + C_3F_V}{p \sin\gamma}. \end{aligned} \tag{1.45}$$

Solving eqns. (1.45) in term of F_N, F_T and F_V and substituting the result into eqns. (1.44) leads to the macroscopic constitutive relation between the macroscopic stress and macroscopic strains. Clearly, appropriate choices of the forces F_N, F_T and F_V can be considered in order to set to zero some components of the stress. The effective properties are given below.

1.3.2.1 Triangular lattice with longitudinal springs

- Poisson's ratio

$$\nu^*_{T_L} = \frac{d_1\alpha_1^3 - 3\alpha_1^2\alpha_2 + d_2\alpha_1\alpha_2^2 + d_3\alpha_1^2 + d_4\alpha_2^2 + d_5\alpha_1\alpha_2 + d_6\alpha_1 + d_7\alpha_2}{-d_1\alpha_1^3 + d_8\alpha_1^2\alpha_2 + 3d_2\alpha_1\alpha_2^2 + d_9\alpha_1^2 + 3d_4\alpha_2^2 + d_{10}\alpha_1\alpha_2 - d_6\alpha_1 - d_7\alpha_2} \tag{1.46}$$

where

$$\begin{aligned}
&d_1 = -9\cos^4\gamma, && d_2 = \sin^4\gamma,\\
&d_3 = 9(\cos^6\gamma - 4\cos^4\gamma + 2\cos^2\gamma - 1), && d_4 = \sin^4\gamma\cos^2\gamma,\\
&d_5 = 3(6\cos^4\gamma - 7\cos^2\gamma - 2\cos^6\gamma + 1), && d_6 = -9\cos^2\gamma,\\
&d_7 = -3\cos^2\gamma, && d_8 = 3(4\sin^2\gamma\cos^2\gamma + 1),\\
&d_9 = 9(3\cos^6\gamma - 4\cos^4\gamma + 2\cos^2\gamma + 1) && d_{10} = 3(10\cos^4\gamma - 6\cos^6\gamma - 5\cos^2\gamma + 3).
\end{aligned} \tag{1.47}$$

- Bulk modulus

$$K^*_{T_L} = \frac{\sqrt{3}\sin^2\gamma\, k_L}{2\,(\cos^2\gamma + \alpha_1)}. \tag{1.48}$$

- Young's modulus

$$E^*_{T_L} = \frac{2\sqrt{3}\left[9\cos^4\gamma\,\alpha_1^2 + \sin^4\gamma\,\alpha_2^2 + 3(2\cos^2\gamma\sin^2\gamma + 1)\alpha_1\alpha_2 + 9\alpha_1 + 3\alpha_2\right]\sin^2\gamma\, k_L}{-d_1\alpha_1^3 + d_8\alpha_1^2\alpha_2 + 3d_2\alpha_1\alpha_2^2 + d_9\alpha_1^2 + 3d_4\alpha_2^2 + d_{10}\alpha_1\alpha_2 - d_6\alpha_1 - d_7\alpha_2}, \tag{1.49}$$

where d_1, d_2, d_4, d_{6-10} are given in 1.47.

- Shear modulus

$$\mu^*_{T_L} = \frac{\sqrt{3}\left[9\cos^4\gamma\alpha_1^2 + \sin^4\gamma\alpha_2^2 + 3(2\cos^2\gamma\sin^2\gamma + 1)\alpha_1\alpha_2 + 9\alpha_1 + 3\alpha_2\right]k_L}{12\cos^2\gamma\,\alpha_1^2\alpha_2 + 4\sin^2\gamma\,\alpha_1\alpha_2^2 + 9\sin^2 2\gamma\,\alpha_1^2 + 6(2 - \sin^2 2\gamma)\alpha_1\alpha_2 + \sin^2 2\gamma\,\alpha_2^2}. \tag{1.50}$$

1.3.2.2 Triangular lattice with rotational springs

When rotational springs are considered, the triangular lattice structure is statically determined and the effective constants are as follows.

- Poisson's ratio

$$\nu^*_{T_R} = \frac{e_1\alpha_3^2 + e_2\alpha_4^2 + e_3\alpha_3\alpha_4 + e_4\alpha_3 + e_5\alpha_4}{e_6\alpha_3^2 + e_7\alpha_4^2 + e_8\alpha_3\alpha_4 - e_4\alpha_3 - e_5\alpha_4}, \tag{1.51}$$

where

$$\begin{aligned} e_1 &= 9\,(2\cos^4\gamma - 3\cos^2\gamma + 1), & e_2 &= (2\cos^4\gamma - \cos^2\gamma), \\ e_3 &= 3(4\cos^2\gamma\sin^2\gamma - 1), & e_4 &= 27\cos^2\gamma, \\ e_5 &= 9\cos^2\gamma, & e_6 &= 9\,(2\cos^4\gamma - \cos^2\gamma - 1), \\ e_7 &= 2\cos^4\gamma - 3\cos^2\gamma, & e_8 &= 12\cos^2\gamma\sin^2\gamma - 9. \end{aligned} \tag{1.52}$$

- Bulk modulus

$$K^*_{T_R} = \frac{3\sqrt{3}\,(k_R/p^2)}{2(3\,\sin^2\gamma\,\alpha_3 + \cos^2\gamma\,\alpha_4 + 9\cos^2\gamma)}. \tag{1.53}$$

- Young's modulus

$$E^*_{T_R} = -\frac{6\sqrt{3}\,(3\alpha_3 + \alpha_4)\,(k_R/p^2)}{e_6\alpha_3^2 + e_7\alpha_4^2 + e_8\alpha_3\alpha_4 - e_4\alpha_3 - e_5\alpha_4}, \tag{1.54}$$

where the coefficients e_{4-8} are given in eq.(1.52).

- Shear modulus

$$\mu^*_{T_R} = \frac{3\sqrt{3}\,(3\,\alpha_3 + \alpha_4)\,(k_R/p^2)}{9\sin^2 2\gamma\,\alpha_3^2 + \sin^2 2\gamma\,\alpha_4^2 + 6(2 - \sin^2 2\gamma)\alpha_3\alpha_4}. \tag{1.55}$$

1.3.3 Analysis of the square lattice

The square lattice has cubic symmetry and it is necessary to compute three independent elastic constants to determine the effective behaviour of the structure. In this case the compliance matrix $\mathbf{S}$ is:

$$\mathbf{S} = \begin{bmatrix} s_{11} & s_{12} & 0 \\ s_{12} & s_{11} & 0 \\ 0 & 0 & s_{13} \end{bmatrix} = \begin{bmatrix} \frac{1}{E^*} & \frac{-\nu^*}{E^*} & 0 \\ \frac{-\nu^*}{E^*} & \frac{1}{E^*} & 0 \\ 0 & 0 & \frac{1}{2\mu^*} \end{bmatrix} \tag{1.56}$$

The lattice with longitudinal and rotational springs is given in Fig. 1.20, the simplified structure used to compute the in-plane Poisson's ratio $\nu^*_{S_L}$, bulk modulus

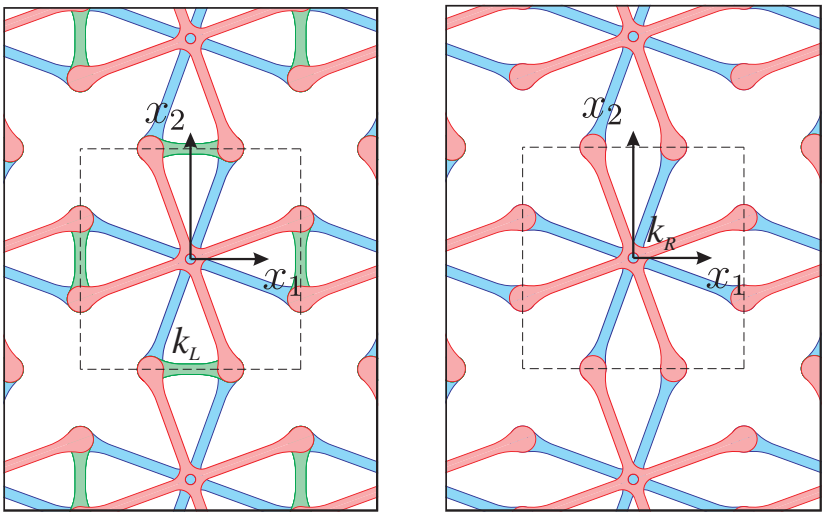

(a) (b)

FIGURE 1.20: Square lattice reinforced with elastic springs. (a) Longitudinal springs of stiffness k_L. (b) Rotational spring of stiffness k_R. The dashed area represent a typical unit cell of the periodic elastic system.

$K^*_{S_L}$ and Young's modulus $E^*_{S_L}$ is shown in Fig. 1.21(a). Statically the structure is twice overdetermined and it is therefore necessary to introduce two disconnections and two dual static variables to find the internal actions within the elastic system. The simplified structure introduced to compute the in-plane shear modulus $\mu^*_{S_L}$ is given in Fig. 1.21(b). In this case the springs are not activated and they can be neglected, so that the structure can be considered as statically determined. The same structural models of Fig. 1.21 have been considered with rotational springs instead of longitudinal for the second case. The effective properties are reported in the following.

1.3.3.1 Square lattice with longitudinal springs

- Poisson's ratio

$$\nu^*_{S_L} = \frac{-3\,(\alpha_1+1)^2\,\cos^2\gamma}{3\cos^2\gamma\,\alpha_1^2+2\sin^2\gamma\,\alpha_1\alpha_2+6(1-\sin^2\gamma\cos^2\gamma)\alpha_1+2\sin^2\gamma\cos^2\gamma\,\alpha_2+3\cos^2\gamma}. \quad (1.57)$$

- Bulk modulus

$$K^*_{S_L} = \frac{k_L\,\sin^2\gamma}{2\,(\alpha_1+\cos^2\gamma)}. \quad (1.58)$$

- Young's modulus

$$E^*_{S_L} = \frac{2\,k_L\sin^2\gamma(3\cos^2\gamma\,\alpha_1+\sin^2\gamma\,\alpha_2+3)}{3\cos^2\gamma\,\alpha_1^2+2\sin^2\gamma\,\alpha_1\alpha_2+6(1-\sin^2\gamma\cos^2\gamma)\alpha_1+2\sin^2\gamma\cos^2\gamma\,\alpha_2+3\cos^2\gamma}. \quad (1.59)$$

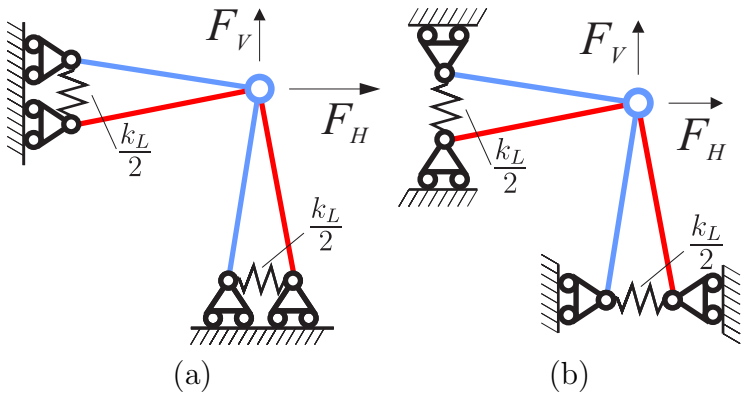

FIGURE 1.21: Simplified structure used for the computation of the effective in-plane Poisson's ratio $\nu^*_{S_L}$, bulk modulus $K^*_{S_L}$ and Young's modulus $E^*_{S_L}$. The forces $F_{H,V}$ are associated with macroscopic stress components $\overline{\sigma}_{11,22} = F_{H,V}/(2p\sin\gamma)$. (c) Simplified structure used for the computation of the in-plane shear modulus $\mu^*_{S_L}$. The force F_V is associated with the macroscopic stress $\overline{\sigma}_{12} = F_V/(2p\sin\gamma)$.

- Shear modulus

$$\mu^*_{S_L} = \frac{3k_L}{2(3\cos^2\gamma\,\alpha_1 + \sin^2\gamma\,\alpha_2)}. \tag{1.60}$$

1.3.3.2 Square lattice with rotational springs

The structure is statically undetermined with degree 1. The effective constitutive parameters are as follows.

- Poisson's ratio

$$\nu^*_{S_R} = -\frac{3\,\cos^2\gamma}{3\sin^2\gamma\,\alpha_3 + \cos^2\gamma\,\alpha_4 + 3\cos^2\gamma}. \tag{1.61}$$

- Bulk modulus

$$K^*_{S_R} = -\frac{3\,(k_R/p^2)}{2(3\sin^2\gamma\,\alpha_3 + \cos^2\gamma\,\alpha_4 + 6\cos^2\gamma)}. \tag{1.62}$$

- Young's modulus

$$E^*_{S_R} = \frac{3\,(k_R/p^2)}{3\sin^2\gamma\,\alpha_3 + \cos^2\gamma\,\alpha_4 + 3\cos^2\gamma}. \tag{1.63}$$

- Shear modulus

$$\mu^*_{S_R} = \frac{3(k_R/p^2)}{2(3\cos^2\gamma\,\alpha_3 + \sin^2\gamma\,\alpha_4)}. \tag{1.64}$$

1.4 Analysis of effective properties

Here, the effective properties of the micro-stuctured media are analysed in detail. We consider at first the case of vanishing stiffness of the springs $k_L, k_R \to 0$. For every lattice

$$\begin{aligned} \nu^* &\simeq -1 + \nu_1^*\, k_{L,R} + \mathcal{O}\left(k_{L,R}^2\right), \qquad & K^* &\simeq 0 + K_1^*\, k_{L,R} + \mathcal{O}\left(k_{L,R}^2\right), \\ E^* &\simeq 0 + E_1^*\, k_{L,R} + \mathcal{O}\left(k_{L,R}^2\right), \qquad & \mu^* &\simeq \mu_0^* + \mu_1^*\, k_{L,R} + \mathcal{O}\left(k_{L,R}^2\right). \end{aligned} \tag{1.65}$$

where $\nu_1^*, K_1^*, E_1^*, \mu_{0,1}^* > 0$ and their explicit expressions are given in Table 1.2.

Lattice	Longitudinal springs	Rotational springs
Hexagonal	$\nu_1^* = \frac{p}{3}(\eta_1+\eta_2)$ $K_1^* = \frac{\sqrt{3}}{6}\tan^2\gamma$ $E_1^* = \frac{2\sqrt{3}}{3}\tan^2\gamma$ $\mu_0^* = \frac{\sqrt{3}}{p\,(\eta_1+\eta_2)}$	$\nu_1^* = \frac{\eta_1+\eta_2}{9\,p\cos^2\gamma}$ $K_1^* = \frac{\sqrt{3}}{18\,p^2\cos^2\gamma}$ $E_1^* = \frac{2\sqrt{3}}{9\,p^2\cos^2\gamma}$ $\mu_0^* = \frac{\sqrt{3}}{p\,(\eta_1+\eta_2)}$
Triangular	$\nu_1^* = \frac{4p}{3}\frac{\eta_1\,\eta_2}{\eta_1+\eta_2}\tan^2\gamma$ $K_1^* = \frac{\sqrt{3}}{2}\tan^2\gamma$ $E_1^* = 2\sqrt{3}\tan^2\gamma$ $\mu_0^* = \frac{3\sqrt{3}}{4\,p}\frac{\eta_1+\eta_2}{\eta_1\,\eta_2}$	$\nu_1^* = \frac{4}{9}\frac{\eta_1\,\eta_2}{p\,\cos^2\gamma\,(\eta_1+\eta_2)}$ $K_1^* = \frac{\sqrt{3}}{6\,p^2\,\cos^2\gamma}$ $E_1^* = \frac{2\sqrt{3}}{3\,p^2\,\cos^2\gamma}$ $\mu_0^* = \frac{3\sqrt{3}}{4\,p}\frac{\eta_1+\eta_2}{\eta_1\,\eta_2}$
Square	$\nu_1^* = \frac{2}{3}p\,\eta_1\,\tan^2\gamma$ $K_1^* = \frac{1}{2}\tan^2\gamma$ $E_1^* = 2\,\tan^2\gamma$ $\mu_0^* = \frac{3}{2\,p\,\eta_2}$	$\nu_1^* = \frac{1}{3}\frac{\eta_1}{p\,\cos^2\gamma}$ $K_1^* = \frac{1}{4\,p^2\,cos^2\gamma}$ $E_1^* = \frac{1}{p^2\,cos^2\gamma}$ $\mu_0^* = \frac{3}{2\,p\,\eta_2}$

TABLE 1.2: Explicit expression of the coefficients in the asymptotic formulae in eqns. (1.65). In the table $\eta_1 = 3\,\sin^2\gamma/(EA) + p^2\,\cos^2\gamma/(EJ)$, $\eta_2 = 3\,\cos^2\gamma/(EA) + p^2\,\sin^2\gamma/(EJ)$.

It is shown in eqns. (1.65) that also for deformable structures the Poisson's ratio remains -1 when the spring stiffnesses are zero, while the effect of the springs is to increase the value of ν^*. In such a limit, the bulk and the Young's moduli vanish while the shear modulus remains finite. This is clearly associated with the deformation mechanism of the lattice, which involve deformation of the cross-shaped elements when a macroscopic shear stress or shear deformation is applied, while macroscopic volumetric deformations can be sustained by rigid internal rotations

of the elements of the micro-structure. The limiting behaviour described in eqns. (1.65) can also be understood in terms of relative stiffness between the spring elements and the elements of the lattice as described by the coefficients $\alpha_{1,\cdots,4}$. In this respect, when $\alpha_{1,\cdots,4} \to 0$, the same outcomes of eqns. (1.65) are obtained. The dependence of the Poisson's ratio on the stiffnesses k_L and (k_R/p^2) is shown in Fig. 1.22(a) and Fig. 1.22(b), respectively, for the three micro-structures. Results confirm that the Poisson's ratio approaches -1 when the spring constants are zero. They also show that $\nu^*_{S_{L,R}} < \nu^*_{T_{L,R}} < \nu^*_{H_{L,R}}$.

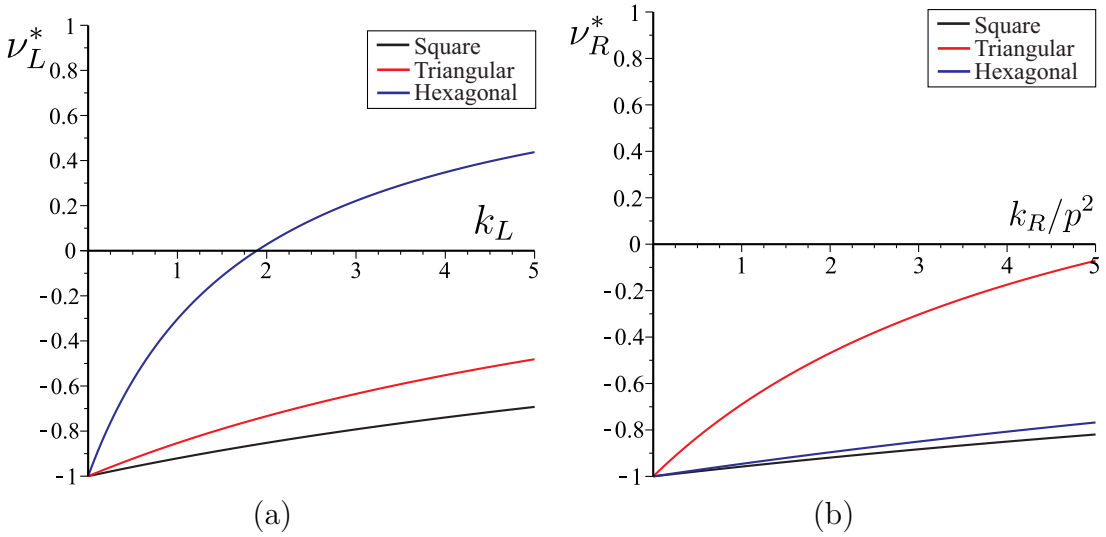

FIGURE 1.22: Effective Poisson's ratio ν^* as a function of the spring stiffness k_L [N/mm] and k_R [N mm]. (a) $\nu^*_{H_L}$, $\nu^*_{T_L}$, $\nu^*_{S_L}$ are given as a function of k_L. (b) $\nu^*_{H_R}$, $\nu^*_{T_R}$, $\nu^*_{S_R}$ are given as a function of k_R/p^2. Results correspond to the following parameters: Young's modulus $E = 3000$ MPa (thermoplastic polymer ABS), $A = 50$ mm^2, $J = 417$ mm^4 corresponding to the geometry given in Fig. 1.26.

It is worthwhile to note the maximum theoretical values that can be reached by the Poisson's ratios at the limit $k_L, k_R/p^2 \to \infty$; the limiting expressions are

$$\nu^*_{H_L} \simeq 1 - \frac{(s/p)^2}{\sin^2\gamma} + \mathcal{O}\left((s/p)^4\right),$$
$$\nu^*_{H_R} \simeq \frac{1-2\cos^2\gamma}{1+2\cos^2\gamma}\left[1 - \frac{(s/p)^2}{1+2\cos^2\gamma}\right] + \mathcal{O}\left((s/p)^4\right),$$
$$\nu^*_{T_L} \simeq \frac{1}{3} - \frac{1+\sin^2\gamma\cos^2\gamma}{\sin^2\gamma}(s/p)^2 + \mathcal{O}\left((s/p)^4\right),$$

$$\nu^*_{T_R} \simeq \frac{1-2\cos^2\gamma}{3-2\cos^2\gamma}\left[1-\frac{(s/p)^2}{3-2\cos^2\gamma}\right]+\mathcal{O}\left((s/p)^4\right),$$
$$\nu^*_{S_L} \simeq 0-\frac{\cot^2\gamma}{8}(s/p)^2+\mathcal{O}\left((s/p)^4\right),$$
$$\nu^*_{S_R} \to 0, \tag{1.66}$$

where in eqns. (1.66) and in the following we consider, for simplicity, rectangular cross-sections of the arms of the cross-shaped elements, so that $A = t\,s$ and $J = t\,s^3/12$, where s and t are the in-plane and out-of-plane thicknesses, respectively. Therefore $s/p \ll 1$. We note that the Poisson's ratio remains always negative for the square lattice approaching zero in the limit. Interestingly, the hexagonal lattice with longitudinal springs has a completely different behaviour approaching the upper limit for the Poisson's ratio corresponding to an incompressible material. For the structures with rotational springs the limit depends on the actual configuration described by the angle γ and ranges between -0.2 and 1 for the hexagonal lattice and between 0.2 and 1 for the triangular one. For general values of k_R and k_L, we note that the shear modulus μ^* is independent of the rotational stiffness k_R. Also, for the square lattice, the shear modulus does not depend on the longitudinal stiffness k_L; in fact, $\mu^*_{S_L} = \mu^*_{S_R}$. The polar diagrams of the Poisson's ratio and

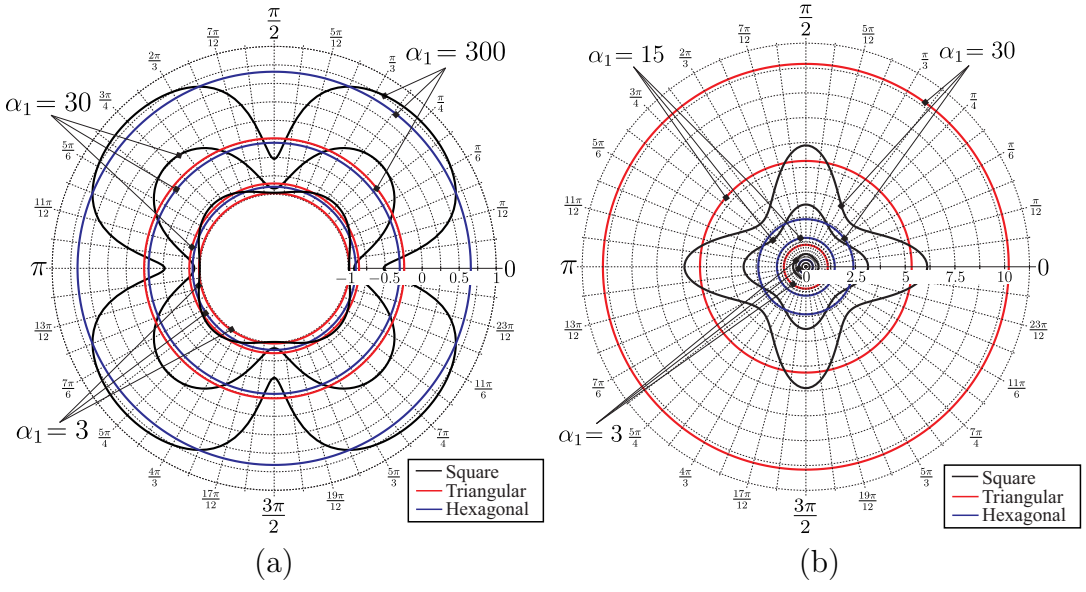

FIGURE 1.23: Polar diagrams of the (a) Poisson's ratio and (b) Young's modulus as a function of the angle β. Results are given for the three micro-geometries with longitudinal springs corresponding to different values of the non-dimensional stiffness ratio $\alpha_1 = (s/p)^2\alpha_2/12$.

Young's modulus are given in Fig. 1.23. In a reference system rotated of an angle β

with respect to the system of reference Ox_1x_2 the Poisson's ratio and the Young's modulus are given by

$$\nu^*(\beta) = -\frac{b_i b_j S^*_{ijkl} n_k n_l}{n_i n_j S_{ijkl} n_k n_l}, \quad E^*(\beta) = (n_i n_j S_{ijkl} n_k n_l)^{-1}, \quad (i,j,k,l = 1,2), \quad (1.67)$$

where $\mathbf{n} = (\cos\beta, \sin\beta)^T$, $\mathbf{b} = (-\sin\beta, \cos\beta)^T$ and $\mathbb{S}^*$ is the fully-symmetric compliance tensor having components

$$\begin{aligned} S^*_{1111} = S^*_{2222} = \frac{1}{E^*}, \qquad S^*_{1122} = S^*_{2211} = -\frac{\nu^*}{E^*}, \\ S^*_{1212} = S^*_{2121} = S^*_{1221} = S^*_{2112} = \frac{1}{4\mu^*}, \end{aligned} \quad (1.68)$$

and $\mu^* = E^*/(2(1+\nu^*))$ in the isotropic cases. In addition to the verified isotropy of the hexagonal and triangular lattices, the polar plots in Fig. 1.23 show the increase (decrease) of the Poisson's ratio (Young's modulus) in oblique direction with a maximum (minimum) for $\beta = \pi/4$, where

$$\begin{aligned} \nu^*_{S_L}(\pi/4) &= -\frac{3\cos^2\gamma + 3(1-\cos^2\gamma\,\sin^2\gamma)\alpha_1 - \sin^4\gamma\,\alpha_2}{3\cos^2\gamma + 3(1+\cos^2\gamma\,\sin^2\gamma)\alpha_1 + \sin^4\gamma\,\alpha_2}, \\ E^*_{S_L}(\pi/4) &= \frac{6\sin^2\gamma\,k_L}{3\cos^2\gamma + 3(1+\cos^2\gamma\,\sin^2\gamma)\alpha_1 + \sin^4\gamma\,\alpha_2}. \end{aligned} \quad (1.69)$$

We note that the square lattice recovers isotropy when $k_L \to 0$, in particular

$$\frac{\nu^*_{S_L}(\pi/4)}{\nu^*_{S_L}(0)} \simeq 1 + \mathcal{O}(k_L), \qquad \frac{E^*_{S_L}(\pi/4)}{E^*_{S_L}(0)} \simeq 1 + \mathcal{O}(k_L). \quad (1.70)$$

We focus now the attention on the effect of the axial and bending stiffness of the elements of the micro-structure on the effective properties; the stiffness ratios are estimated as

$$\alpha_1 \simeq \frac{k_L}{E}\frac{p}{s}, \quad \alpha_2 \simeq \frac{k_L}{E}\left(\frac{p}{s}\right)^3 \quad \text{and} \quad \alpha_3 \simeq \frac{k_R/p^2}{E}\frac{p}{s}, \quad \alpha_4 \simeq \frac{k_R/p^2}{E}\left(\frac{p}{s}\right)^3. \quad (1.71)$$

The ratio $p/s \gg 1$ is proportional to the slenderness of the arms of the cross-shaped elements of the micro-structures. It is also inversely proportional to the density of the effective medium, as also noted in [49]. On physical grounds, it is reasonable to consider $\alpha_1 < 10$ ($\alpha_3/p^2 < 10$) and, therefore $\alpha_1 \ll \alpha_2^{1/3}$ ($\alpha_2 \ll \alpha_4^{1/3}$). It follows that, for sufficiently low values of k_L and k_R, only $K^*_{H_L}$, $K^*_{T_L}$ and $K^*_{S_L}$ are governed by the axial stiffness of the arms of the cross-shaped elements of

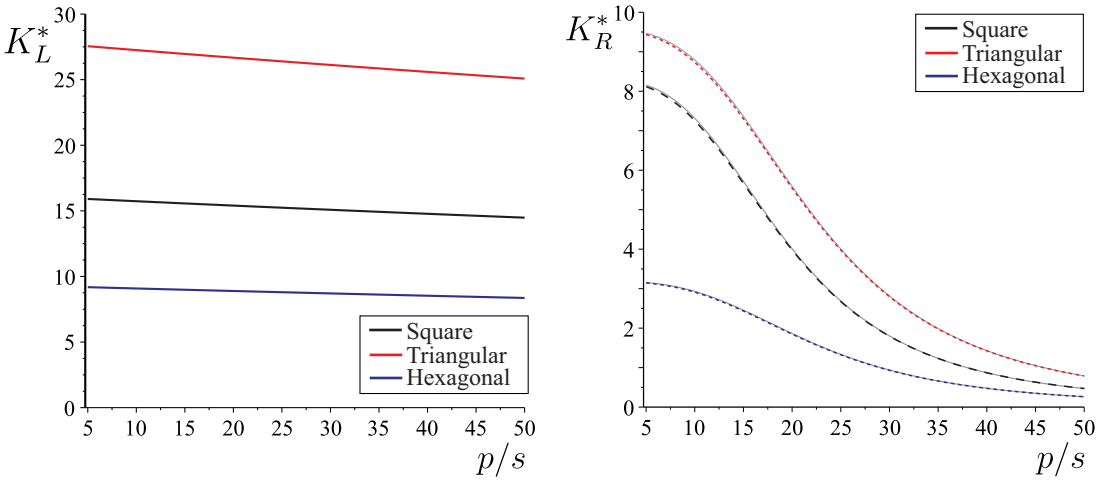

FIGURE 1.24: Effective bulk modulus K^* [MPa] as a function of the 'slenderness' p/s. (a) $K^*_{H_L}$, $K^*_{T_L}$ and $K^*_{S_L}$. (b) $K^*_{H_R}$, $K^*_{T_R}$ and $K^*_{S_R}$ where dashed lines correspond to formulae in eqns. (1.41), (1.53) and (1.62) while continuous grey lines correspond to the same formulae with $\alpha_3 = 0$. Results are given for: Young's modulus $E = 3000$ MPa, $t = 5$ mm, $k_L = k_R/p^2 = 1$ N/mm.

the micro-structure, while the other effective constitutive parameters are governed by the flexural behaviour of the elements of the micro-structures associated with the parameters α_2 and α_4. In Fig. 1.24 the effective bulk modulus K^* is shown as a function of the geometrical parameter p/s; lattices with longitudinal and rotational springs are shown in parts (a) and (b), respectively. The triangular lattice is the stiffest and its bulk modulus is exactly three times the bulk modulus for the hexagonal micro-structure, in fact it is easy to check that for the same γ and the same geometrical parameters of the elements, the effective stored-energy density of the triangular lattice is exactly three times the effective stored-energy density of the hexagonal one when dilatational deformations are applied. The nearly linear dependence of $K^*_{H_L}$, $K^*_{T_L}$ and $K^*_{S_L}$ on the 'slenderness' p/s highlights the dependence of the bulk moduli on the axial stiffness of the element of the micro-structure while for $K^*_{H_R}$, $K^*_{T_R}$ and $K^*_{S_R}$, it is the bending stiffness of the elements of micro-structure that governs the effective behaviour. This is evident from the comparison between the dashed black lines, corresponding to formulae in eqns. (1.41), (1.53) and (1.62), and the grey continuous lines where the effect of the axial stiffness of the element has been neglected ($\alpha_3 = 0$). We conclude our analysis with a comparison of the proposed models with classical cellular solids. Square, triangular and hexagonal lattices are common topologies encountered in physical models and engineering applications and their static behaviour is discussed in [37, 49, 79, 80], among others. For the purpose of comparison we consider the

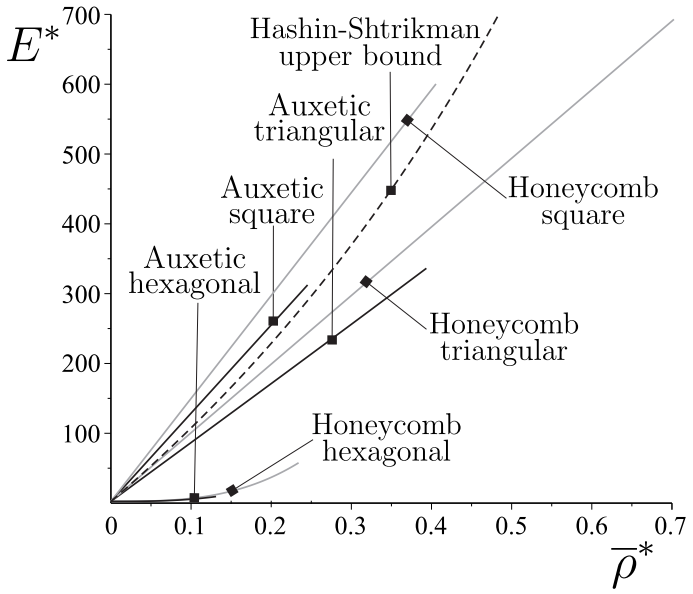

FIGURE 1.25: Comparison between auxetic and honeycomb solids. Effective Young's modulus E^* [MPa] is given as a function of the relative density $\overline{\rho}^*$. The results correspond to the parameters: Young's modulus $E = 3000$ MPa (thermoplastic polymer ABS), longitudinal springs stiffness $k_L = Es/(2p\cos\gamma)$ and $\gamma = 4\pi/9$. The Hashin-Shtrikman upper bound $E^* = E\,\overline{\rho}^*_H/(3 - 2\overline{\rho}^*_H)$ for isotropic media is also shown.

behaviour in terms of effective Young's Modulus E^* and we introduce the relative density parameter $\overline{\rho}^*$, defined as the ratio between the volume occupied by the thin elements of the micro-structure and the volumes of the unit cell. In particular, for the proposed hexagonal, square and triangular auxetic lattices, we have

$$\overline{\rho}^*_H = \frac{\sqrt{3}}{3\sin^2\gamma}\frac{s}{p}, \quad \overline{\rho}^*_S = \frac{1}{\sin^2\gamma}\frac{s}{p}, \quad \overline{\rho}^*_T = \frac{\sqrt{3}}{\sin^2\gamma}\frac{s}{p}, \tag{1.72}$$

respectively, where, for the purpose of comparison, the physical parameters are reported for unit out-of-plane thickness. The dominant deformation mechanism

Topology	**Density**	**Young's Modulus**	**Shear Modulus**	**Poisson's ratio**
Triangular	$\overline{\rho}^* = \frac{2\sqrt{3}\,s}{l}$	$\frac{2\sqrt{3}\,E\,s}{3\,l}$	$\frac{\sqrt{3}\,E\,s}{4\,l}$	$\frac{1}{3}$
Square	$\overline{\rho}^* = \frac{2\,s}{l}$	$\frac{E\,s}{l}$	$\frac{E\,s^3}{2\,l^3}$	$\frac{\nu\,s}{l}$
Hexagonal	$\overline{\rho}^* = \frac{2\,s}{\sqrt{3}\,l}$	$\frac{4\,E\,s^3}{\sqrt{3}\,l^3}$	$\frac{E\,s^3}{\sqrt{3}\,l^3}$	1

TABLE 1.3: Mechanical properties of honeycomb lattices, where E and ν are the Young's modulus and the Poisson's ratio of the constituent material, l is the length of the cell side, and s is in-plane thickness of the cell-walls.

in classical honeycomb structures may be of extensional or bending nature. The effective behaviour of honeycombs, with triangular and square micro-structures, are dominated by the axial deformations of its internal components [79], while the corresponding hexagonal lattice is dominated by cell-wall bending [37]. The same bending-dominated behaviour has been observed experimentally for the chiral lattice proposed in [48]. The mechanical properties for such topologies in terms of geometric parameters are listed in Table 1.3, where in this case l is the length of the cell side. In Fig. 1.25 we compare the effective Young's modulus E^* of the proposed auxetic lattices with those of the honeycombs micro-structures. The curves are shown for $p/s \geq 5$, in the range of validity of the beam theory, which has been used for the computation of the effective behaviour. For the purpose of comparison, we also consider the stiffness of the spring equal to the longitudinal stiffness of a single arm of the cross-shaped elements. We note that the auxetic lattices can reach values of E^* comparable with the corresponding honeycomb structures and that the square topology gives the stiffest behaviour, when the results are given in terms of relative density $\overline{\rho}^*$.

1.5 The lattice with Poisson's ratio close to -1

We conclude this chapter showing an experimental evidence of the square microstructured medium with Poisson's ratio approaching -1. The elements of the structure have been produced with a 3D printer (Dimension SST 1200es) in thermoplastic polymer ABS with two different colors, blue and white. In Fig. 1.26 some snapshots of the experiment are shown, the elastic structure is subjected to a uniaxial tension in horizontal direction. The images are taken at a distance of approximately 1.2m to the sample, which has been considered sufficient to minimize image distortions. The displacements of the junction points at the central

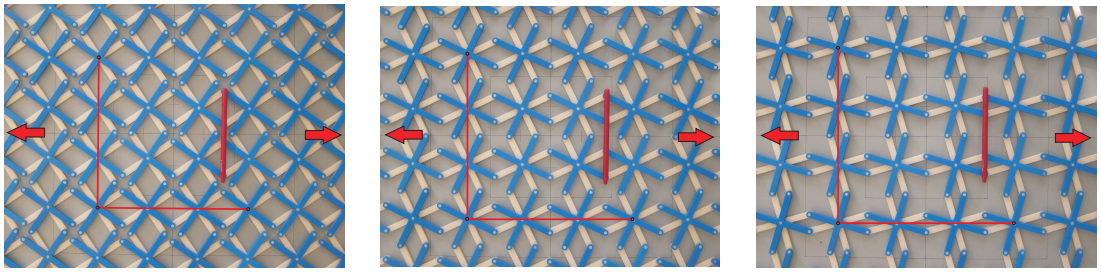

(a) (b) (c)

FIGURE 1.26: Deformation of the auxetic lattice subjected to an horizontal tensile traction. (a), (b) and (c) show three configurations of the structured media at increasing magnitude of deformation.

hinge of each couple of cross-shaped elements of different colors are equal to the macroscopic displacements of the perfectly periodic structure. The displacements of these junction points in the 4×4 central unit cells are tracked, to this purpose an algorithm for Image Processing in Matlab® (Release 2011b), has been implemented. During the experiment several pictures were taken with a high-definition camera, the image of our sample in the un-deformed state was compared with the images in the deformed state, resulting from the application of the load, to determine displacements and deformations of the junction points. Before to proceed with the comparisons the images were conveniently processed in order to obtain automatically the position of the points. The images have been adjusted to increase the contrast, after that they were converted to gray-scale by eliminating the hue and saturation information while retaining the luminance, and the background was removed. The Fig. 1.27 shows the images for three different steps of the experiment. To make easier the identification of the white circles, which centers represent the points of the lattice that move macroscopically, the gray-scale images were converted to binary images (Black-White), see Fig. 1.28. The

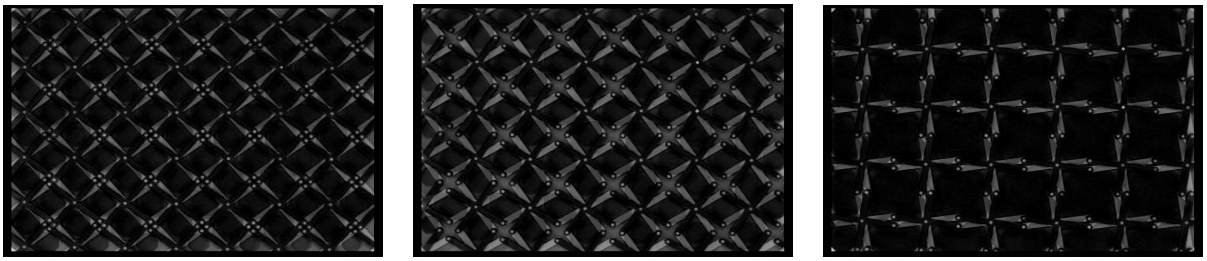

(a) (b) (c)

FIGURE 1.27: Images of the experiment in gray-scale. (a), (b) and (c) represent three different steps of the experiment.

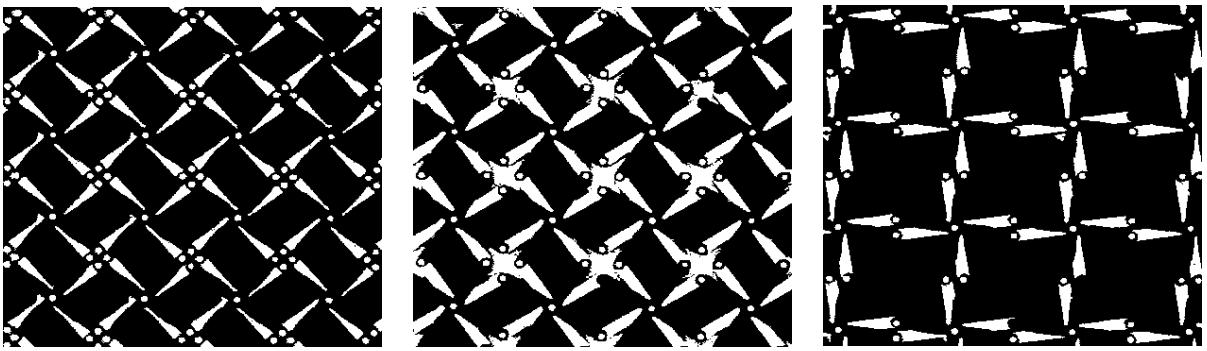

(a) (b) (c)

FIGURE 1.28: Binary images of the experiment. (a), (b) and (c) represent three different steps of the experiment.

output binary images have values of 1 (white) for all pixels in the input images with luminance greater than a set threshold and 0 (black) for all other pixels. The images were cut in order to operate only in the 4×4 central unit cells. The exterior boundary of the objects (each connected component) in the images, displayed in white in Fig. 1.28, were traced and a set of properties were measured.

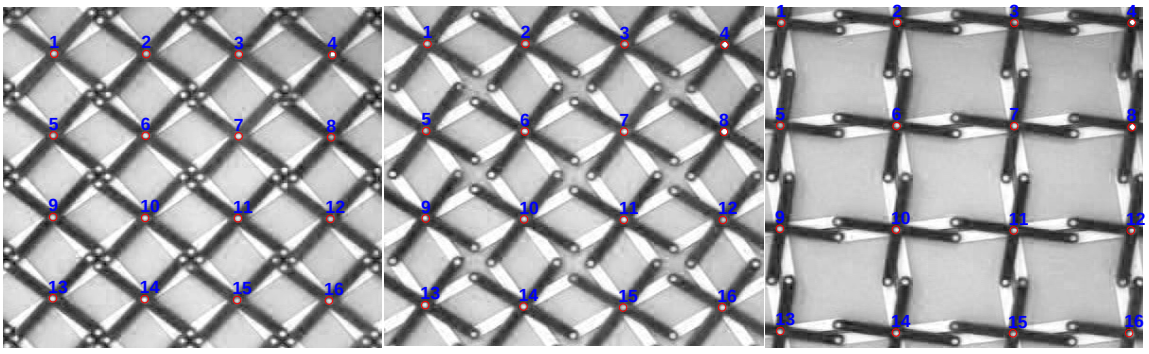

(a) (b) (c)

FIGURE 1.29: 16 joint points of the lattice of which were calculated the displacements. (a), (b) and (c) represent three different steps of the experiment.

Areas and perimeters were used because their ratio allow to identify the circles, which represent the hinges, discarding the other items, whereas centroids (center for circle) identify the geometric centers of two-dimensional regions, in our case the junction points that move macroscopically, see Fig. 1.29. In Fig. 1.30(a) the progressive position of these junction points is highlighted with white dots. The corresponding deformations are plotted in Fig. 1.30(b); the resulting Poisson's ratio is $\nu = -0.9931 \pm 0.0025$.

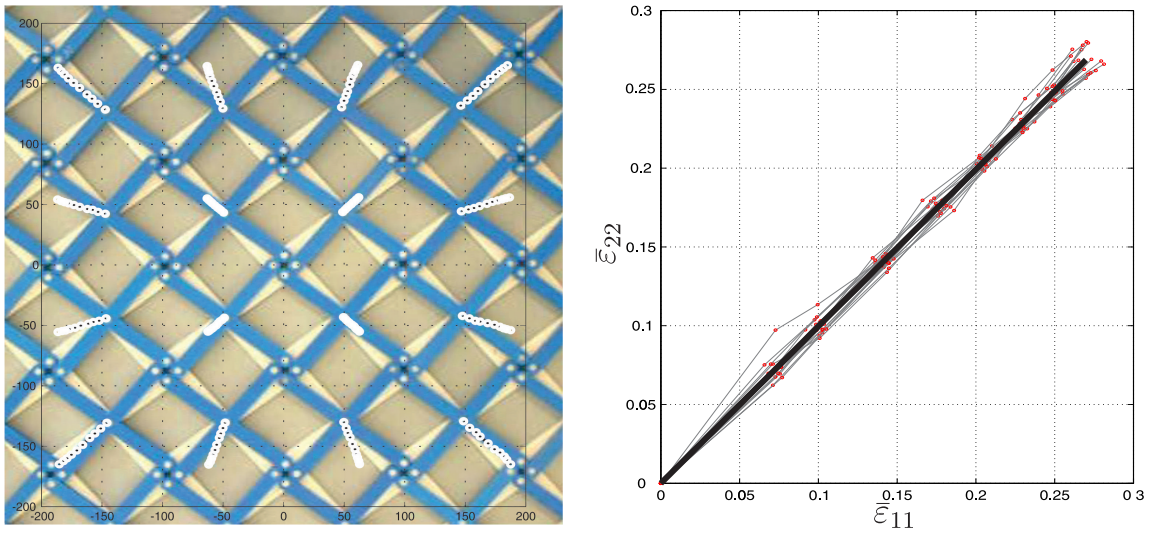

(a) (b)

FIGURE 1.30: Displacement and Poisson's ratio of the micro-structure. (a) The white dots indicate the progressive position of the central points in the 4×4 central unit cells of the structured media. (b) Deformations $\bar{\varepsilon}_{11}$ and $\bar{\varepsilon}_{22}$ as a result of the applied uniaxial stress $\bar{\sigma}_{11}$. The grey lines correspond to the points highlighted in part (a). The thick black line indicates the average deformation. The Poisson's ratio is equal to -0.9931 ± 0.0025.

The Poisson's ratio $\nu(t_i, p_j)$ is evaluated at any point p_j as a function of time t_i, where j varies between 1 and the number of points N and i between 1 and the number of instants of time N_T, the values of the Poisson's ratio $\nu(t_i, p_j)$ are given in Appendix B, Table B.1 and Table B.2. The sample mean of $\nu(t_i, p_j)$, at any time t_i, is:

$$\bar{\nu}(t_i) = \sum_{j=1}^{N} \frac{\nu(t_i, p_j)}{N}. \tag{1.73}$$

The sample standard deviation of $\nu(t_i, p_j)$ is:

$$\sigma_\nu(t_i) = \sqrt{\frac{\sum_{j=1}^{N} (\nu(t_i, p_j) - \bar{\nu}(t_i))^2}{N-1}} \tag{1.74}$$

The standard error of the mean is:

$$\delta_\nu(t_i) = \frac{\sigma_\nu(t_i)}{\sqrt{N}}. \tag{1.75}$$

The Poisson's ratio $\nu(t_i)$, at any time, is $\nu(t_i) = \bar{\nu}(t_i) \pm \delta_\nu(t_i)$. To evaluate a single value of the Poisson's ratio ν, the weighted mean of $\bar{\nu}$ have been calculated:

$$\bar{\nu} = \frac{\sum_{i=1}^{N_T} \omega_i \bar{\nu}_m(t_i)}{\sum_{i=1}^{N_T} \omega_i} = -0.9931, \tag{1.76}$$

where the weights are:

$$\omega_i = \frac{1}{\delta_\nu^2(t_i)}. \tag{1.77}$$

The error that is assigned to ν is obtained by applying the formula of error propagation calculated using the relation:

$$\delta_\nu = \frac{1}{\sqrt{\sum_{i=1}^{N_T} \omega_i}} = 0.0025. \tag{1.78}$$

The values of the sample mean $\bar{\nu}(t_i)$ obtained from eqn. (1.73), the sample standard deviation $\sigma_\nu(t_i)$ obtained from eqn. (1.74), the standard error of the mean $\delta_\nu(t_i)$ obtained from eqn. (1.75), and the weights ω_i obtained from eqn. (1.77), are given in Appendix B, Table B.3. Finally, the Poisson's ratio ν, is $\nu = \bar{\nu} \pm \delta_\nu = -0.9931 \pm 0.0025$. Reducing the number of points the values of ν range from $\nu = -0.9956 \pm 0.0028$ to $\nu = -0.9929 \pm 0.0026$.

Chapter 2

3D Cubic and isotropic lattices with Negative Poisson's ratio

2.1 Introduction

In the previous Chapter we described three plane micro-structure which can exhibit under particular condition auxetic behaviour tending to the limit -1. Now we want to extend the study to a three-dimensional model that can reproduce the same particular feature. Different models are known to have auxetic behaviour, among these we mention re-entrant structures and rotating structures. One of the earliest auxetic models was proposed by Almgren [32], it is a re-entrant three-dimensional structure of rods, hinges, and springs with macroscopic Poisson's ratio $\nu = -1$ in some directions. Other models based on re-entrant cells were proposed by Evans et al. [38], by Gibson and Ashby [37], and by Choi and Lakes [39, 40] that transformed the cell of conventional foam from the convex polyhedral shape to a concave or 're-entrant' shape. A different mechanism made of rotating rigid units can exhibit auxetic behaviour as proposed by Grima and Attard [81], it is composed from rigid cuboids connected at their edges, which deform through relative rotation with respect to each other. They derive analytically the Poisson's ratio and the Young's modulus and it is shown that for loading on-axis, the system exhibits negative values for all the six on-axis Poisson's ratios. The use of three-dimensional models to predict or to explain auxetic behaviour is used by Alderson and Evans [82, 83, 84] which apply a three-dimensional rotating and/or dilating tetrahedral model to real crystalline auxetic materials such as α-cristobalite and

α-quartz structures of both silica and germania. Auxetic responses have been demonstrated possible in many crystals [7], and some artificial three-dimensional auxetic materials have been proposed especially with the coming of the 3D-printer. A new material, named 'Bucklicrystals', achieves a three-dimensional auxetic behavior through the elastic buckling [57]. In [56] it is described a dilatational three-dimensional cubic auxetic material with an ultimate Poisson's ratio of $\nu = -1$, based on a two-dimensional conceptual model recently published [73], the model is studied numerically with a F.E.M. program and a sample is fabricated with a 3D-printer. The development of the modern 3D-printers has allowed the creation of meta-materials starting from theoretical models with unit cells in the micro-meter range, in [85] for the first time the authors fabricated and characterized a truly three-dimensional crystalline mechanical meta-materials with unit cells in the micro-meter range and with adjustable Poisson's ratios, including negative values. They modified appropriately the DLW technology (Direct laser writing), that allows to create three-dimensional nano- and micro-structures height only some tens of micro-meters, to get larger structures, and they apply this new approach, called dip-in 3D-DLW, to a model previously introduced in [37]. To obtain an auxetic behaviour we choose to extend to three dimension the square lattice, studied previously. The system, we will introduce, has an elementary cell with the shape of a cube, making an analogy with crystallography, it could be seen as a cubic (or isometric) crystal system. We will propose two different versions of the cubic lattice, one can be imagined as a Primitive cubic (abbreviated cP and alternatively called simple cubic) and the other one as a Body-centered cubic (abbreviated cB or bcc). As we will see later these two different systems are generally anisotropic, or more precisely cubic according to symmetry consideration, but one of them can be modified in its structural properties so that the macroscopic behaviour becomes isotropic. The anisotropic elastic character of the material is obviously reflected on the effective Young's modulus E^* and on the effective Poisson's ratio ν^*, which are therefore a function of the direction in the solid. Henceforth the Young's modulus will be expressed as $E^* = E^*(\mathbf{n})$ and the Poisson's ratio as $\nu^* = \nu^*(\mathbf{n}, \mathbf{m})$ to emphasize the directional dependence, where $\mathbf{n}$ and $\mathbf{m}$ are two orthogonal directional vectors. The Young's modulus function will be identified by the direction $\mathbf{n}$ along it is applied a simple tension, whereas Poisson's ratio needs also to know the direction $\mathbf{m}$ along it is measured the contraction. Let $\mathbf{n}$, $\mathbf{m}$ and $\mathbf{t}$ be mutually orthogonal unit vectors and let x'_i $(i = 1 \dots 3)$ be a new coordinate system in which the x'_1, x'_2, x'_3 axes are along the vectors $\mathbf{n}$, $\mathbf{m}$ and $\mathbf{t}$, respectively.

To identify the direction of the vectors, we will refer to the angles ϕ, β and θ. The two angles ϕ, β identify the direction of the vector $\mathbf{n}$ in spherical coordinates, whereas the angle θ identifies the direction of the vector $\mathbf{m}$. For brevity directions are also described using crystallographic notation, e.g. $\mathbf{n}$=110 is the unit vector $(1/\sqrt{2}, 1/\sqrt{2}, 0)$, characterized by $\phi = \pi/4$, $\beta = \pi/2$. In Fig. 2.1 are shown some directions which will be useful in the rest of the work. The point [100] is along

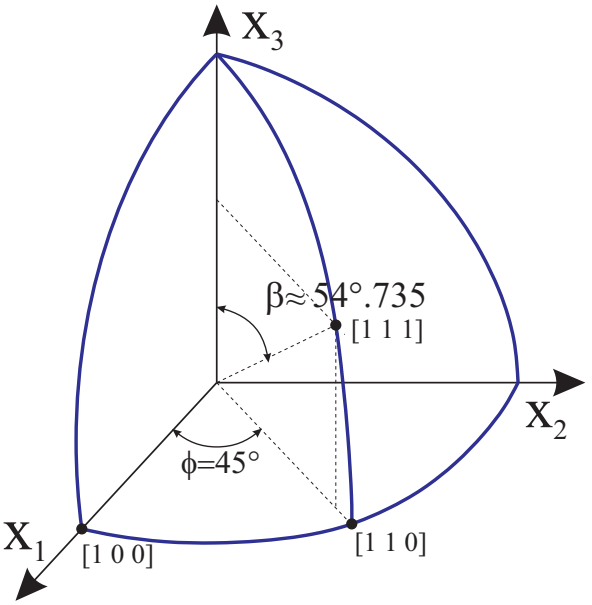

FIGURE 2.1: Crystallographic notation for the directions of the vectors $\mathbf{n}$, $\mathbf{m}$, $\mathbf{t}$.

the coordinate axe x_1 ($\phi = 0$ and $\beta = \pi/2$), the point [110] is along the line that bisects the coordinate plane $x_1 - x_2$ ($\phi = \pi/4$ and $\beta = \pi/2$), and the point [111] is along the line that trisects the octant of the coordinate system ($\phi = \pi/4$ and $\beta = \arccos(1/\sqrt{3})$).

The type of elastic anisotropy of the material is reflected in the symmetries of the fourth-order elasticity stiffness tensor $\mathbb{C}$ or its inverse, the compliance tensor $\mathbb{S} = \mathbb{C}^{-1}$, here always supposed to be positive definite. In a fixed rectangular coordinate system x_i ($i = 1 \dots 3$), the stress-strain relation can be written as

$$\varepsilon_{ij} = S_{ijkl}\sigma_{kl}, \quad S_{ijkl} = S_{jikl} = S_{klij} = S_{ijlk}, \tag{2.1}$$

where ε_{ij} and σ_{ij} are the strain and stress and S_{ijkl} is the elastic compliance. The S_{ijkl} is positive definite and possesses the full symmetry shown in eqn. (2.1). In view of more tractable computation, a change of notation is now performed. We

evaluate the three-dimensional Hooke's law, for a full anisotropic solid, by the following Voigt's notation:

$$\begin{bmatrix} \sigma_{11} \\ \sigma_{22} \\ \sigma_{33} \\ \sigma_{23} \\ \sigma_{31} \\ \sigma_{12} \end{bmatrix} = \begin{bmatrix} s_{1111} & s_{1122} & s_{1133} & 2s_{1123} & 2s_{1131} & 2s_{1112} \\ s_{1122} & s_{2222} & s_{2233} & 2s_{2223} & 2s_{2231} & 2s_{2212} \\ s_{1133} & s_{2233} & s_{3333} & 2s_{3323} & 2s_{3331} & 2s_{3312} \\ 2s_{1123} & 2s_{2223} & 2s_{3323} & 4s_{2323} & 4s_{2331} & 4s_{2312} \\ 2s_{1131} & 2s_{2231} & 2s_{3331} & 4s_{2331} & 4s_{3131} & 4s_{3112} \\ 2s_{1112} & 2s_{2212} & 2s_{3312} & 4s_{2312} & 4s_{3112} & 4s_{1212} \end{bmatrix} \cdot \begin{bmatrix} \varepsilon_{11} \\ \varepsilon_{22} \\ \varepsilon_{33} \\ \varepsilon_{23} \\ \varepsilon_{31} \\ \varepsilon_{12} \end{bmatrix} \tag{2.2}$$

Although this notation provides a vector and matrix representation of the tensors which is physically meaningful, it shows nonetheless a loss of tensorial character. In view of defining the material symmetries that will be considered in this paper, a special reference system is introduced. For the symmetry under investigation, the matrix representation of the elasticity tensor, written in the principal reference system, defined as a system of coordinates in which the elasticity tensor shows the fewest number of independent non-zero components, can be simplified as

$$\begin{bmatrix} \sigma_{11} \\ \sigma_{22} \\ \sigma_{33} \\ \sigma_{23} \\ \sigma_{31} \\ \sigma_{12} \end{bmatrix} = \begin{bmatrix} s_{1111} & s_{1122} & s_{1133} & 0 & 0 & 0 \\ s_{1122} & s_{2222} & s_{2233} & 0 & 0 & 0 \\ s_{1133} & s_{2233} & s_{3333} & 0 & 0 & 0 \\ 0 & 0 & 0 & 4s_{2323} & 0 & 0 \\ 0 & 0 & 0 & 0 & 4s_{3131} & 0 \\ 0 & 0 & 0 & 0 & 0 & 4s_{1212} \end{bmatrix} \cdot \begin{bmatrix} \varepsilon_{11} \\ \varepsilon_{22} \\ \varepsilon_{33} \\ \varepsilon_{23} \\ \varepsilon_{31} \\ \varepsilon_{12} \end{bmatrix} \tag{2.3}$$

In Section 2.2 we describe a three-dimensional lattice with negative Poisson's ratio characterized by cubic symmetry, so that $S_{1111} = S_{2222} = S_{3333}$, $S_{1122} = S_{1133} = S_{2233}$ and $S_{2323} = S_{3131} = S_{1212}$, and we will analyze the directional dependance of the Poisson's ratio and of the Young's modulus directing our attention to the global minimum. Then in Section 2.3 the configuration of the lattice will be modified to produce isotropic symmetry under appropriate conditions.

2.2 Poisson's ratio and Young's modulus for three-dimensional cubic lattice

We tessellate the space building a cubic cells, as in Fig. 2.2. If we do a similarity with crystallographic systems the elementary cell of the structure can be seen as a primitive cubic system (cP) with one lattice point on each corner of the cube, it is composed of slender crosses with length of the arms p and springs with stiffness equal to k_L, so classical structural theories can be conveniently applied to analyse the response of the elastic system. In Fig. 2.2 the crosses are depicted in red and blue while the springs in green, each couple of red and blue crosses is mutually constrained to have the same displacement at the central point where a hinge is introduced. Different couples are then constrained by internal hinges at the external end of each arm.

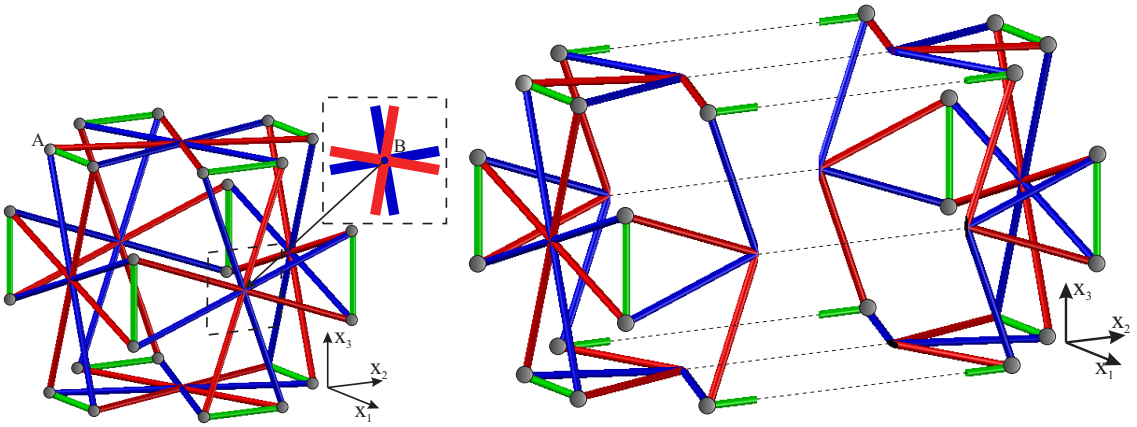

(a) (b)

FIGURE 2.2: (a) Three-dimensional cell of the cubic lattice. (b) Three-dimensional cell of the cubic lattice, cutted by a parallel plane to $x_1 - x_3$.

In particular, each arm of a single cross-shaped element is modelled as an Euler beam undergoing flexural and extensional deformations. Each beam has Young's modulus E, cross-sectional area A and second moment of inertia J. We also introduce the non-dimensional stiffness ratio parameters $\alpha_1 = k_L p/(EA)$. The structure has been studied numerically with the finite element code, Comsol Multiphysics®, referring to an elementary cell to which was applied the appropriate periodic boundary conditions to approximate the infinite system conditions of periodicity. The calculations are performed, unless otherwise specified, considering the Young's modulus of the iron $E = 200000[MPa]$, the length of the arms $p = 1000$ $[mm]$ and a circular cross section with radius $r = 25$ $[mm]$.

The micro-structured medium falls within the class of uni-mode materials with dilatation as the only easy mode of deformation. The periodic structure has a Bravais periodic lattice [77] consisting of points

$$\mathbf{R} = n_1\mathbf{t}_1 + n_2\mathbf{t}_2 + n_3\mathbf{t}_3 \tag{2.4}$$

where $n_{1,2,3}$ are integers and $\mathbf{t}_{1,2,3}$ the primitive vectors spanning the lattice. Following the systematic analysis for finite deformation as in Chapter 1 for the square lattice we conclude that the lattice is a unimode material. Let

$$\mathbf{T} = \begin{bmatrix} \mathbf{t}_1 & \mathbf{t}_2 & \mathbf{t}_3 \end{bmatrix} \tag{2.5}$$

be the 'lattice matrix'. The Cauchy-Green tensor is a path:

$$\mathbf{C}(t, t_0) = [\mathbf{T}(t_0)]^{-T}[\mathbf{T}(t)]^T[\mathbf{T}(t)][\mathbf{T}(t_0)]^{-1} = \left(\frac{\sin\gamma}{\sin\gamma_0}\right)^2 \mathbf{I}. \tag{2.6}$$

As for the planar square lattice the possible paths $\mathbf{C}(t, t_0)$, for any Bravais lattice, lie on the same one-dimensional curve materials. The lattice structure presents cubic behaviour, so that we need to determine three elastic moduli, the cubic case represents the symmetry with the lesser number of independent elastic constants, excluding the isotropic case. As explained in the Introduction, here and in the following it is preferable to express the components of the elastic compliance tensor $\mathbb{S}$ in the Voigt's contracted notation which allows to construct, in the principal material Cartesian reference frame, the compliance matrix in the form:

$$S^* = \begin{bmatrix} s_{11} & s_{12} & s_{12} & 0 & 0 & 0 \\ s_{12} & s_{11} & s_{12} & 0 & 0 & 0 \\ s_{12} & s_{12} & s_{11} & 0 & 0 & 0 \\ 0 & 0 & 0 & 4s_{44} & 0 & 0 \\ 0 & 0 & 0 & 0 & 4s_{44} & 0 \\ 0 & 0 & 0 & 0 & 0 & 4s_{44} \end{bmatrix} \tag{2.7}$$

where the reduced elastic coefficients are defined as $s_{11} = S_{1111} = S_{2222} = S_{3333}$, $s_{12} = S_{1122} = S_{1133} = S_{2233}$, $s_{44} = S_{2323} = S_{3131} = S_{1212}$. The conditions for the strain energy density to be positive definite are, as shown in [86]:

$$s_{11}s_{12} > 0, \quad s_{11} + 2s_{12} > 0, \quad s_{44} > 0 \tag{2.8}$$

The elastic compliance S'_{1111} and S'_{1122}, if a Cartesian orthogonal reference frame $Ox_1x_2x_3$ is considered, are:

$$S'_{1111} = n_i n_j n_k n_l S_{ijkl} = s_{11}(n_1^4+n_2^4+n_3^4)+(2s_{11}+4s_{44})(n_1^2n_2^2+n_1^2n_3^2+n_2^2n_3^2), \quad (2.9)$$

$$\begin{aligned} S'_{1122} = n_i n_j n_k n_l S_{ijkl} = s_{11}(n_1^2t_1^2 + n_2^2t_2^2 + n_3^2t_3^2) + s_{12}(t_1^2n_2^2 + t_2^2n_1^2 + t_1^2n_3^2 + t_3^2n_1^2+ \\ + t_2^2n_3^2 + t_3^2n_2^2) + 4s_{44}(n_1n_2t_1t_2 + n_1n_3t_1t_3 + n_2n_3t_2t_3); \end{aligned} \quad (2.10)$$

where indices i, j, k and l range from 1 to 3, and the usual rule of sum over a repeated subscript is assumed. The expression $E^* = E^*(\mathbf{n})$ can be written, using eqn. (2.9), in index form as:

$$\frac{1}{E^*(\mathbf{n})} = S'_{1111} = s_{11}(n_1^4 + n_2^4 + n_3^4) + (2s_{11} + 4s_{44})(n_1^2n_2^2 + n_1^2n_3^2 + n_2^2n_3^2); \quad (2.11)$$

which, making use of the identity:

$$n_1^4 + n_2^4 + n_3^4 = 1 - 2(n_1^2n_2^2 + n_1^2n_3^2 + n_2^2n_3^2), \quad (2.12)$$

can be rewritten as:

$$\frac{1}{E^*(\mathbf{n})} = s_{11} - (2s_{11} - 2s_{12} + 4s_{44})(n_1^2n_2^2 + n_1^2n_3^2 + n_2^2n_3^2). \quad (2.13)$$

We rewrite S'_{1122} in eqn. (2.10) making use of the following identities:

$$\begin{aligned} 1 - (n_1^2t_1^2 + n_2^2t_2^2 + n_3^2t_3^2) &= (t_1^2n_2^2 + t_2^2n_1^2 + t_1^2n_3^2 + t_3^2n_1^2 + t_2^2n_3^2 + t_3^2n_2^2), \\ (n_1^2t_1^2 + n_2^2t_2^2 + n_3^2t_3^2) &= (n_1n_2t_1t_2 + n_1n_3t_1t_3 + n_2n_3t_2t_3), \end{aligned} \quad (2.14)$$

so that we have

$$S'_{1122} = s_{12} + (s_{11} - s_{12} - 2s_{44})(n_1^2m_1^2 + n_2^2m_2^2 + n_3^2m_3^2); \quad (2.15)$$

therefore, the Poisson's ratio $\nu^*(\mathbf{n}, \mathbf{m})$ is

$$\nu^*(\mathbf{n}, \mathbf{m}) = -\frac{S'_{1122}}{S'_{1111}} = -\frac{s_{12} + (s_{11} - s_{12} - 2s_{44})(n_1^2m_1^2 + n_2^2m_2^2 + n_3^2m_3^2)}{s_{11} - 2(s_{11} - s_{12} - 2s_{44})(n_1^2n_2^2 + n_2^2n_3^2 + n_3^2n_1^2)}. \quad (2.16)$$

2.2.1 Young's modulus for three-dimensional cubic lattice

The Young's modulus for the cubic case depends on all three elastic constants s_{11}, s_{12} and s_{44}, see eqn. (2.13). In Fig. 2.3 it is illustrated the Young's modulus $E^* = E^*(\mathbf{n})$ of the cubic lattice for $\alpha_1 = 0.000515$, it is possible to see the cubic mechanical behaviour and the strong variation with respect to the direction $\mathbf{n}$. $E^* = E^*(\mathbf{n})$ can be effectively represented by means of a three-dimensional plot, that is, with a surface generated by the vector $\mathbf{n}$ where the distance from the origin is proportional to the value of the Young's modulus in the direction pointed by the vector itself.

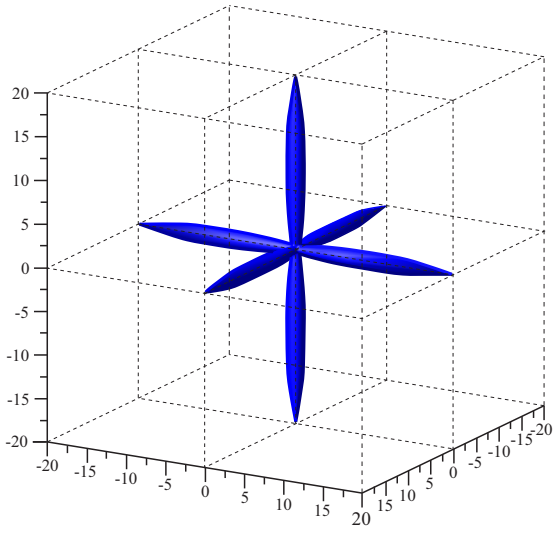

FIGURE 2.3: Three-dimensional representation of the Young's module E^* in the cubic lattice.

In Fig. 2.4 is also shown a polar plot of the Young's modulus $E^* = E^*(\mathbf{n})$ for $\alpha_1 = 0.000515$ when the unit vector $\mathbf{n}$ is directed in turn along the coordinate plane $x_1 - x_2$ ($\beta = \pi/2$).

To emphasize the anisotropic behaviour the eqn. (2.13) can be rewritten as

$$\frac{1}{E^*(\mathbf{n})} = s_{11} - \beta_1(n_1^2 n_2^2 + n_1^2 n_3^2 + n_2^2 n_3^2), \tag{2.17}$$

introducing the anisotropic coefficient β_1 that depends on material properties only. It should be noticed that β_1 is related to the dimensionless Zener anisotropy factor β_{cub}

$$\beta_{cub} = \frac{2(s_{11} - s_{12})}{4s_{44}}, \tag{2.18}$$

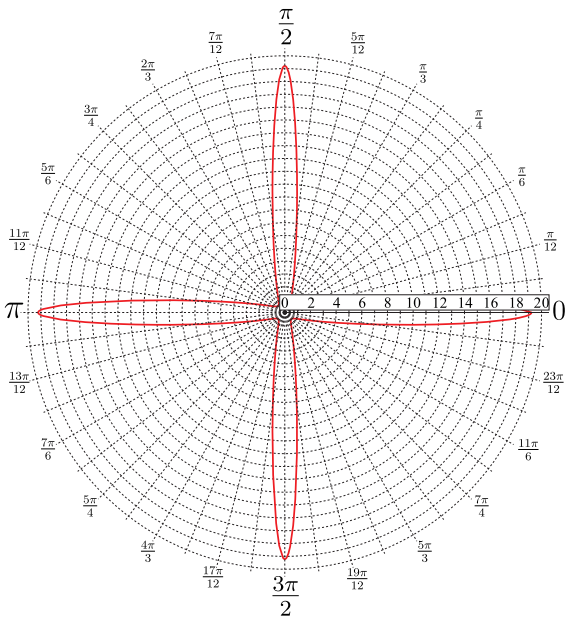

FIGURE 2.4: Polar diagrams of the Young's modulus E^* as a function of the angle ϕ. Results are given for: the angle $\beta = \pi/2$ and the non-dimensional stiffness ratio $\alpha_1 = 0.000515$.

used in the literature about cubic materials, by the following relationship

$$\beta_1 = 4s_{44}(\beta_{cub} - 1). \tag{2.19}$$

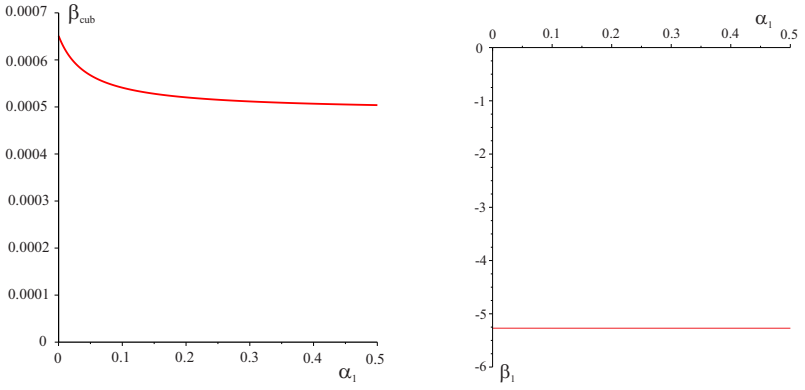

(a) (b)

FIGURE 2.5: Zener anisotropic factor β_{cub} and anisotropic coefficient β_1 for the lattice as a function of the non-dimensional stiffness ratio α_1. (a) β_{cub} as a function of α_1. (b) β_1 as a function of α_1.

In case of isotropic behaviour the Zener anisotropic factor and the anisotropic coefficient are equal to $\beta_1 = 0$ and $\beta_{cub} = 1$ respectively, and they are linked to

the relative shear stiffness of the material, as described in [87]. We can say that when $\beta_1 < 0$ the material has low relative shear stiffness whereas when $\beta_1 > 0$ the material has high relative shear stiffness. In Fig. 2.5 are depicted the two factors β_{cub} and β_1 for the cubic lattice as a function of α_1. In our case β_1 is negative and as confirmed in Fig. 2.6 the shear stiffness of the lattice is low.

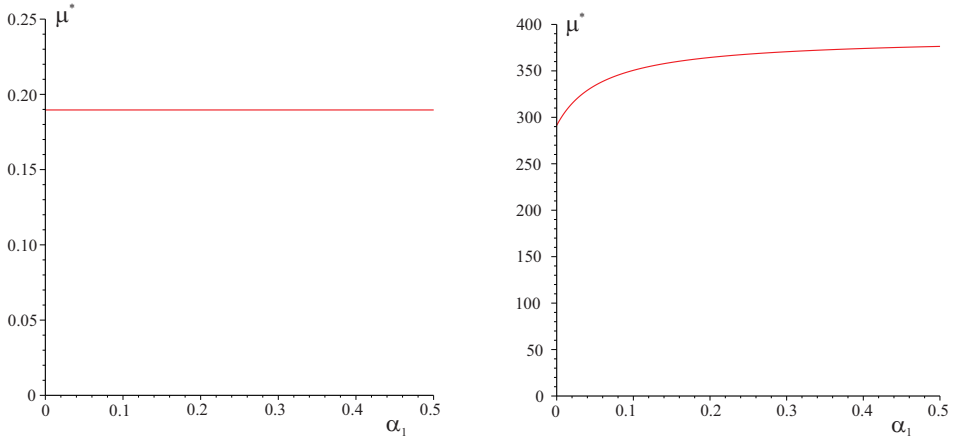

(a) (b)

FIGURE 2.6: Shear modulus μ^* of the lattice as a function of the non-dimensional stiffness ratio α_1. (a) Shear modulus of the cubic lattice. (b) Shear modulus in case of isotropic behaviour, $\mu^* = E^*/(2(1+\nu^*))$.

Returning to the evaluation of the extrema of the the Young's modulus, we find the directions $\mathbf{n}$ which correspond to critical points. First we consider the situation

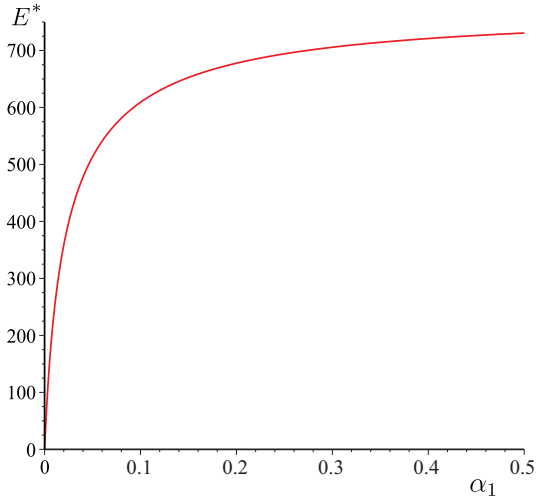

FIGURE 2.7: Maximum Young's modulus E^* in [100] as a function of the non-dimensional stiffness ratio α_1.

when $\mathbf{n}$ matches each coordinate axis. In this case there are six stationary points,

each according to $n_i = \pm 1$ (i=1 ... 3), and the value of Young's modulus is:

$$E^*(\mathbf{n}) = \frac{1}{s_{11}}. \tag{2.20}$$

The $E^*(\mathbf{n})$ valued in a coordinate axis, $\mathbf{n}$ directed as [100], is shown in Fig. 2.7 as a function of the non-dimensional stiffness ratio α_1. The second case is when the unit vector $\mathbf{n}$ is directed in turn along the bisectors of each coordinate plane. The 12 stationary points are those for which $n_i = \pm 1/\sqrt{2}$, $n_j = \pm 1/\sqrt{2}$ and $n_k = 0$ $(i, j, k = 1 \ldots 3, i \neq j \neq k)$, and the Young's modulus is given by:

$$E^*(\mathbf{n}) = \frac{4}{4s_{11} - \beta_1} = \frac{4}{2s_{11} + 2s_{12} + 4s_{44}}; \tag{2.21}$$

In Fig. 2.8 are shown the values of $E^*(\mathbf{n})$ in the diagonal direction [110] as a function of the non-dimensional stiffness ratio α_1.

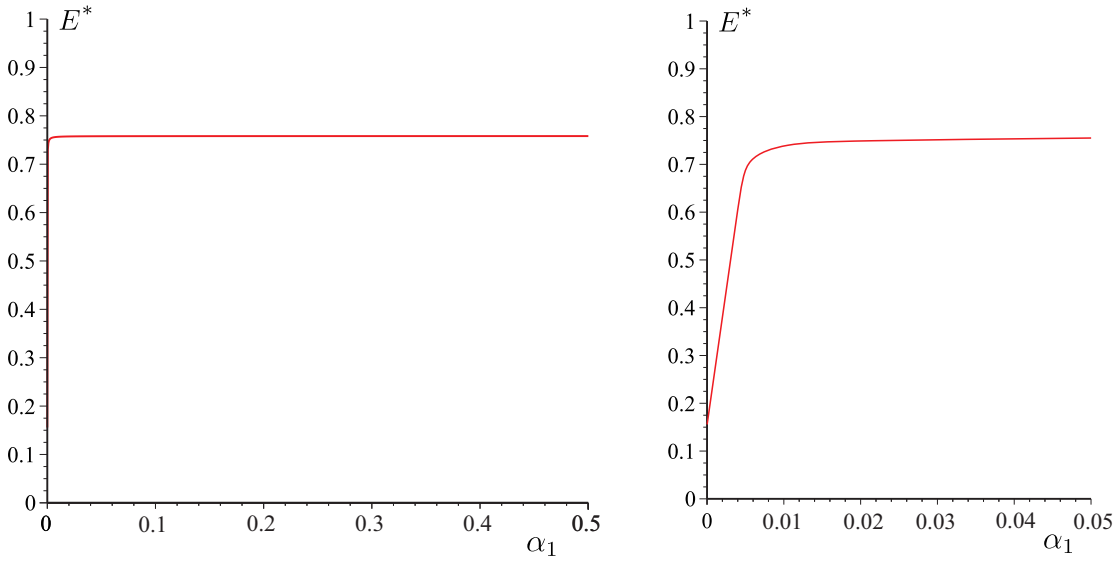

(a) (b)

FIGURE 2.8: Young's modulus E^* in [110] as a function of the non-dimensional stiffness ratio α_1. (a) Young's modulus between $\alpha_1 = 0$ and $\alpha_1 = 0.5$. (b) Young's modulus between $\alpha_1 = 0$ and $\alpha_1 = 0.05$.

The last case is when the unit vector $\mathbf{n}$ trisects each octant of the coordinate system. This case produces eight stationary points: $n_i = \pm 1/\sqrt{3}$, $n_j = \pm 1/\sqrt{3}$ and $n_k = \pm 1/\sqrt{3}$ $(i, j, k = 1 \ldots 3, i \neq j \neq k)$, and the elastic modulus is:

$$E^*(\mathbf{n}) = \frac{3}{3s_{11} - \beta_1} = \frac{3}{s_{11} + 2s_{12} + 4s_{44}}. \tag{2.22}$$

In Fig. 2.9 are visualized the values of $E^*(\mathbf{n})$ in the direction [111] as a function of the non-dimensional stiffness ratio α_1.

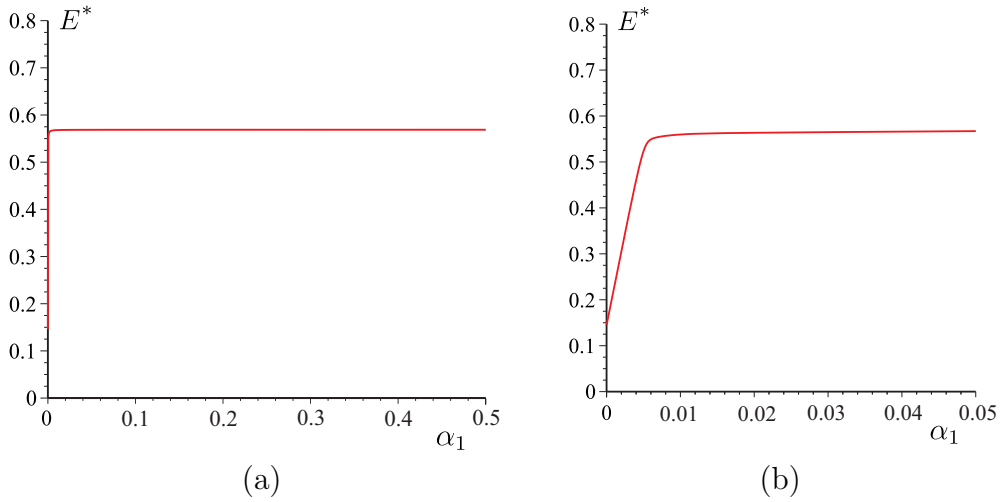

FIGURE 2.9: Minimum Young's modulus E^* in [111] as a function of the non-dimensional stiffness ratio α_1. (a) Young's modulus between $\alpha_1 = 0$ and $\alpha_1 = 0.5$. (b) Young's modulus between $\alpha_1 = 0$ and $\alpha_1 = 0.05$.

From the previous plots, we can conclude that $E^*_{max} = 1/s_{11}$ and $E^*_{min} = 3/(s_{11} + 2s_{12} + 4s_{44})$, confirming the claims made in [87] for a lattice with low shear stiffness $\beta_1 < 0$, in case of $\beta_1 > 0$ we would have had $E^*_{min} = 1/s_{11}$ in direction [100], eqn. (2.20), and $E^*_{max} = 3/(s_{11} + 2s_{12} + 4s_{44})$ in direction [111], eqn. (2.22)

2.2.2 Poisson's ratio for three-dimensional cubic lattice

We know that Poisson's ratio is strictly bounded between -1 and $1/2$ in isotropic solids in order to stable constitutive law, but such simple bounds do not exist for anisotropic solids, even for those 'closest' to isotropy such as the cubic material. Ting and Chen (2005) demonstrated that arbitrarily large positive and negative values of Poisson's ratio could occur in solids with cubic material symmetry. The key requirement is that the Young's modulus in the 111-direction is very large (relative to other directions), and as a consequence the Poisson's ratio for stretch close to but not coincident with the 111-direction can be large, positive or negative. Ting and Chen replace conventional belief (e.g. Baughman et al. 1998) that the extreme values of $\mathbf{n}$ are associated with stretch along the face diagonal (110-direction). It is more complicated to find the locations of the extremes of $\nu^*(\mathbf{n}, \mathbf{m})$ for cubic materials for all possible choices of the vectors $\mathbf{n}$ and $\mathbf{m}$ with $\mathbf{n} \cdot \mathbf{m} = 0$,

indeed it is necessary to consider general $\mathbf{n}$ and $\mathbf{m}$. The specification of $\mathbf{n}$ and $\mathbf{m}$ requires three parameters such as ϕ, β and θ. We can take the derivatives of $\nu^*(\mathbf{n},\mathbf{m})$ with respect to the three parameters and set the results to zero. Instead, once $\mathbf{n}$ is supposed to be given, $\mathbf{m}$ depends on just one parameter and so the $\mathbf{m}$ that gives the extremes of $\nu^*(\mathbf{n},\mathbf{m})$ is:

$$\mathbf{m} = \frac{\cos\theta}{\sqrt{1-n_3^2}}\begin{bmatrix} n_2 \\ n_1 \\ 0 \end{bmatrix} + \frac{\sin\theta}{\sqrt{1-n_3^2}}\begin{bmatrix} -n_1 n_3 \\ -n_2 n_3 \\ 1-n_3^2 \end{bmatrix}, \quad n_3^2 \neq 1, \tag{2.23}$$

where θ is arbitrary. Inserting 2.23 into 2.16 and setting the derivative of $\nu^*(\mathbf{n},\mathbf{m})$ with θ to zero gives:

$$\tan 2\theta = \frac{n_1 n_2 n_3 (n_2^2 - n_1^2)}{n_1^2 n_2^2 (1+n_3^2) - n_3^2 (1-n_3^2)^2}. \tag{2.24}$$

θ is a solution of 2.24, so is $\theta + \pi/2$.

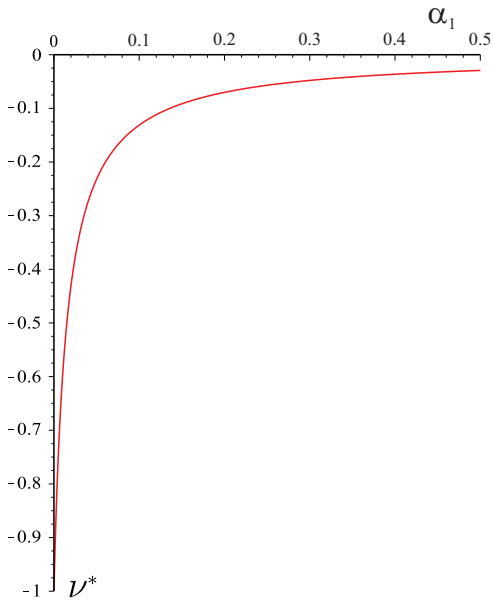

FIGURE 2.10: Poisson's ratio ν_0^* as a function of the non-dimensional stiffness ratio α_1.

Thus, for each $\mathbf{n}$, there are two $\mathbf{m}$ that provide the extrema. Now let's focus on two particular directions $\mathbf{n} = 111$ and $\mathbf{n} = 001$, these are the only two directions for which $\nu^*(\mathbf{n},\mathbf{m})$ is independent of $\mathbf{m}$. In case of $\mathbf{n} = 001$ is $\nu_0^* = \nu^*(001,-) = -s12/s11$ whereas for $\mathbf{n} = 111$ is

$$\nu^*_{111} = \nu^*(111, -) = -\frac{s_{11} + 2s_{12} - 2s_{44}}{s_{11} + 2s_{12} + 4s_{44}}. \tag{2.25}$$

When $s_{44} \to 0$, we obtain $\nu^*_{111} \simeq -1$. Fig. 2.10 shows the Poisson's ratio ν^*_0 of our lattice, when the direction of the simple tension is along a symmetry principal axes (100), (010) or (001) and the lateral contraction is measured in an orthogonal one, as a function of the non-dimensional stiffness ratio α_1. As we can see, reducing the value of α_1 the Poisson's ratio tends to -1. If we change the direction of the vector $\mathbf{n}$ we can visualize through the polar plot in Fig. 2.11, for $\alpha_1 = 0.000515$, the Poisson's ratio as the position of the vector $\mathbf{m}$ changes. We have considered three different positions of the vector $\mathbf{n}$ on the symmetry plane characterized by $\beta = \pi/2$. Among the infinite values of the Poisson's ratio the minimum and the maximum are given when the angle θ, that determines $\mathbf{m}$, assumes the values in eqn. (2.23).

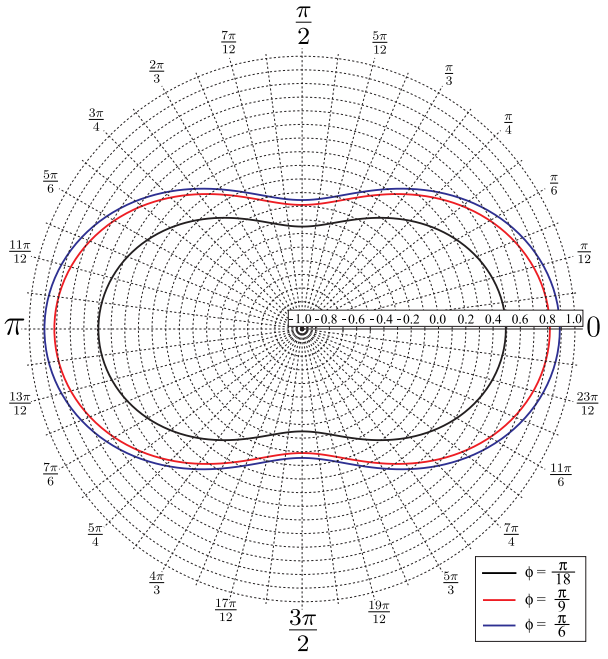

FIGURE 2.11: Polar diagrams of the Poisson's ratio as a function of the angle θ which determines the position of $\mathbf{m}$. Results are given for three different values of the angle ϕ, for the angle $\beta = \pi/2$ and for the non-dimensional stiffness ratio $\alpha_1 = 0.000515$.

We can see that for $\beta = \pi/2$ and $\phi = \pi/18$, $\pi/9$ and $\pi/6$ ν^* varies between a local maximum at $\theta = 0, \pi$ and a local minimum at $\theta = \pm\pi/2$. We want now to consider the global extremes of $\nu^*(\mathbf{n}, \mathbf{m})$ over all directions $\mathbf{n}$ and $\mathbf{m}$. For an anisotropic elastic material general conditions can be derived for the Poisson's ratio to be stationary. These conditions may be obtained by considering the derivative of $\nu^*(\mathbf{n}, \mathbf{m})$ with respect to rotation of the pair $(\mathbf{n}, \mathbf{m})$ and setting the results

to zero. Following symmetry considerations the analysis can be reduced to the irreducible spherical sector delimited by directions $\mathbf{n} = 100, 110, 111$ which corresponds to $1/48th$ of the unit sphere surface as shown in Fig. 2.12 where A, B and C correspond to $\mathbf{n} = 100, 110$ and 111. It could be shown that there are no stationary values of $\nu^*(\mathbf{n}, \mathbf{m})$ inside the spherical sector of Fig. 2.12 but only on its boundaries, see [88]. Hence, the only possible stationary values are on the edges. We follow the local maximum and minimum Poisson's ratio when $\mathbf{n}$ moves along the path $A-B-C-A$ visualized in green in Fig. 2.12 and the direction of $\mathbf{m}$ making ν^* stationary is obtained from eqn. (2.23).

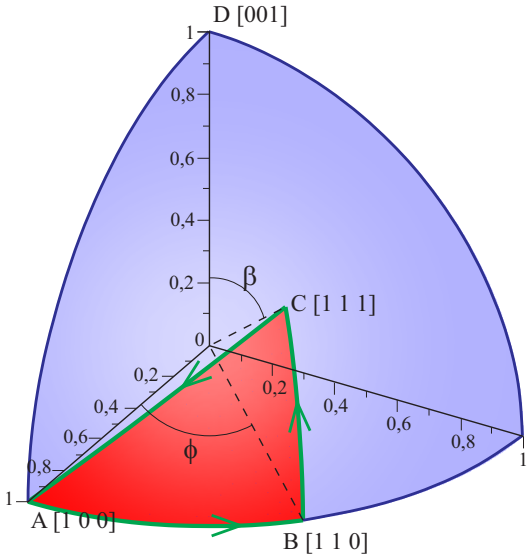

FIGURE 2.12: The irreducible spherical sector defined by the vertices corresponding to, $\mathbf{n} = 100, 110$ and 111. Note that the edge $\overline{C-D}$ is equivalent to the edge $\overline{C-A}$.

We have visualized in Fig. 2.13 all possible local minima and maxima along the path $A-B-C-A$ among which it is possible to find the global minimum and maximum.

In Fig. 2.13 we also note the high degree of anisotropy of the lattice and the fact that Poisson's ratio increases quite rapidly moving from the direction $\mathbf{n} = 100$. Also we show that in the direction $\mathbf{n} = 1p0$, with $0 \leq p \leq 1$, along $A-B$ the behaviour is always auxetic along specific transversal directions, while in the proximity of $\mathbf{n} = 111$ (point C) the behaviour is not auxetic. After to have found the global extreme values of the Poisson's ratio for a fixed value of the stiffness parameter α_1, we want now to search the global minimum and maximum as a function of α_1. To do this we follow the method proposed in [88], reaching the

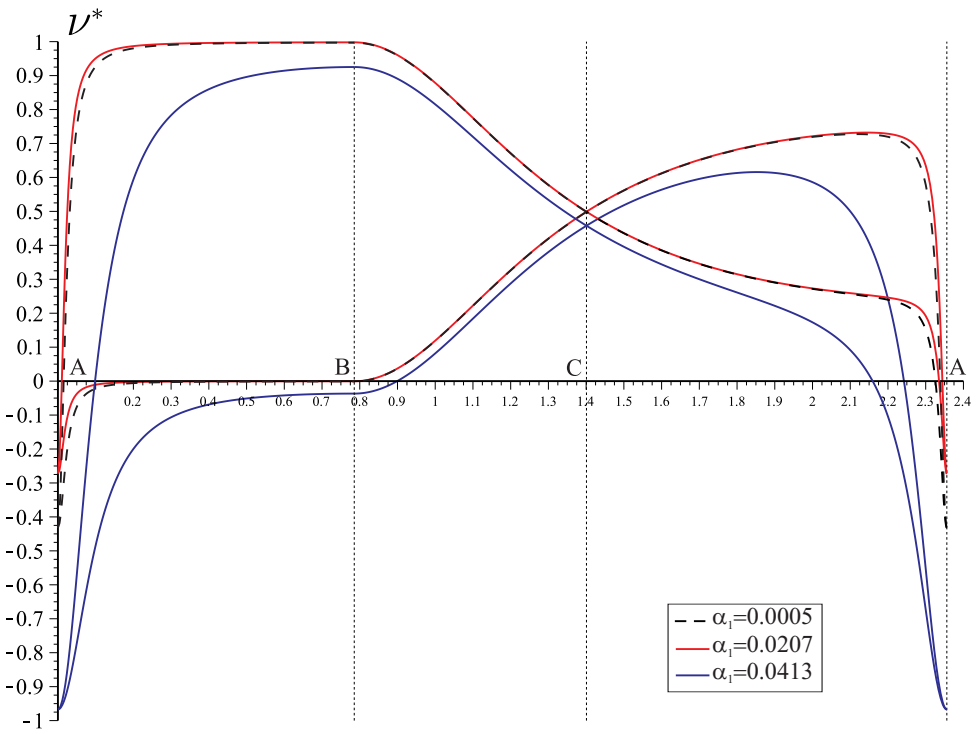

FIGURE 2.13: Maximum and minimum Poisson's ratio ν^* for different position of $\mathbf{n}$ along the path $A-B-C-A$ shown in Fig. 2.12. Results are given for three different values of the non-dimensional stiffness ratio α_1.

same results shown earlier for a single value of α_1. Along the edges of the sphere sector the potential candidates for global extremes of the Poisson's ratio are not infinite, but they are a limited number. The direction $\mathbf{n}$ can be parametrized along each edge with a single variable. Along the edge $A-B$ characterized by $\mathbf{n} = 1p0$, $0 \leq p \leq 1$ and $\mathbf{m} = p\bar{1}0$ or 001, except the specific cases $\nu^* = 0$ or $\nu^* = 1$, the stationary values of ν^* occur only at the end points $p = 0$ and 1. By convention, negative integers are written with a bar, as in $\bar{1}$ for -1. Thus, $\nu_0^* = \nu^*(100)$, $\nu_{1\bar{1}0}^* = \nu^*(110, 1\bar{1}0)$ and $\nu_{001}^* = \nu^*(110, 001)$ are potential candidates for global extrema of ν^*. Along the two edges $B-C$ and $C-D$, which is equivalent to the path $C-A$, characterized by $\mathbf{n} = 11p$, $0 \leq p \leq \infty$ and $\mathbf{m} = 1\bar{1}0$ and $\mathbf{m} = pp\bar{2}$. The four global candidates come from the roots of:

$$\nu^{*\,2} - \nu^* \nu_{111}^* - \frac{1}{48} E_{111}^* \chi, \quad \text{and} \quad (\nu^* - 1)^2 - (\nu^* - 1)(\nu_{111}^* - 1) - \frac{1}{48} E_{111}^* \chi, \tag{2.26}$$

where

$$E_{111}^* = E^*(111) = \frac{3}{s_{11} + 2s_{12} + 4s_{44}}, \quad \text{and} \quad \chi = 2s_{11} - 2s_{12} - 4s_{44}. \tag{2.27}$$

In total we have seven possible global extremes. The first three extremes are the only ones associated with the principal directions of the cube (axes and face diagonals). Moreover five of them depend on the material properties. These are $\nu^*(100)$, $\nu^*(110, 1\bar{1}0)$, $\nu^*(110, 001)$ and the following two distinct roots of eqns. (2.26) respectively,

$$\nu_1^* = \nu^*(11p_1, 1\bar{1}0) = \frac{1}{2}\nu_{111}^* - \frac{1}{2}\sqrt{\nu_{111}^{*2} + \frac{1}{6}(\nu_{111}^* + 1)(\frac{\mu_1}{\mu_2} - 1)}, \tag{2.28a}$$

$$p_1 = \sqrt{\frac{\nu_1^* + 1/2}{\nu_1^* - 1/4}}, \tag{2.28b}$$

and

$$\nu_2^* = \nu^*(11p_2, p_2p_2\bar{2}) = \frac{1}{2}(\nu_{111}^* + 1) - \frac{1}{2}\sqrt{(\nu_{111}^* - 1)^2 + \frac{1}{6}(\nu_{111}^* + 1)(\frac{\mu_1}{\mu_2} - 1)}, \tag{2.29a}$$

$$p_2 = \sqrt{\frac{\nu_2^* - 3/2}{\nu_2^* - 3/4}}, \tag{2.29b}$$

where

$$\mu_1 = \frac{1}{4s_{44}}, \quad \text{and} \quad \mu_2 = \frac{1}{2s_{11} - 2s_{12}}. \tag{2.30}$$

We have identified all seven global extreme, if now we consider the entirety of possible cubic materials with positive definite strain energy, we find that:

$$-1 < \nu_{1\bar{1}0}^* < 1, \quad \text{and} \quad -\frac{1}{2}(1 - \nu_{1\bar{1}0}^*) < \nu_{001}^* < \nu_{1\bar{1}0}^*. \tag{2.31}$$

These two relations define the interior of a triangle in the ν_{001}^*, $\nu_{1\bar{1}0}^*$ plane.

ν_{min}^*	**n**	**m**	**condition 1**	**condition 2**
$0 < \nu_{001}^*$	110	001	$\nu_{001}^* > 0$	$\nu_{1\bar{1}0}^* > \nu_{001}^*$
$-1/2 < \nu_{1\bar{1}0}^*$	110	$1\bar{1}0$	$\nu_{1\bar{1}0}^* > -1/2$	$\nu_{1\bar{1}0}^* < \nu_{001}^*$
$-1 < \nu_0^*$	110	$1\bar{1}0$	$\nu_{001}^* < 0$	$\nu_{1\bar{1}0}^* > \nu_{001}^*$
$-\infty < \nu_1^*$	110	$1\bar{1}0$	$\nu_{1\bar{1}0}^* < -1/2$	$\nu_{1\bar{1}0}^* < \nu_{001}^*$

TABLE 2.1: Global minimum of Poisson's ratio for cubic material

The interior of the triangle in the ν^*_{001}, $\nu^*_{1\bar{1}0}$ plane represents the entirety of possible cubic materials with positive definite strain energy. Tables 2.1 and 2.2 list the values of the global minimum ν^*_{min} and the global maximum ν^*_{max}, respectively, for all possible combinations of elastic parameters. Each row of the Tables 2.1 and 2.2

ν^*_{min}	**n**	**m**	**condition 1**	**condition 2**
$\nu^*_1 < -1/2$	$11p_1$	$1\bar{1}0$	$\nu^*_{1\bar{1}0} < -1/2$	$\nu^*_{1\bar{1}0} > \nu^*_{001}$
$\nu^*_0 < 0$	100	*arbitrary*	$\nu^*_{001} < 0$	$\nu^*_{1\bar{1}0} < \nu^*_{001}$
$\nu^*_{1\bar{1}0} < 1$	110	$1\bar{1}0$	$\nu^*_{1\bar{1}0} > -1/2$	$\nu^*_{1\bar{1}0} > \nu^*_{001}$
$\nu^*_{001} < 3/2$	110	001	$0 < \nu^*_{001} < 3/2$	$\nu^*_{1\bar{1}0} < \nu^*_{001}$
$-\infty < \nu^*_1$	$11p_2$	$p_2p_2\bar{2}$	$\nu^*_{001} > 3/2$	

TABLE 2.2: Global maximum of Poisson's ratio for cubic material

identifies a sector in the triangles shown in Fig. 2.14 and defined by eqn. (2.31). These sectors define the global extremes for every point within the triangles, so to identify them we need to know the two quantities ν^*_{001} and $\nu^*_{1\bar{1}0}$ from which it is possible to go back to the values sought. In Fig. 2.14 are shown with blue dots the values of ν^*_{001} and $\nu^*_{1\bar{1}0}$, for our lattice, each dot represent a different value of α_1. The minimum global Poisson's ratio, for different α_1, is always given by $\nu^*_{110} = \nu^*_0$

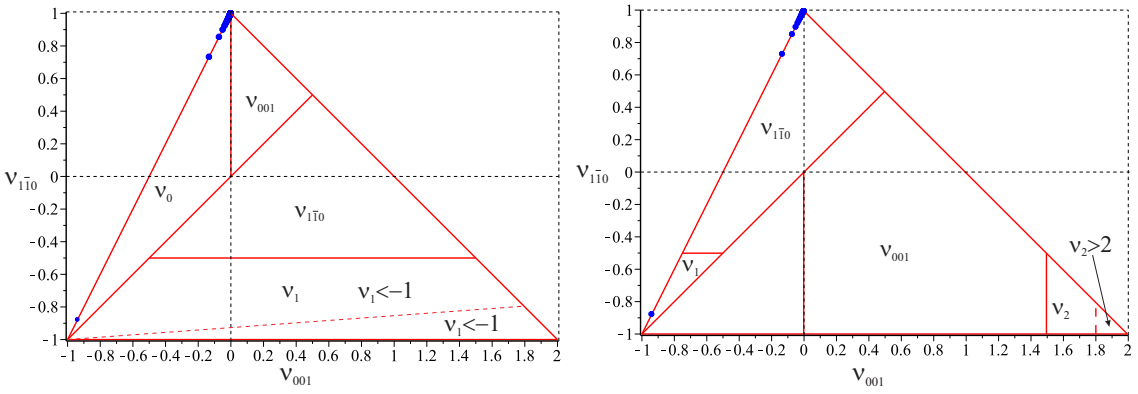

(a) (b)

FIGURE 2.14: Global maximum and minimum Poisson's ratio ν^* for a cubic material as a function of ν^*_{001} and $\nu^*_{1\bar{1}0}$. The blue dots represent the values of the cubic lattice for different values of the non-dimensional stiffness ratio α_1. (a) Global minimum Poisson's ratio. (b) Global maximum Poisson's ratio.

Finally we are able to show in Fig. 2.15 the global minimum and maximum of the Poisson's ratio of our cubic lattice as a function of the dimensionless parameter α_1. As we can see the behaviour of the lattice is always auxetic, at least along

some directions. Indeed decreasing the stiffness ratio α_1 to 0 the global minimum of ν^* tends to -1.

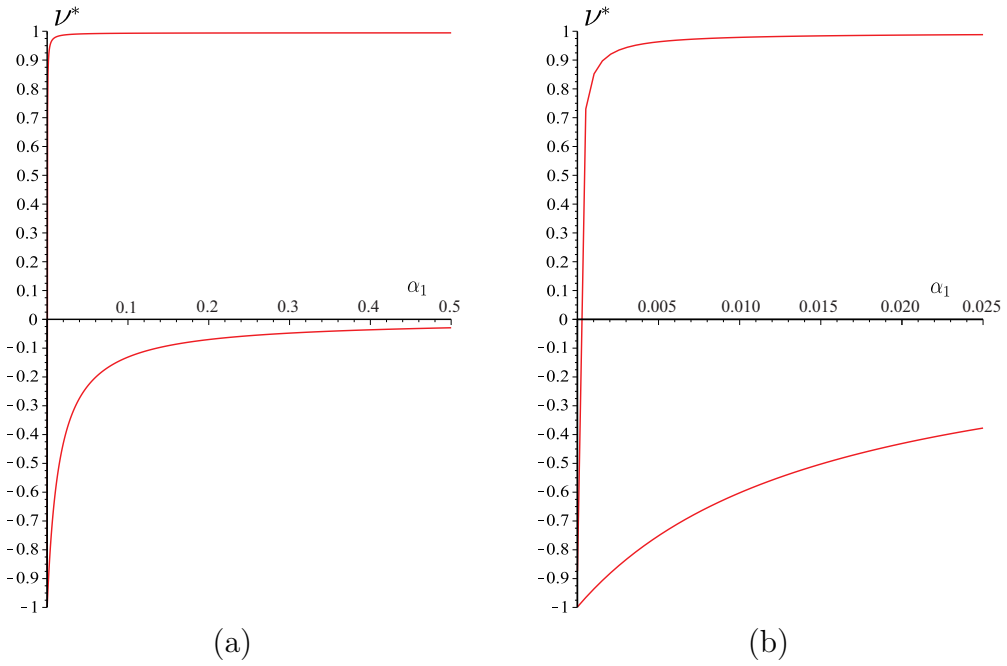

(a) (b)

FIGURE 2.15: Global maximum and minimum Poisson's ratio ν^* as a function of the dimensionless stiffness ratio α_1. a) α_1 from 0 to 0.5. b) α_1 from 0 to 0.025.

2.3 Poisson's ratio and Young's modulus for three-dimensional isotropic lattice

In the previous section we have presented an anisotropic lattice, where the Poisson's ratio is negative only with respect to some directions **n** and **m** as shown in Fig. 2.13. This directional dependence is a limitation in the performances of the structure in term of auxetic behaviour. Here we modify the previous microstructure and we show a type of three-dimensional lattice that can exhibit isotropic negative Poisson's ratio. We have introduced in the lattice described above, and shown in Fig. 2.2, diagonal beams depicted in magenta in Fig. 2.16 adding one lattice point in the center of the unit cell in addition to the eight corner points. Each diagonal beam is mutually constrained to have the same displacement at the central point where a hinge is introduced while they are constrained by internal hinges at the external end. Doing the same similarity with the crystal system used previously, it can be seen as a body-centered cubic system (cI). We call ω the ratio between the cross sectional area of the diagonal beams and the cross sectional area of the arms of the cross-shaped elements on the vertical and horizontal faces of the unit cell of the lattice. We choose to tune such coefficient to obtain an isotropic behavior. The values of the constitutive parameters will be function of the two

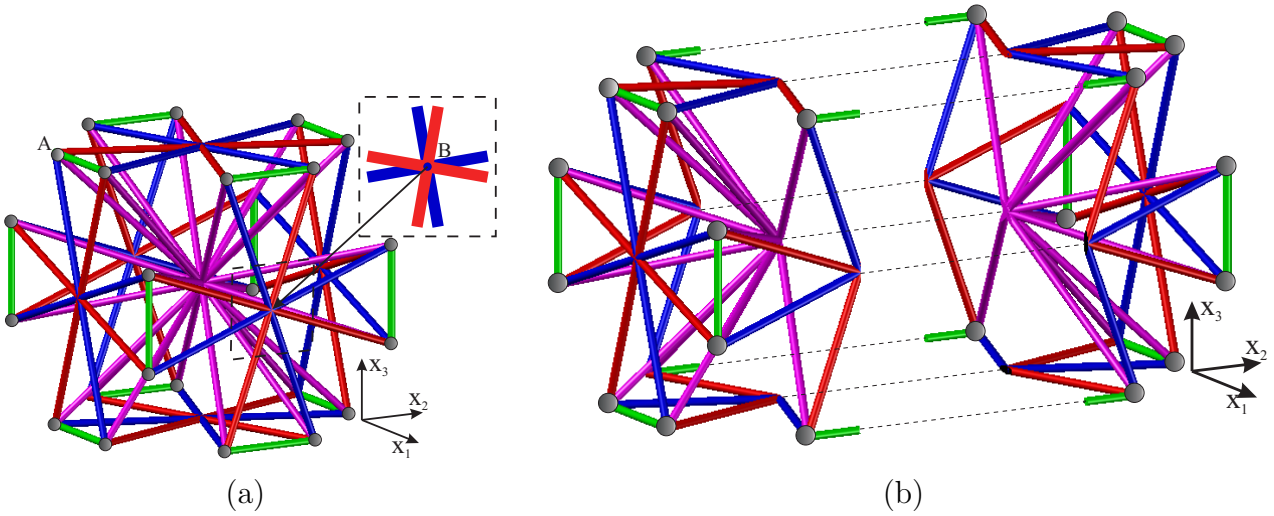

(a) (b)

FIGURE 2.16: (a)Three-dimensional unit cell of the isotropic lattice. (b)Three-dimensional unit cell of the isotropic lattice, cutted by a plane parallel to $x_1 - x_3$.

non-dimensional parameters α_1 and ω. In Fig. 2.17 we show the Young's modulus $E^*(\mathbf{n})$ and the Poisson's ratio $\nu^*(\mathbf{n}, \mathbf{m})$ in [100] as a function of the parameters ω,

for $\alpha_1 = 0.005$. As for the three-dimensional lattice described previously in Section 1.2, for small values of α_1 the mechanical behaviour of the lattice is auxetic at least in the considered directions.

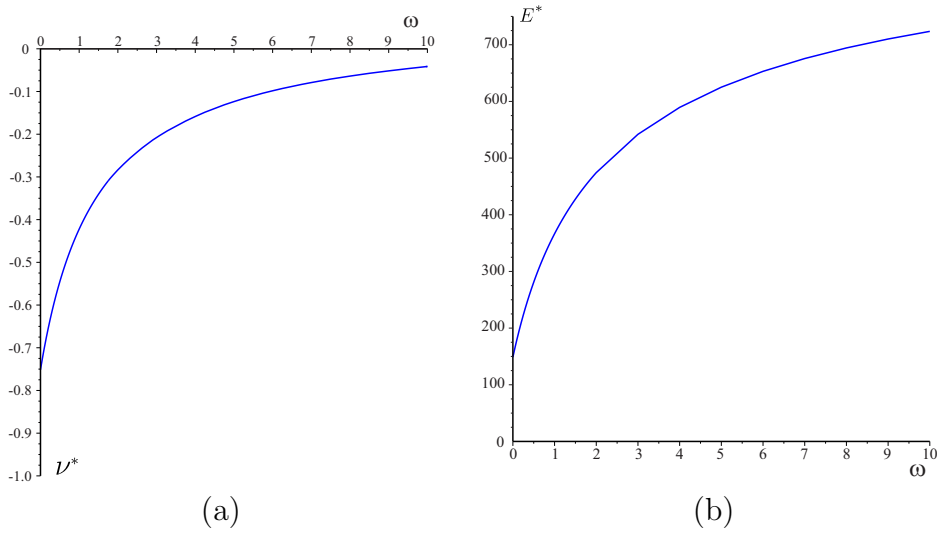

FIGURE 2.17: (a) Poisson's ratio ν^* as a function of non-dimensional stiffness ratio ω, for $\alpha_1 = 0.005$. (b) Young's modulus E^* as a function of non-dimensional stiffness ratio ω for $\alpha_1 = 0.005$. Values are given for $\mathbf{n} = 100$.

In Fig. 2.18 the Young's modulus, as a function of ω, is shown for three representative points [100], [110] and [111]. Result are given for $\alpha_1 = 0.005$. It can be seen that changing the value of the cross-sectional ratio ω the maximum value of $E^*(\mathbf{n})$ change position from 100 to 111. The intersection point corresponds to the value of ω for which the behaviour of the lattice becomes isotropic.

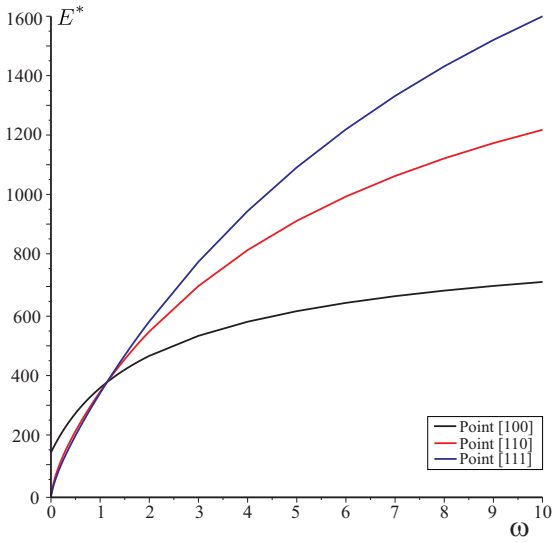

FIGURE 2.18: Young's modulus E^* as a function of ω, for $\alpha_1 = 0.005$, evaluated for directions $\mathbf{n} = 100$, 110 and 111.

To highlight the influence of the ratio ω on the behaviour of the lattice, in Fig. 2.19 it is depicted the Young's modulus $E^*(\mathbf{n})$ for each direction $\mathbf{n}$ and $\alpha = 0.005$. The behaviour of the lattice is generally cubic as ω changes, but it became isotropic when the plot assumes spherical shape at $\omega \sim 1.13695$, see Fig. 2.19(c). This value is also the transition point to 'shear dominant' structures.

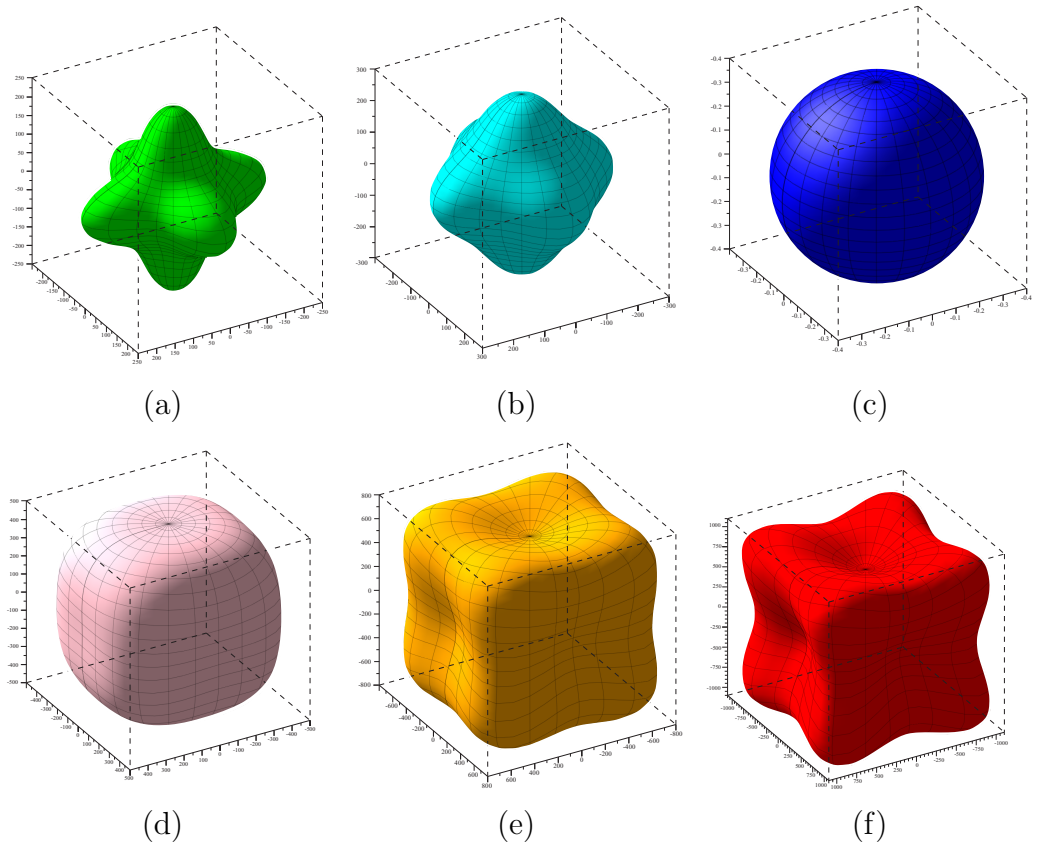

FIGURE 2.19: Directional dependence of the homogenized Young's modulus E^* for six different cross-shaped ratio ω and for $\alpha_1 = 0.005$. (a) $\omega = 0.25$. (b) $\omega = 0.5$. (c) $\omega = 1.13695$. (d) $\omega = 2$. (e) $\omega = 5$. (f) $\omega = 10$.

The directional dependence of the Young's modulus in the $x_1 - x_2$ plane is illustrated in the polar plot in Fig. 2.20 as a function of the direction of $\mathbf{n}$ for the six different values of $\omega = 0.25, 0.5, 1.13695, 2, 5, 10$, when ω is close to 1.3695 the behaviour is isotropic. To identify the value of ω for which the behaviour of the lattice becomes isotropic we compared the shear modulus μ^* (red line) as a function of ω in 100, and the shear modulus $\mu^*_{iso} = E^*/(2(1+\nu^*))$ (blue line) that the lattice would have in case of isotropic behavior, a representation is shown in Fig. 2.21. The intersection point identifies the value of $\omega = 1.13695$ for which the lattice has the desired isotropic behavior. If we consider now a three-dimensional plot of the Poisson's ratio for $\omega = 1.13695$ and $\alpha_1 = 0.005$, it will assume a spherical

shape, see Fig. 2.22, the behaviour for this particular value of α_1 is auxetic and the value of $\nu^* = -0.35$. We have described the behaviour of $E^*(\mathbf{n})$ and $\nu^*(\mathbf{n}, \mathbf{m})$ for

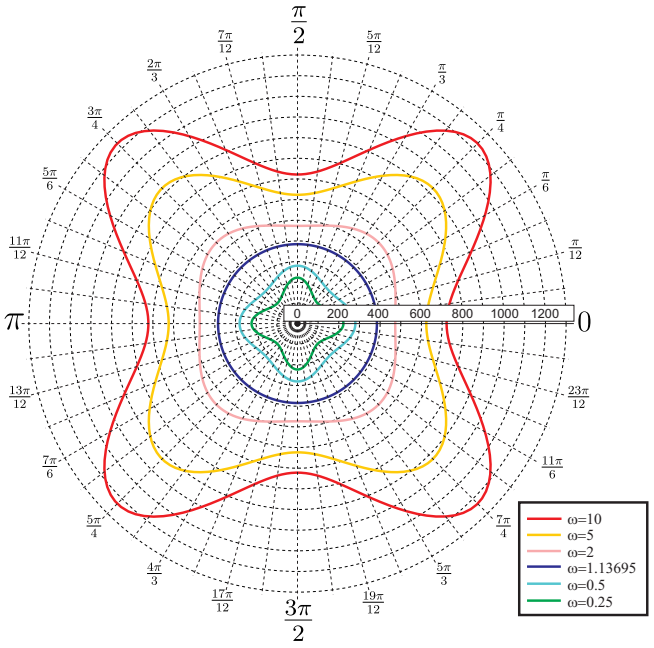

FIGURE 2.20: Polar graph of the Young's modulus E^* for six different values of non-dimensional stiffness ratio ω and for $\alpha_1 = 0.005$.

a fixed value of the stiffness ratio α_1 and we have found how is possible to achieve an isotropic behaviour changing the ratio of cross-sectional area of the crossbeams to cross-sectional area of the diagonal beams through the parameter ω.

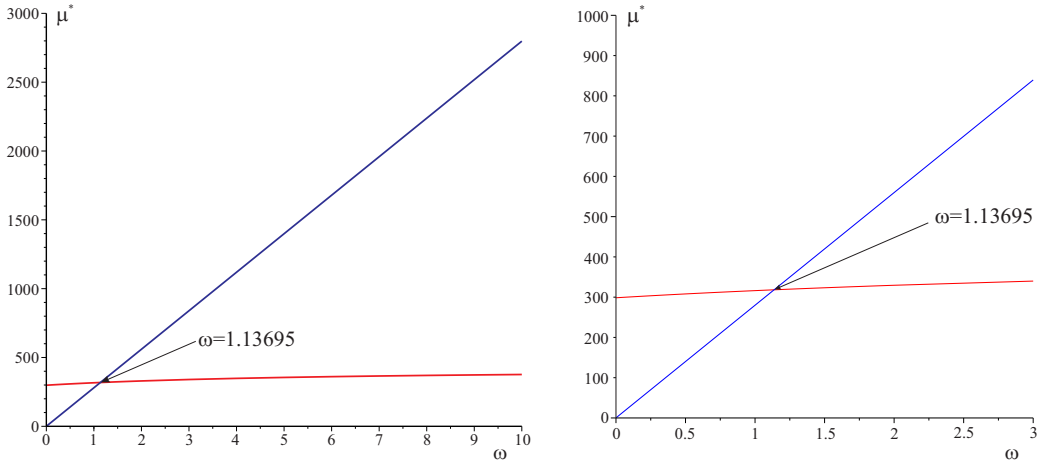

FIGURE 2.21: In red shear modulus μ^* as a function of non-dimensional stiffness ratio ω, in blue shear modulus in case of isotropic behaviour, for $\alpha_1 = 0.005$. The intersection point represents the value of the shear modulus for which the lattice assumes isotropic behavior. a) For ω from 0 to 10. a) For ω from 0 to 3.

It is now interesting to illustrate the behaviour of the lattice when it is guaranteed isotropy.

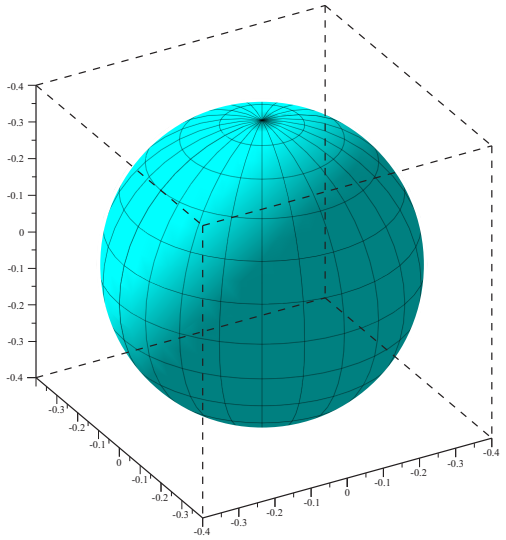

FIGURE 2.22: Three-dimensional representation of the Poisson's ratio ν^*, in case of isotropic behaviour, for $\omega = 1.13695$ and $\alpha_1 = 0.005$.

We have determined for each stiffness ratio α_1 the value of ω that ensures isotropic behaviour.

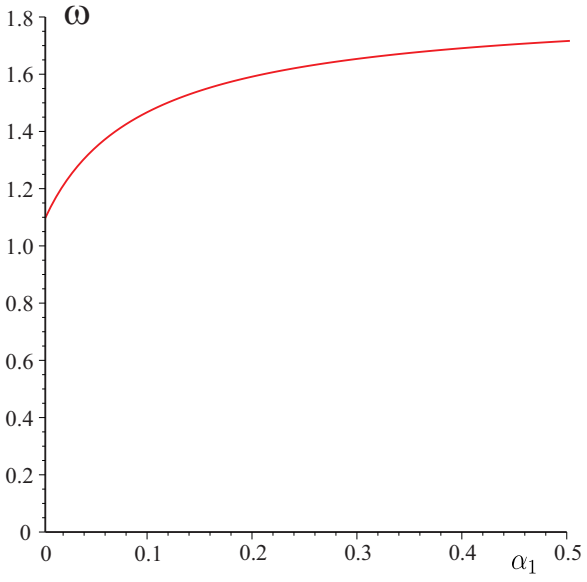

FIGURE 2.23: Non-dimensional cross-sectional ratio ω as a function of non-dimensional stiffness ratio α_1, in case of isotropic behaviour.

These values of ω are shown in Fig. 2.23. As a further confirmation of the isotropic behaviour we also represent in Fig. 2.24 the Zener anisotropic factor β_{cub} as a function of α_1, obtained considering the values of ω in Fig. 2.23. It is evident that

$\beta_{cub} = 1$, confirming the isotropic behaviour. We conclude the section describing the value of the isotropic Poisson's ratio as α_1 changes, the auxetic behaviour is reached for $\alpha_1 < 0.06$.

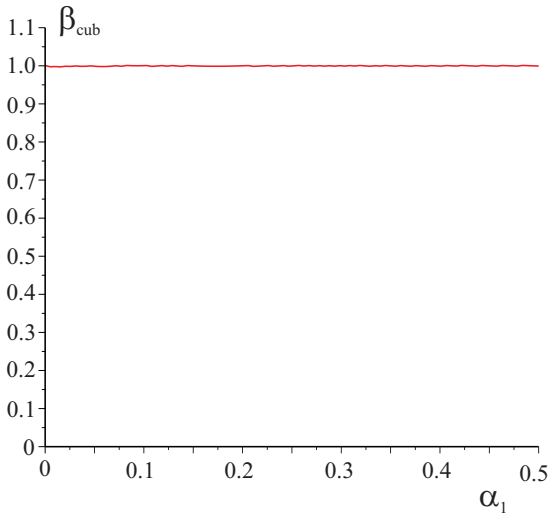

FIGURE 2.24: Zener anisotropic factor β_{cub} for the isotropic lattice as a function of the non-dimensional stiffness ratio α_1.

The minimum isotropic Poisson's ratio is $\nu^* = -0.57$, whereas the maximum one is $\nu^* = 0.15$, as shown in Fig. 2.25.

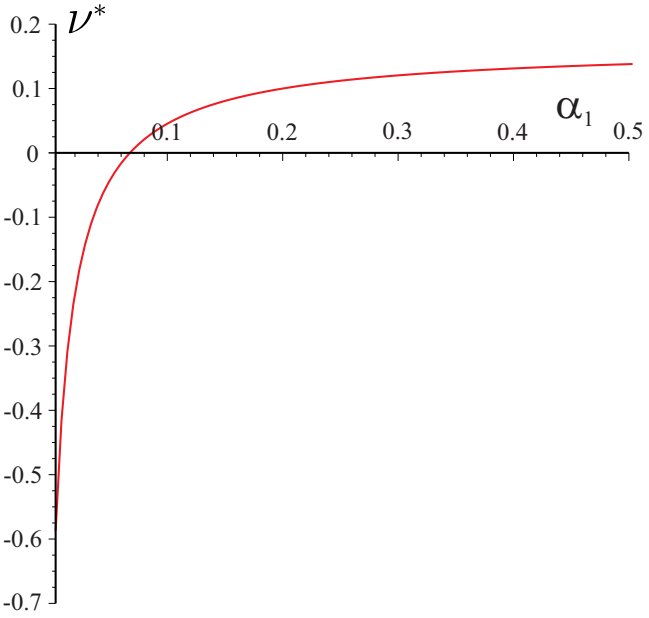

FIGURE 2.25: Poisson's ratio ν^* as a function of α_1, in case of isotropic behaviour.

In Fig. 2.26 we show the Young's modulus E^*, the bulk modulus K^* and the

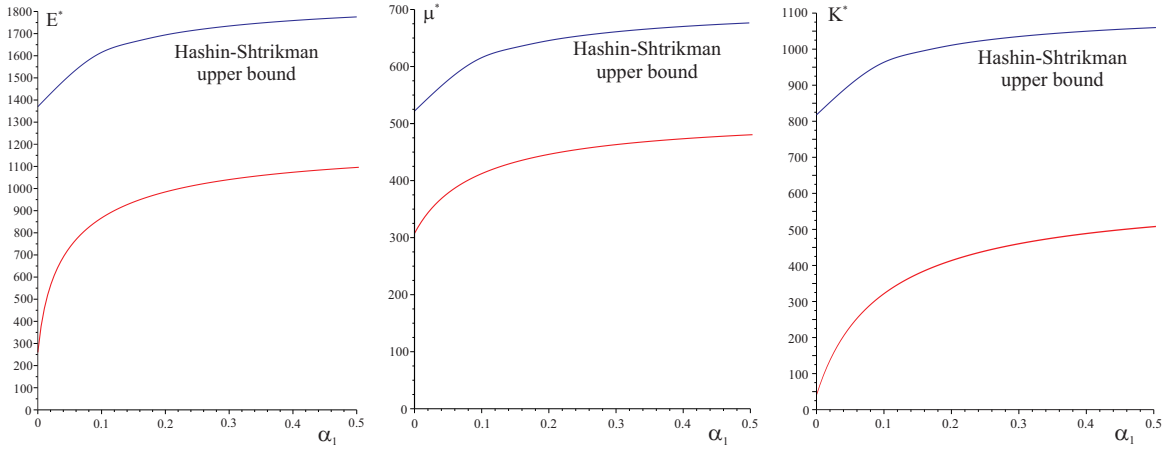

(a) (b) (c)

FIGURE 2.26: Young's modulus E^*, Bulk modulus K^* and shear modulus μ^* as a function of α_1, in case of isotropic behaviour. (a) Young's modulus. (b) Shear modulus. (c) Bulk modulus

Shear modulus μ^* as a function of α_1, in blue line are depicted the HashinShtrikman upper-bounds of low-density isotropic materials with one single elastic phase, supplied in Table 2.3. The bounds are normalized by the Young's modulus of

Young's modulus E^*/E	**Shear modulus** μ^*/E	**Bulk modulus** K^*/E
$\frac{\rho}{6}(1+3\frac{49K+8\mu}{6K+8\mu})$	$\frac{\rho}{15}(1+\frac{18K^2+8\mu^2+21K\mu}{3K(3K+4\mu)})$	$\frac{\rho}{9}(1+\frac{9K}{3K+4\mu})$

TABLE 2.3: HashinShtrikman upper-bounds of low-density isotropic materials with elastic Young's modulus E, shear modulus μ and bulk modulus K. The bounds for the effective Young's modulus E^*, shear modulus μ^* and bulk modulus K^*, are normalized by E.

the constituent material E, they depends on the bulk modulus K, on the shear

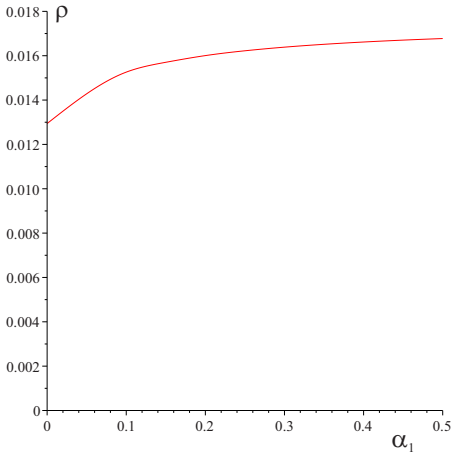

FIGURE 2.27: Density ρ of the isotropic lattice as a function of α_1.

modulus μ of the constituent materials, and on the relative density ρ, defined as the volume of beams per unit volume of the lattice, [89]. The dependence of the HashinShtrikman upper-bounds on the ratio α_1 is obtained from the relation between α_1 and ρ reported in Fig. 2.27. The values of the elastic moduli are those typical of the iron: $E = 200000\, N/mm^2$, $K = 170000\, N/mm^2$ and $\mu = 80000\, N/mm^2$.

Chapter 3

Lattices with Negative Coefficient of Thermal Expansion

3.1 Introduction

The coefficient of thermal expansion is the measure of the deformation of the material due to a unitary change of temperature. Materials normally expand on heating and contract when cooled (positive thermal expansion coefficients), however not all systems behave in this way, in fact there are systems (materials or structures) which have the counterintuitive property of contracting upon heating (negative thermal expansion). It should also be noted that for anisotropic systems the coefficient of thermal expansion is not anymore a scalar quantity, but it is a second order tensor and it is possible that a system exhibits negative thermal expansion in some directions. In homogeneous crystalline materials thermal expansion is attributed to slight nonlinearity (an-harmonicity) of the interatomic potential, it has been therefore considered to be a property intrinsic to each material. The ability to generate materials with negative coefficient of thermal expansion, or adaptable to a desired value, can be achieved either by creating a homogeneous material with that particular property or by a special micro-structures. The first solution is rarely possible, is limited to a single coefficient of thermal expansion value and leads to expensive materials, the second one uses lattice structures made of common materials to achieve properties un-achievable by their solid counterparts. Only very few known solids possess a negative coefficient of thermal expansion,

cubic zirconium tungstate ($\alpha - ZrW_2O_8$) is perhaps one of the most studied materials to have this unusual phenomenon, indeed it contracts continuously and isotropically over a wide range of T [90, 91]. Besides ZrW_2O_8 also ZrP_2O_7 and $Sc_2(WO_4)_3$ families have aroused considerable interest over the past few years for the magnitude and temperature range over which they display negative thermal expansion [92]. Other examples include glasses in the titania-silica family [93] at room temperature T and silicon and germanium [94] at very low T ($< 100^oK$). Materials with directional negative expansion coefficients at room temperature include Kevlar®, carbon fibers, plastically deformed (anisotropic) Invar (FeNi alloys) [95], and certain molecular networks. Some new materials are emerging which can accomplish negative expansion, e.g., many liquid crystal organic fibers as well as carbon and aramid fibers can show negative values in a particular direction.

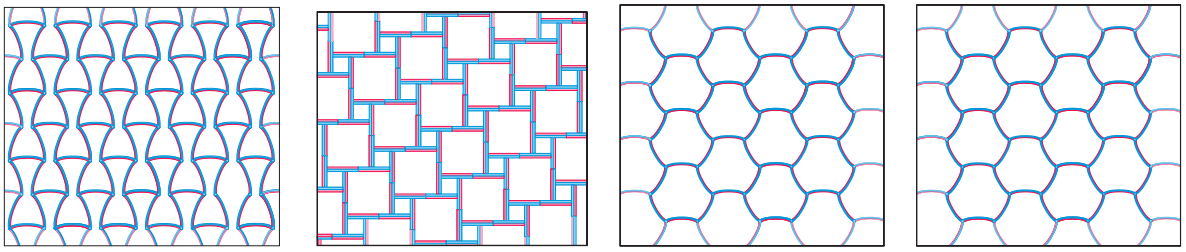

(a) (b) (c) (d)

FIGURE 3.1: Lattice with negative thermal expansion, made by two dissimilar materials of different thermal expansion coefficients which bends in response to a temperature change, by Lakes et al. [96, 97].

There have been a small number of attempts to rationally design specific structures with negative thermal expansion, the unifying principle is that the negative thermal expansion mechanism is driven by a heterogeneity in the coefficient of thermal expansion of the constituent parts.

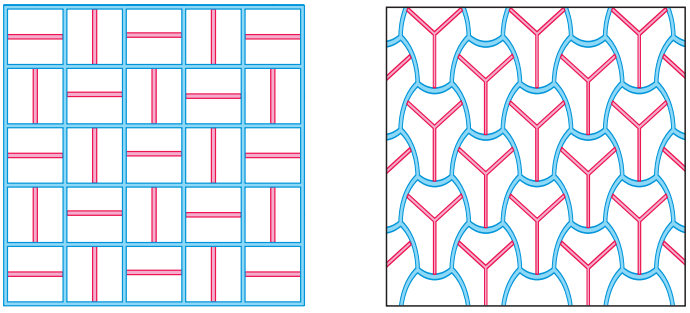

(a) (b)

FIGURE 3.2: Micro-structures that combine materials with different thermal expansion to achieve an overall effective negative expansion, by Jefferson et al. [98].

Of particular interest are the materials and structures that not only exhibit negative thermal expansion behavior, but also allow to adjust the coefficient of thermal expansion.

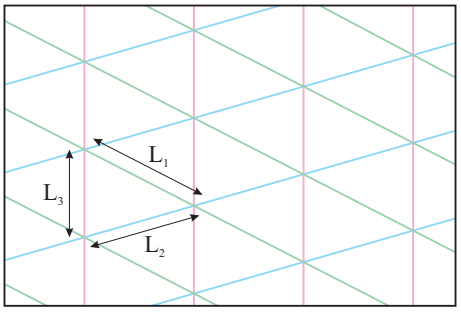

FIGURE 3.3: Periodic triangular lattice with one side made from a different material than the other two ones, able to produce adjustable thermal expansion in two dimensions, by Grima et al. [99].

Properly designed structures can produce thermal expansion coefficients lying well outside the range shown by homogeneous materials, both in a single direction and in a plane, indeed much lower negative values may be achieved compared with those of the constituent materials as well as larger positive values. Accordingly it is possible to generate structures with very low or negative thermal expansion from conventional materials.

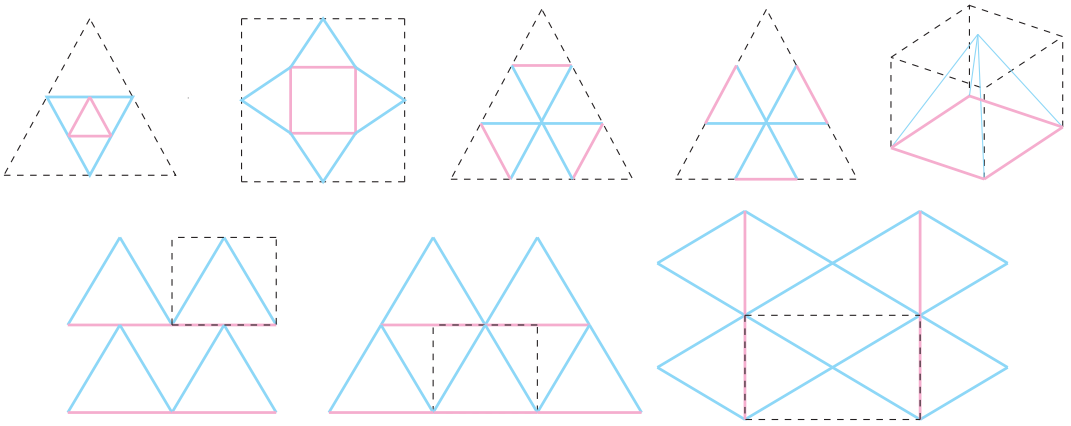

FIGURE 3.4: Elements made with different materials that produce tunable thermal expansion in two-dimension and in three dimensions, by Miller et al. [100].

We remember the lattices proposed by Lakes et al. [96, 97], shown in Fig. 3.1, where the single rib elements contain two dissimilar materials with different thermal expansion coefficients which bends in response to a temperature change, leading to a particular effective thermal expansion. In [98] is shown a micro-structure that combines materials with different coefficient of thermal expansion to achieve

an overall effective isotropic expansion, substantially different from that of the constituent materials, see Fig. 3.2. Models, that involve periodic networks which consist of triangular elements with one side made from a different material from the other two ones, are known to produce tunable thermal expansion in two dimensions [99, 100], see Figs.3.3 and 3.4, and in three dimensions [100, 101], see Fig. 3.4. In [102] is analyzed a periodic triangular lattice, see Fig. 3.5, that simultaneously combine negative Poisson's ratios and negative thermal expansion.

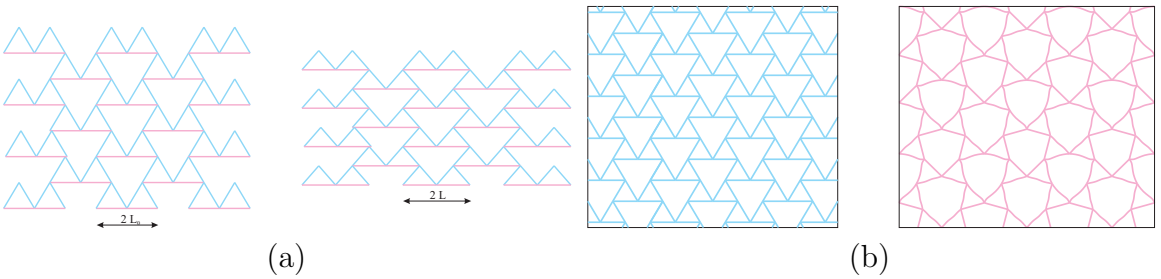

FIGURE 3.5: Periodic triangular lattice that simultaneously combine negative Poisson's ratios and negative thermal expansion, by Grima et al. [102].

Using materials with different thermal expansion and exploiting thermal stress produced by Poisson's contraction for an increase in temperature, it is possible to compensate thermal expansion in some direction by careful choose of the material properties. This is what happens to multilayered composites [103], see Fig. 3.6(a), to composites with needle-like inclusions [104], see Fig. 3.6(b), and to lattice structures with concentric tubes [105], where due to the Poisson's effect we have tunable coefficient of thermal expansion, see Fig. 3.6(c).

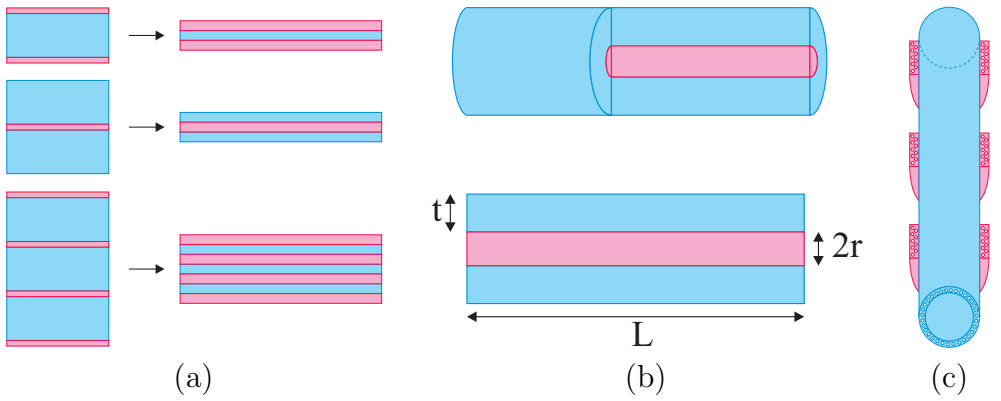

FIGURE 3.6: a) Multilayered composites with adjustable thermal expansion, by Grima et al. [103]. b) Composites with needle-like inclusions with negative thermal expansion, by Grima et al. [104]. c) Lattice structures with concentric tubes where due to the Poisson's effect we have tunable coefficient of thermal expansion , by Lehman and Lakes [106].

The capability to design micro-structured media with desired thermal expansion has great practical importance and it has been studied for many years since to neglect temperature effects may lead to disastrous consequences. Materials exhibiting the capacity to be precisely tailored to a specific positive, negative or even zero coefficient of thermal expansion are very useful in various practical applications. In many engineering circumstances uncontrolled thermal expansion is usually a nuisance because it precludes extreme precision, therefore a zero expansion material can be employed in the manufacture of precision instruments. Materials with low or zero coefficients of thermal expansion are desirable for applications that involve large temperature variations to reduce thermal stresses and to have structures that are dimensionally stable as temperature varies, in the field of structural engineering we can mention bridges, aircraft, space structures, piping systems, industrial machineries and energy plants. Lattice structures are widely used for example in satellites, for support of appendages such as antennae and telescopes, indeed such equipments are thermal sensitive so it is required to have dimensional stability over a large temperature changes in addition to ensuring adequate strength [107], see Fig. 3.7.

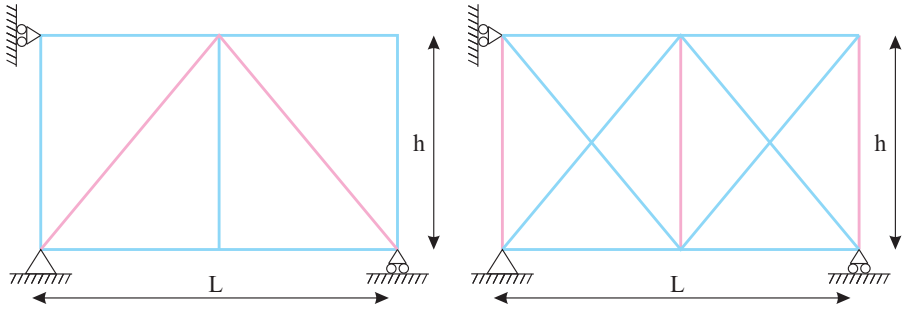

FIGURE 3.7: Frame structures with zero thermal expansion, by Palumbo et al. [107].

Materials produced to have low expansion are used to mitigate the effects of thermal shock, Pyrex© glass, a low expansion ceramic, is the best known examples of this application. Negative thermal expansion materials can be extremely useful in the manufacture of composites exhibiting some pre-determined thermal expansion coefficients, since the presence of a component with negative thermal expansion lowers the overall thermal expansion of a composite. A fastener made of a negative thermal expansion material, upon heating, can be inserted easily into a hole. Upon cooling it will expand, fitting tightly into the hole. By contrast, materials with extremely large expansion can be employed as 'thermal' actuators. Lastly

materials with a coefficient of thermal expansion matched to that of another material are also of importance in electronic and biomedical applications, for instance dental fillings need to have their expansion coefficients matched to those of teeth [108].

In this chapter we describes three planar periodic lattices, similar to the ones in Chapter 1 and a three-dimensional periodic lattices, such as the one in Chapter 2, with desired thermal expansion coefficient (positive, negative or near zero). They are made of two materials with intrinsically positive thermal expansion coefficients. The particular geometry of the micro-structures makes possible to have dissimilar expansions of the elements within the lattice, leading to the effective coefficient of thermal expansion different from that of the constituent elements. We tested experimentally the effective coefficient of thermal expansion of the hexagonal micro-structured medium. A theoretical expression of the above mentioned macroscopic property has been provided in full analytical form as a function of the coefficients of thermal expansion of the constituent elements and of the geometrical configuration of the lattices. The studied micro-structures expand by the same extent in any direction upon heating showing an isotropic expansion. It is important to emphasize that although there are several models with either negative Poisson's ratio or negative thermal expansion, it is not possible to say the same for systems which exhibit both of these anomalous properties simultaneously. Indeed it is known that negative thermal expansion and negative Poisson's ratio are not mutually exclusive properties, as shown in [96, 102, 109, 110, 111]. The novel systems are constructible at any length-scale including the micro-scale from conventional components with different mechanical and thermal properties, which may be combined to ensure the required macroscopic behaviour. In Section 3.2 we determine analytically the macroscopic coefficient of thermal expansion of the lattices and we present the results applied to conventional materials. In Section 3.3 we show experimental evidence that the hexagonal lattice can have negative thermal expansion.

3.2 Model of periodic lattices with tunable coefficient of thermal expansion

In this section we derive the effective coefficient of thermal expansion of the three types of lattices presented in Chapter 1. The micro-structures are composed of cross-shaped elements, depicted in red and blue in Fig. 3.8, with coefficient of thermal expansion λ_c, and of extensional elastic springs or trusses with coefficient of thermal expansion λ_t, depicted in green.

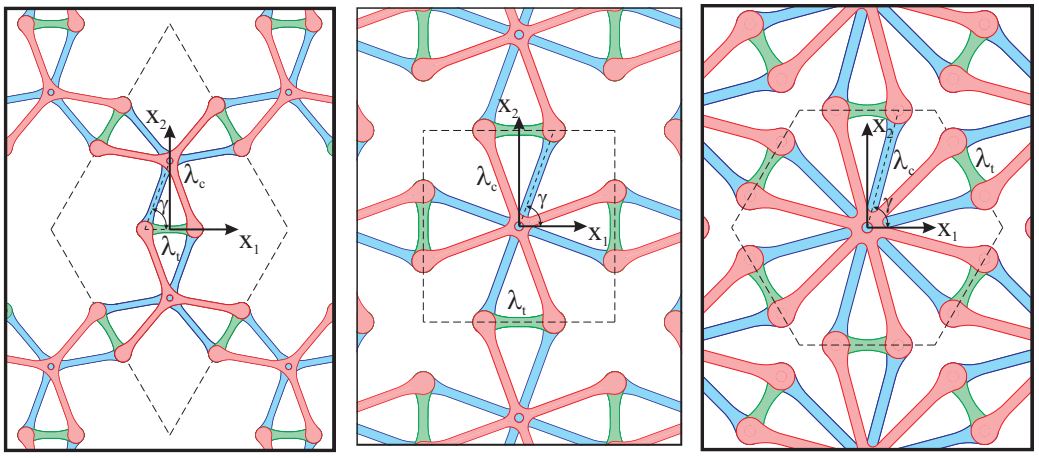

(a) (b) (c)

FIGURE 3.8: Elementary cells of the lattices. The coefficients of thermal expansion of the crosses and of the longitudinal elements are λ_c and λ_t respectively. a) Hexagonal lattice. b) Square lattice. c) Triangular lattice. The arms of the crosses, with coefficient of thermal expansion λ_c, are shown in red and blue, whereas the spring or truss, with coefficient of thermal expansion λ_t, are shown in green.

The linearised behaviour of each lattice depends nonlinearly on the reference configuration determined by the angle γ formed by the arms of the crosses and the springs. The lattices have thermal isotropic behaviour in plane; to quantify the linearized thermal expansion we could indifferently use the volume (λ_V), area (λ_A) or linear (λ_L) thermal expansion coefficient, since they are related by known relations $\lambda_L = 1/2 = \lambda_A = 1/3 = \lambda_V$, clearly for the in plane structures we will focus only on (λ_L) and (λ_A). In Fig. 3.9 we show the three typologies of lattice in two different configurations, where $\lambda_c \ll \lambda_t$. In the right column the lattices are subjected to an increase of temperature ΔT which causes a contraction of the lattices, as shown by the dashed rectangles which indicate the macroscopic thermal deformation.

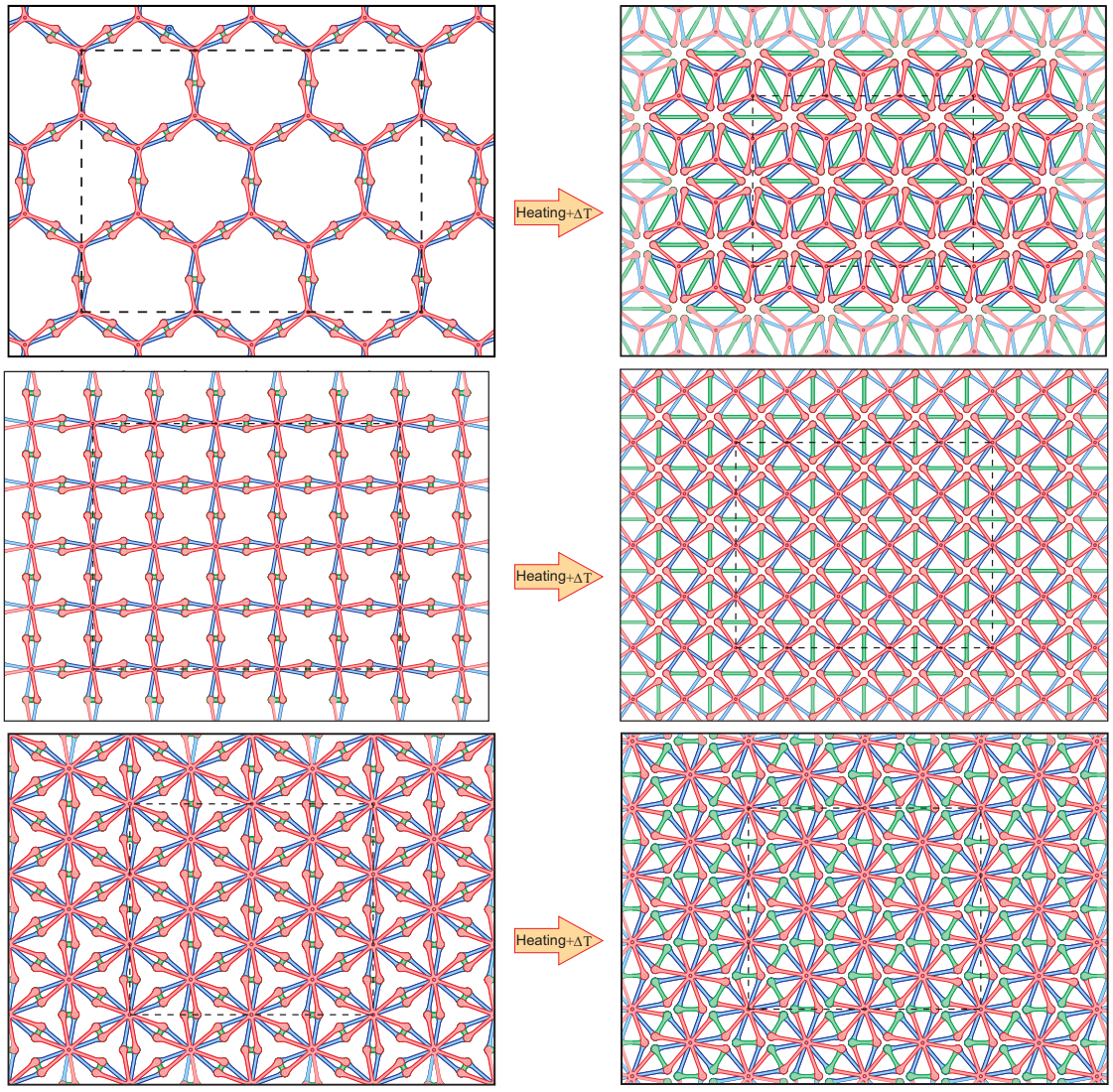

FIGURE 3.9: Two different configurations of the lattice as a result a increase of temperature ΔT, $\lambda_c \ll \lambda_t$.

The analytical expression of the effective coefficient of thermal expansion is determined as follows. We draw from the lattices the triangle shown in Fig. 3.10. The point 3 represents the intersection of the crosses visualized in blue and red in Fig. 3.8 and Fig. 3.9, whereas the element joining the points 1 and 2 is longitudinal spring visualized in green. The vertical displacement of the point 3 identifies the effective thermal deformation; its displacement for a change of temperature ΔT is due to the thermal deformation of the cross-shaped and longitudinal elements. Therefore, it can be computed as the sum of two contributions, the displacement when $\lambda_c \neq 0$ and $\lambda_t = 0$ plus the displacement when $\lambda_c = 0$ and $\lambda_t \neq 0$, as shown

in Fig. 3.10:

$$L_1 - L_0 = \frac{p\lambda_c \Delta T}{\sin\gamma} - \frac{p\lambda_t \cos^2\gamma \Delta T}{\sin\gamma}. \tag{3.1}$$

Therefore the linear coefficient of thermal expansion is

$$\lambda_L = \frac{L_1 - L_0}{L_0 \Delta T} = \frac{\lambda_c}{\sin^2\gamma} - \frac{\cos^2\gamma \lambda_t}{\sin^2\gamma} \tag{3.2}$$

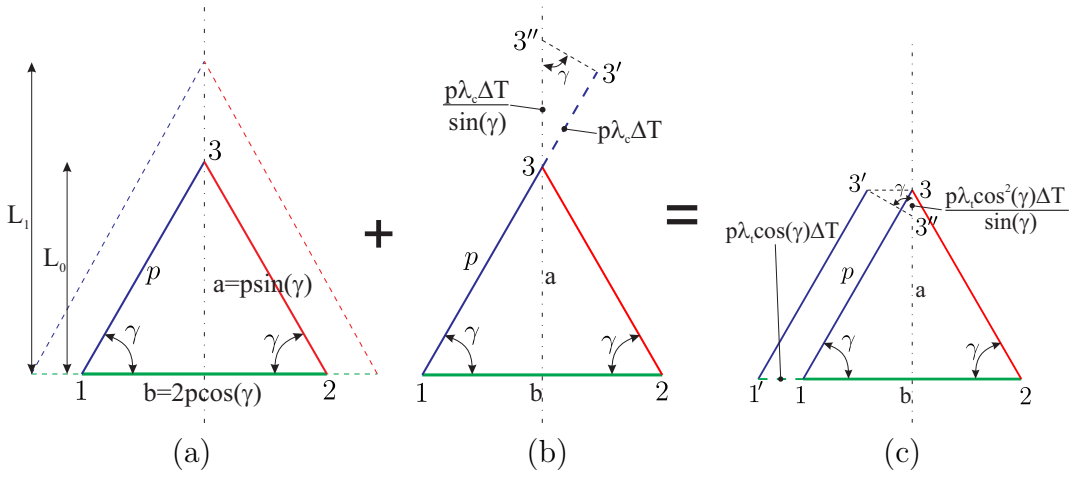

FIGURE 3.10: Computation of the linear coefficient of thermal expansion. The height variation $L_1 - L_0$ of the triangle 123 due to a temperature change ΔT (a) is the sum of the displacement of the point 3 when $\lambda_c \neq 0$ and $\lambda_t = 0$ (b) and the displacement of the point 3 when $\lambda_c = 0$ and $\lambda_t \neq 0$ (c)5.

The thermal expansion of the triangle in Fig. 3.10 can also be derived, as in [100]

$$(a + \delta a)^2 = (p + \delta p)^2 - (\frac{b + \delta b}{2})^2, \tag{3.3}$$

where

$$\delta p = p\lambda_c \Delta T, \quad \delta b = 2p\cos\gamma\lambda_t \Delta T \quad \text{and} \quad a = p\sin\gamma,$$

which leads to

$$2p\,\sin\gamma\delta a + \delta a^2 = 2p^2\lambda_c\Delta T + p^2\lambda_c^2\Delta T^2 - 2p^2\cos^2\gamma\lambda_t\Delta T - p^2\lambda_t^2\Delta T^2. \tag{3.4}$$

Considering small elongation $\lambda_c \Delta T$, $\lambda_t \Delta T \ll 1$, we can simplify the above relation and we get to linear order

$$\delta a = \frac{p\lambda_c\Delta T - p\cos^2\gamma\lambda_t\Delta T}{\sin\gamma}. \tag{3.5}$$

The area coefficient of thermal expansion λ_A is obtained from the deformation of the initial area of the elementary cell A_0, shown in dashed line in Fig. 3.8. Indicating with A_1 the area of the cell after the thermal deformation due to a change of temperature ΔT, the real deformation of the lattices is

$$\lambda_A \Delta T = \frac{A_1 - A_0}{A_0} = \frac{2\Delta T}{\sin^2\gamma}(\lambda_c - \lambda_t \cos^2\gamma) + \frac{\Delta T^2}{\sin^4\gamma}(\lambda_c^2 - 2\lambda_c\lambda_t \cos^2\gamma + \lambda_t^2 \cos^4\gamma) \tag{3.6}$$

To leading order in the small parameters $\lambda_c \Delta T$, $\lambda_t \Delta T$ eqn. (3.6) gives the expected

$$\lambda_A = 2\lambda_L = \frac{2\lambda_c}{\sin^2\gamma} - \frac{2\cos^2\gamma\lambda_t}{\sin^2\gamma} \tag{3.7}$$

We introduce now the ratio η of the coefficient of thermal expansion of the cross-shaped elements λ_c to the coefficient of thermal expansion of the longitudinal elements λ_t, namely $\eta = \lambda_c/\lambda_t$.

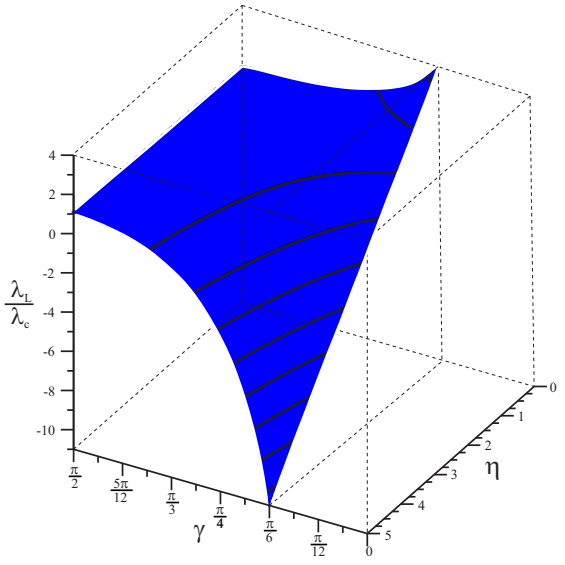

FIGURE 3.11: Effective coefficient of thermal expansion of the lattices as a function of the angle γ and of the ratio $\eta = \lambda_t/\lambda_c$.

The plot in Fig. 3.11 describes the effective linear coefficient of thermal expansion λ_L of eqn. (3.2), non-dimensionalized with respect to λ_c, as a function of the parameter η and of the angle γ that determines the reference configuration of the lattices. We note the possibility to have a negative coefficient in a wide interval of ratios η and configurations γ, in particular the coefficient of thermal expansion equal to zero $\lambda_L = 0$ when $\lambda_t = \lambda_c/\cos^2\gamma$.

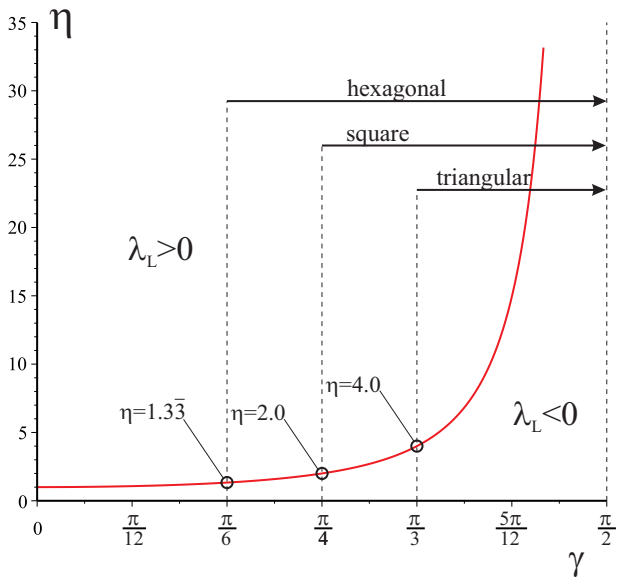

FIGURE 3.12: Ratio between coefficient of thermal expansion η as a function of γ, for which the effective coefficient of thermal expansion of the lattices is zero.

In Fig. 3.12 we show the ratio $\eta = \lambda_t/\lambda_c$ as a function of the angle γ that identifies the geometrical configuration of the lattices when the effective coefficient of thermal expansion of the lattices is zero such a line is the threshold between positive and negative domains of λ_L.

Material	λ_L at 20^oC $(10^{-6}K^{-1})$	λ_V at 20^oC $(10^{-6}K^{-1})$
Aluminium	23.1	69
Carbon steel	10.8	32.4
Concrete	12	36
Copper	17	51
Diamond	1	3
Glass	8.5	25.5
Gold	14	42
Invar	1.2	3.6
Iron	11.8	33.3
Lead	29	87
Nickel	13	39
Platinum	9	27
PVC	52	156
Quartz	0.33	1
Silicon	2.56	9
Sitall	0 ± 0.15	0 ± 0.45
Silver	18	54
Stainless steel	$10.1 \sim 17.3$	51.9
Steel	$11.0 \sim 13.0$	$33.0 \sim 39.0$
Titanium	8.6	1114
YbGaGe	0	0
Zerodur	≈ 0.02	

TABLE 3.1: Coefficients of thermal expansion of common materials

If we consider that geometrically the minimum attainable values of γ are $\pi/6$, $\pi/4$ and $\pi/3$, for hexagonal, square and triangular lattice respectively, the minimum values of η are $1.3\bar{3}$, 2 and 4. Such ratio indicate that the two materials composing the micro-structure can have coefficients of thermal expansion which differ of less than one order of magnitude, in order to assure $\lambda_L < 0$, values perfectly attainable by common materials. In particular hexagonal auxetic lattice allows the use of materials with the smaller ratio η. Increasing the angle γ, to obtain an effective negative coefficient of thermal expansion, we need to use two materials where the difference between the coefficients of thermal expansion λ_c and λ_t is significant, greater than 10 for $\gamma > 0.4\pi$.

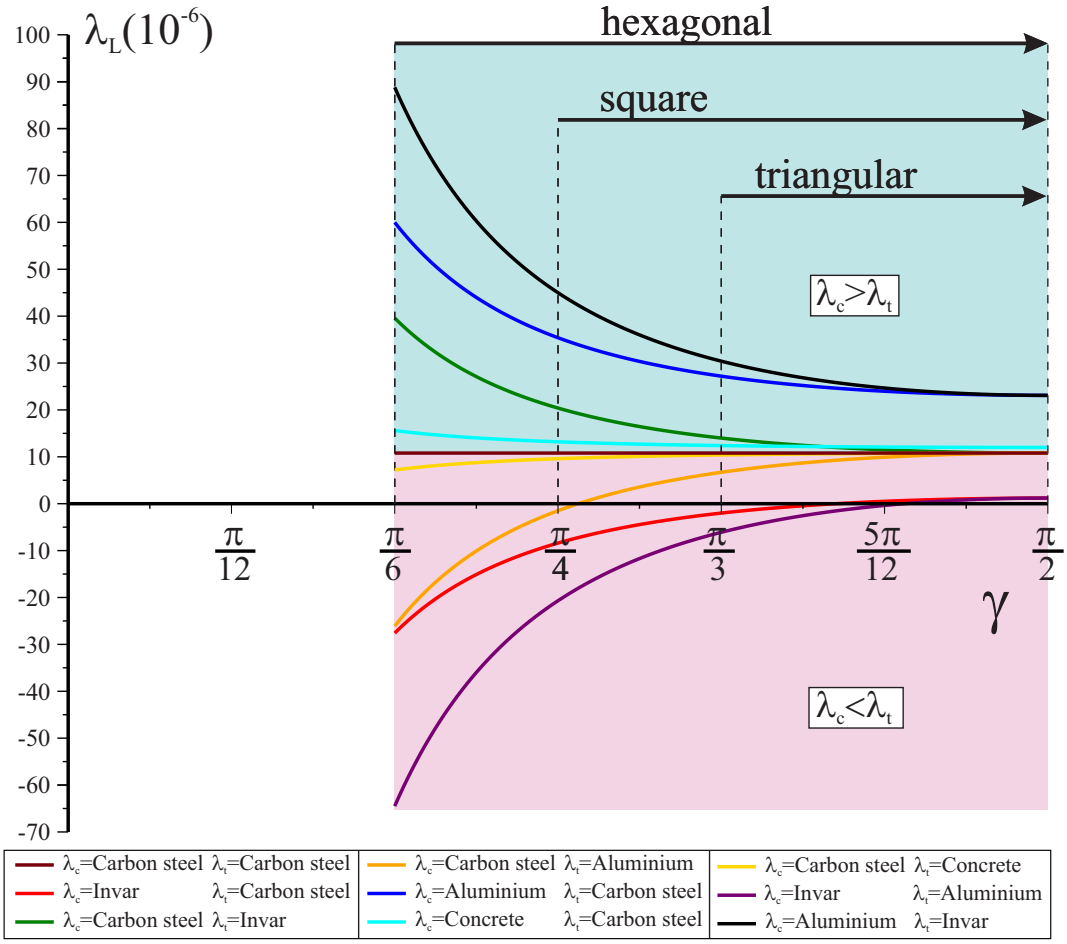

FIGURE 3.13: Effective coefficients of thermal expansion for lattices, made of different couples of materials, as a function of the angle γ.

For completeness we introduce now in eqn. (3.7) some values of the coefficient of thermal expansion typical of common materials, listed in Table 3.2. In Fig. 3.13 the effective linear coefficient of thermal expansion is given as a function of the angle γ for different couples of materials characterized by different value of λ_c and

λ_t. In the blue part of the graph ($\lambda_L > 10^{-5}$) the lattices have $\lambda_c > \lambda_t$, in the red one λ_c is lower than λ_t. When γ increases, the effective coefficient of thermal expansion tends to λ_c, this is evident in particular beyond $\gamma = 5\pi/12$. On the contrary for angles γ sufficiently close to $\gamma = \pi/6$ the effective coefficient of thermal expansion strongly differs from the coefficients of the constituent materials.

As a conclusion we consider the three-dimensional lattice described in Chapter 2, and shown in Fig. 3.14, the blue and red crossbeams have a coefficient of thermal expansion λ_c and the green trusses have a coefficient of thermal expansion λ_t.

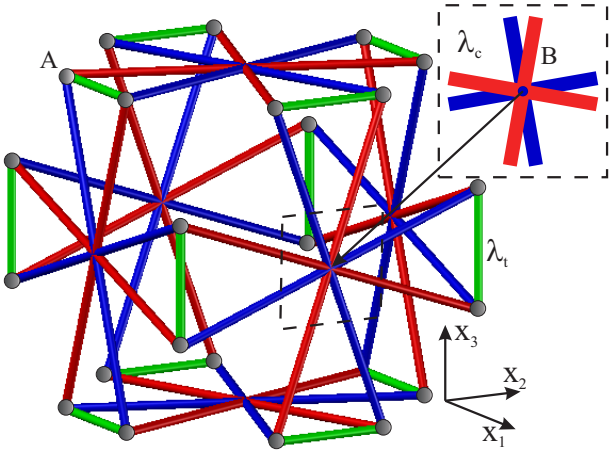

FIGURE 3.14: Three-dimensional lattice with tunable coefficient of thermal expansion, the blue and red crossbeams have a coefficient of thermal expansion λ_c and the green trusses have a coefficient of thermal expansion λ_t.

The macroscopic thermal volume deformation of the lattice λ_V is

$$\begin{aligned}\lambda_V \Delta T = \frac{V_1 - V_0}{V_0} = \frac{3\Delta T}{\sin^2\gamma}(\lambda_c - \lambda_t \cos^2\gamma) + \frac{3\Delta T^2}{\sin^4\gamma}(\lambda_c^2 - 2\lambda_c\lambda_t\cos^2\gamma + \\ + \lambda_t^2\cos^4\gamma) + \frac{\Delta T^3}{\sin^6\gamma}(\lambda_c^3 - 3\lambda_c^2\lambda_t\cos^2\gamma + 3\lambda_c\lambda_t^2\cos^4\gamma - \lambda_t^3\cos^6\gamma),\end{aligned} \tag{3.8}$$

which to leading order in the small parameters $\lambda_c\Delta T$, $\lambda_t\Delta T$ gives

$$\lambda_V = 3\lambda_L = \frac{3}{\sin^2\gamma}(\lambda_c - \lambda_t\cos^2\gamma), \tag{3.9}$$

which corresponds perfectly to the plane structure previously presented.

3.3 The lattice with negative thermal expansion

Here we show experimental evidence that the micro-structured media with tunable coefficient of thermal expansion can have negative thermal expansion. The actual two-dimensional micro-structured lattice was realized with Y shaped elements in two plane layers, the upper one in blue colour and the lower one in red, and with shape memory alloys longitudinal springs (SMA). The Y shaped elements were obtained, using an Engraving Machine (EGX-600 by Roland), from sheets of PMMA, a polymeric material (PERSPEX® blue 727 and red 431 distributed from Bayer AG), they are thick $4\,mm$, with Young's modulus $E = 3350\,MPa$, Poisson's ratio $\nu = 0.35$ and CTE= $56 - 66 \cdot 10^{-6} K^{-1}$ at $20^{o}C$. The SMA (NiTiCu) flat springs from Kellogg's research Lab (diameter $0.5\,mm$, length $50\,mm$, amplitude $20\,mm$, pitch $20\,mm$ at body transition temperature) were employed to amplify the effect of the thermal expansion and they were connected to the hexagonal periodic network via specially designed elements. The Y shaped elements are joined together

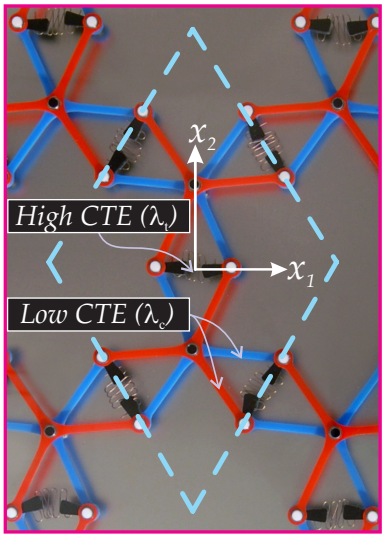

FIGURE 3.15: Geometrical properties of the lattice, the blue and red crossbeams have a coefficient of thermal expansion λ_c and the memory alloy longitudinal springs have a coefficient of thermal expansion λ_t.

by hinges made up with two roller bearings (from MISUMI Europa GmbH) to reduce the rotational friction, one hinge couples the red and the blue Y shaped elements in their centre whereas other hinges are placed at the end of each arm to join the different couples and the SMA springs. In Fig. 3.15 it is possible to see in detail the geometrical properties of the lattice. The temperature of the lattice was varied by keeping it in a temperature controlled environment consisting of a metal tray with a transparent plastic cover, where the lattice was free to expand

and contract. The source of heat was an hot plate controlled by a rugged and reconfigurable control and monitoring system (NI CompactRIO) interfaced with a system-design platform commonly used for data acquisition and instrument control (Labview2013-National Instruments). The temperature was simultaneously measured by a resistance temperature detector (PT100). The temperature of the environment was then increased gradually and linearly, see Fig. 3.16. The exper-

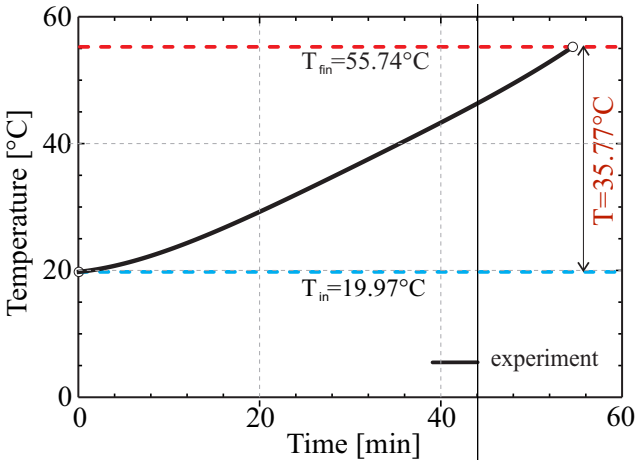

FIGURE 3.16: Temperature of the experimental environment during the experiment.

imental set-up, as shown in Fig. 3.16, was mounted on an optical table (made by Technical Manufacturing Corporation) and equipped with four *Gimbal Piston*^{TM} air isolators to prevent spurious vibrations. The table was also monitored for vibrations using Integrated electronic piezoelectric (IEPE) accelerometers (PCB Piezotronics Inc., model 333B50). During the test, photos were taken with a

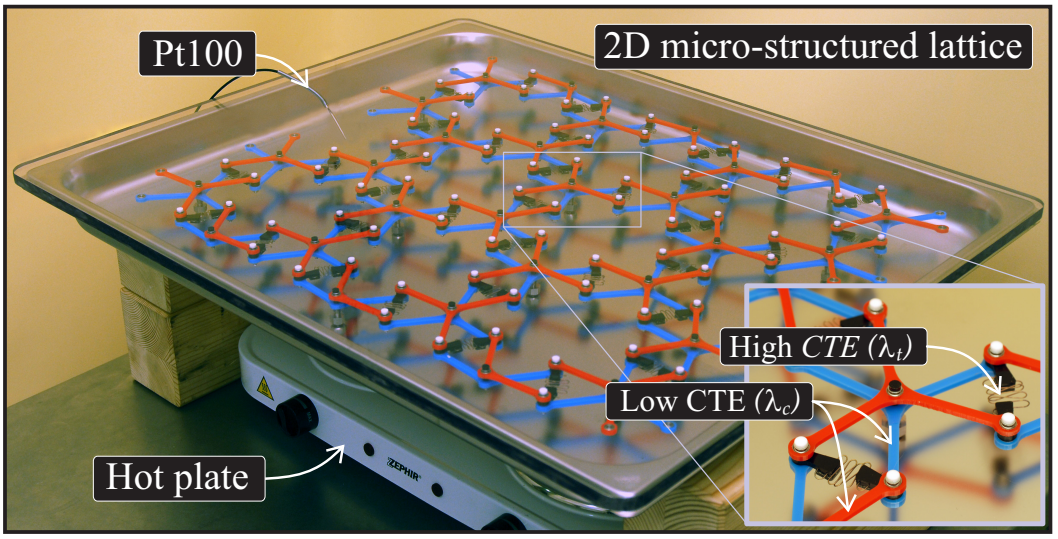

FIGURE 3.17: Experimental set-up.

Sony digital camera (model NEX 5N equipped with 3.5-5.6/18-55 lens, optical steady shot from Sony Corporation) and movies were recorded with a Sony camcorder (model HDR-XR550VE). The experiment, which confirms that the lattice can show negative thermal expansion, was performed at the 'Instabilities Lab', (http://www.ing.unitn.it/dims/ssmg/) of the University of Trento in collaboration with Dr.Diego Misseroni. The micro-structured lattice subjected to a positive change of temperature shrinks, as it can be observed in Fig. 3.18, where the yellow dashed square, whose vertices coincide with points of the lattice which move macroscopically, identifies the initial configuration whereas the white dashed square identifies the same points in the final configuration. We are now able to

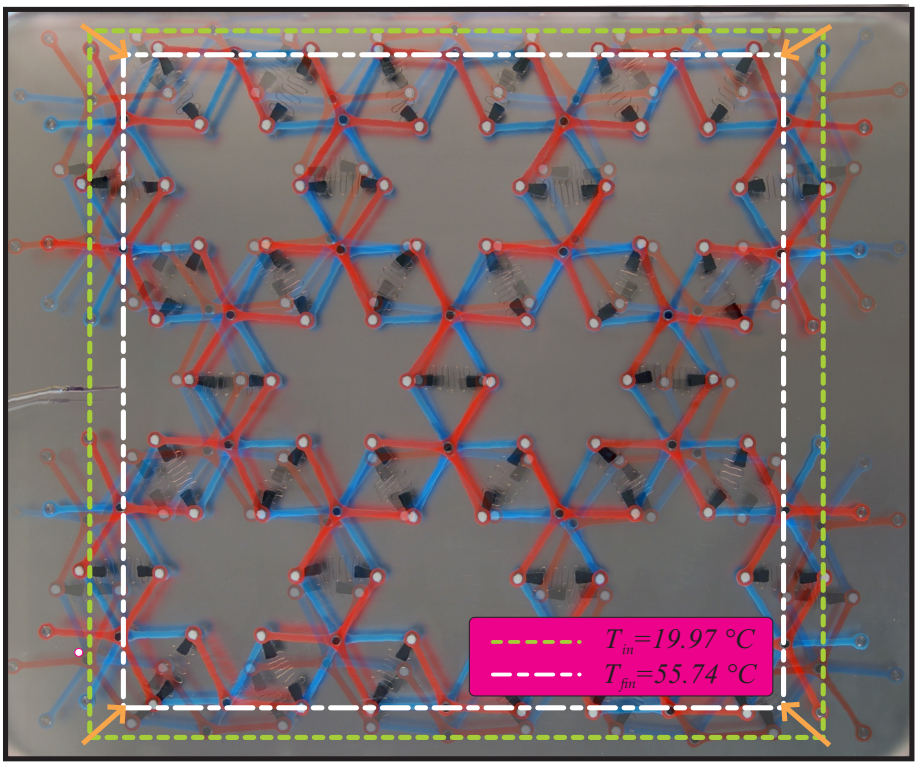

FIGURE 3.18: Lattice subjected to a positive change of temperature, yellow dashed square identifies the initial configuration whereas the white dashed square identifies the same points in the final configuration.

evaluate the coefficient of linear thermal expansion of the lattice, obtained with our experiment. Observing the Fig. 3.19(a), the initial distance L_0, for $T = 19.97^oC$ between two points that move macroscopically, is $L_0 = 7.41cm$. Increasing the temperature up to the final value of $T = 55.74^oC$ the distance between the two points decreases, and its final value becomes $L_1 = 6.91cm$, see Fig. 3.19(b). The resulting coefficient of linear thermal expansion results negative and its value is $\lambda_L = (L_1 - L_0)/(L_0\Delta T) = -0.001887\ 1/^o\text{C}$.

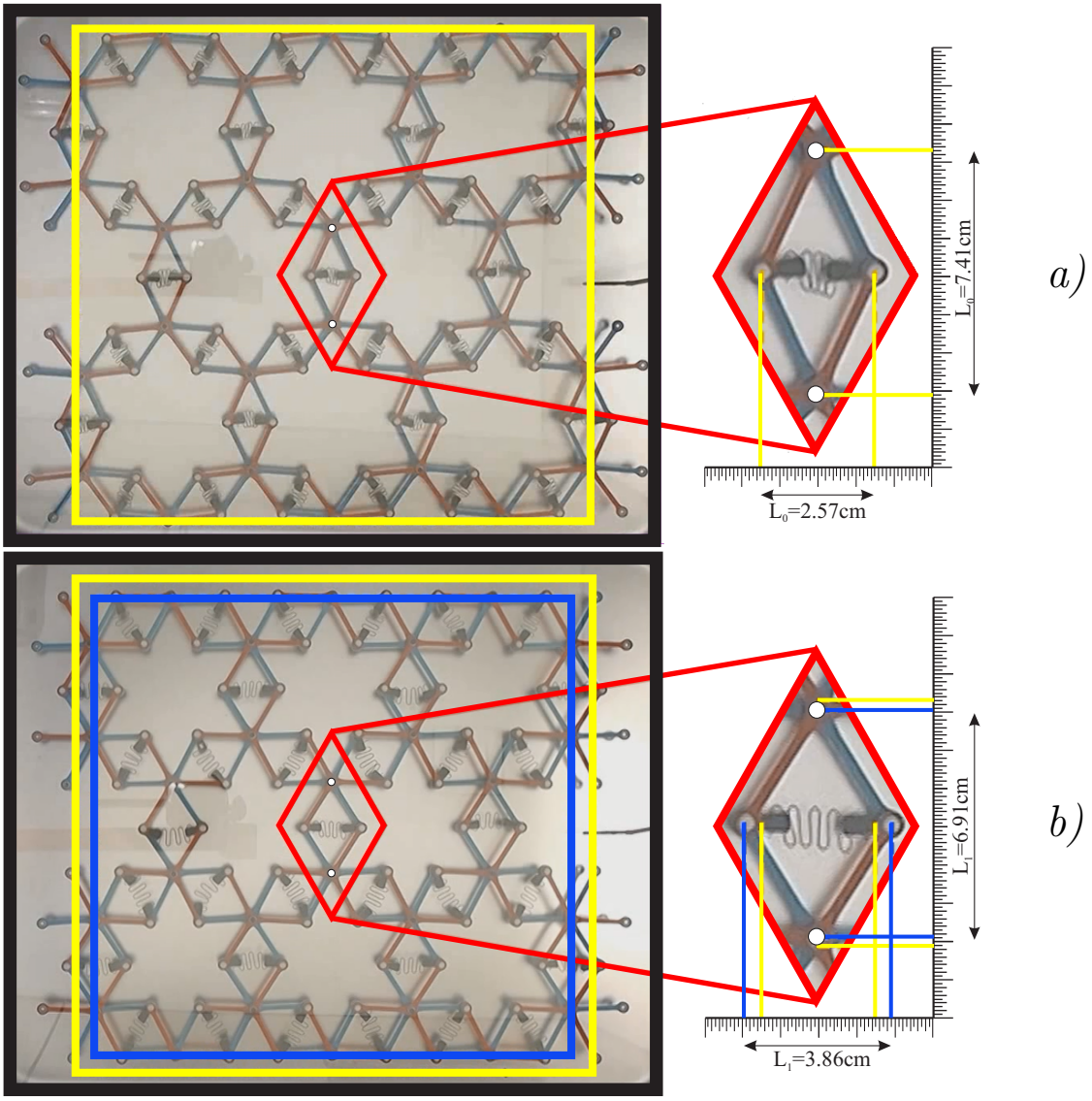

FIGURE 3.19: Evaluation of the expansion of the lattice. a) Initial configuration at $T = 19.97^oC$ (in yellow). b) Final configuration at $T = 55.74^oC$ in (blue).

Conclusion

In this work a new family of auxetic lattices with negative Poisson's ratio has been proposed, in addition to the auxetic behaviour the lattices can be designed to provide a negative coefficient of thermal expansion. In literature there are not several models that provide simultaneously these two counterintuitive properties. The mechanical and thermal effective properties of the lattices depend on the properties of the single constituents and on the topology of the micro-structures. These unusual properties are achievable for each topology provided that the constituent materials are different. Two-dimensional hexagonal, square and triangular micro-structures have been studied with Poisson's ratio arbitrarily close to -1. The triangular and hexagonal lattices show isotropic mechanical behaviour, whereas the square plane lattice shows cubic behaviour, see Chapter 1. The basic idea of the two-dimensional media has been extended to a three-dimensional cubic lattice focusing in particular on the extreme values of the Poisson's ratio, see Chapter 2, its mechanical behaviour results cubic with global negative Poisson's ratio arbitrarily close to -1. The lattice has been properly modified to ensure an isotropic behaviour. In the plane case a complete analytical analysis of the static behaviour has been performed and the effective mechanical and thermal properties have been given in closed form, see Chapters 1 and 3, whereas the three-dimensional micro-structured lattice has been studied numerically in regard to the mechanical properties, because of the considerable complications involved, see Chapter 2, and analytically in regard to the coefficient of thermal expansion, see Chapter 3. Two experiments were realized to provide evidences which confirmed the theoretical models, at the end of Chapter 1 the square lattice subjected to an axial load confirm a Poisson's ratio very close to -1, and at the end of Chapter 3 the hexagonal lattice subjected to a thermal load confirm a negative coefficient of thermal expansion.

Comparisons with classical honeycomb lattices show that the mechanical parameters and the geometry of our models can be set in order to have effective properties of the same order of magnitude without significant penalization in terms of strength and stiffness, in particular when these two features are required, as in the structural field, triangular and square lattices result to be more suitable than the hexagonal one since they deforms mainly by axial deformation of cell walls rather than by bending deformation. We remember that the properties studied here are scale-independent so the lattices can be seen both as micro-structured media and as frame structures, for this reason they can be used in several engineering fields: bio-medic, structural, aeronautics, civil. Especially in the last three fields there are quite direct applications since the design of the internal hinges is a problem that has already been solved technologically, and different joint structures are already produced, moreover with the advent of 3D printing technology the capability to create the proposed micro-structures at different scales open new and exciting prospects in terms of possible technological applications. An interesting aspect concerns the thermal behaviour, it is possible to reach strongly negative, null, or positive coefficient of thermal expansion using conventional constituent materials with positive thermal expansion, the macroscopic thermal expansion is not anymore an intrinsic property of the material but it is correlated to the micro-structure and to the ratio between the thermal coefficients of the constituent materials. This allow for example to realize structure insensitive to temperature changes or with a specific coefficient of thermal expansion depending on the application, without no need to use special materials generally very expensive.

Appendix A

Application of the Principle of Virtual Work.

A.1 Hexagonal lattice with longitudinal springs

Here the computation of the Principle of the Virtual Works is specified with reference to the hexagonal lattice with longitudinal springs schematized in Fig. A.1.

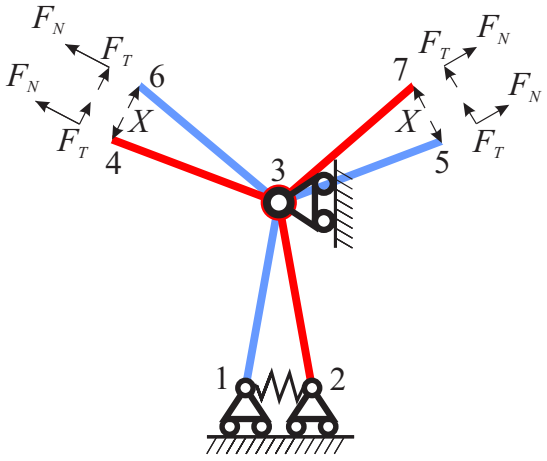

FIGURE A.1: Simplified hexagonal structure for the application of the Principle of Virtual Work.

With the subscript 0 are indicated the internal actions (bending moments M, axial forces N and spring forces S^L) of the equivalent statically determined (or isostatic) system, obtained disconnecting two springs. With the subscript 1 are indicated the internal actions of the equivalent statically determined (or isostatic) system,

obtained disconnecting two springs and introducing two unitary forces to replace them. In the Table A.1 are shown the internal actions of each beam.

Beam	**Axial force N**	**Bending moment M**
23	$N_0 = \frac{(2\cos^2\gamma+1)F_N-\sqrt{3}F_T}{\sin\gamma}$ $N_1 = -2\cos\gamma$	$M_0 = 2\,F_N\cos\gamma\,x$ $M_1 = -2\sin\gamma\,x$
34	$N_0 = F_T\cos\gamma + F_N\sin\gamma$ $N_1 = \cos\gamma$	$M_0 = -F_T\sin\gamma\,x + F_N\cos\gamma\,x$ $M_1 = -\sin\gamma\,x$
37	$N_0 = -F_T\cos\gamma + F_N\sin\gamma$ $N_1 = \cos\gamma$	$M_0 = -F_T\sin\gamma\,x - F_N\cos\gamma\,x$ $M_1 = \sin\gamma\,x$
13	$N_0 = \frac{F_N\cos 2\gamma+2F_N-F_T\sqrt{3}}{\sin\gamma}$ $N_1 = -2\cos\gamma$	$M_0 = 2\,F_N\cos\gamma\,x$ $M_1 = -2\sin\gamma\,x$
36	$N_0 = -F_T\cos\gamma + F_N\sin\gamma$ $N_1 = \cos\gamma$	$M_0 = -F_T\ \sin\gamma\,x - F_N\cos\gamma\,x$ $M_1 = \sin\gamma\,x$
35	$N_0 = F_T\cos\gamma + F_N\sin\gamma$ $N_1 = \cos\gamma$	$M_0 = -F_T\sin\gamma\,x + F_N\cos\gamma\,x$ $M_1 = -\sin\gamma\,x$
Spring force S		
$S_0 = \frac{-\sqrt{3}\,F_T\cos\gamma+3\,F_N\cos\gamma}{\sin\gamma}$	$S_1 = -2$	

TABLE A.1: Internal actions in the hexagonal lattice.

The unknown X of eqn. (1.29) is

$$X = -\frac{\sum_{beam}\int_0^p\left(M_0\frac{M_1}{EJ}+N_0\frac{N_1}{EA}\right)ds+\sum_{spring}S_0^L\frac{S_1^L}{k_L/2}}{\sum_{beam}\int_0^p\left(M_1\frac{M_1}{EJ}+N_1\frac{N_1}{EA}\right)ds+\sum_{spring}S_1^L\frac{S_1^L}{k_L/2}} = \\ = \left(F_N-\frac{\sqrt{3}(1+\alpha_1)}{3+3\alpha_1\cos^2\gamma+\alpha_2\sin^2\gamma}F_T\right)\mathrm{cotg}\gamma. \tag{A.1}$$

The external applied forces F_N, and F_T are:

$$F_T = \frac{3}{2}\frac{k_L p\sqrt{3}\sin\gamma(\sin^2\gamma\alpha_2+3\cos^2\gamma\alpha_1+3)(\varepsilon_{11}-\varepsilon_{22})}{\sin^4\gamma\alpha_2^2+9\cos^4\gamma\alpha_1^2+3(2\sin^2\gamma\cos^2\gamma+1)\alpha_1\alpha_2+3\alpha_2+9\alpha_1}, \tag{A.2}$$

$$F_N = \frac{1}{2}\frac{k_L p\sin\gamma(c_1\alpha_1^2+c_2\alpha_2\alpha_1+c_3\alpha_1+c_4\alpha_2^2+c_5\alpha_2+3c_6)\varepsilon_{11}}{c_{11}\alpha_1^3+c_{10}\alpha_1\alpha_2^2+c_{12}\alpha_1^2\alpha_2+c_{13}\alpha_2^2+c_{14}\alpha_1^2+c_{15}\alpha_1\alpha_2+3c_6\alpha_1+c_6\alpha_2}+ \\ +\frac{k_p\sin\gamma(c_7\alpha_1^2+c_8\alpha_1\alpha_2+c_9\alpha_1+c_4\alpha_2^2+3c_{10}\alpha_2-3c_6)\varepsilon_{22}}{c_{11}\alpha_1^3+c_{10}\alpha_1\alpha_2^2+c_{12}\alpha_1^2\alpha_2+c_{13}\alpha_2^2+c_{14}\alpha_1^2+c_{15}\alpha_1\alpha_2+3c_6\alpha_1+c_6\alpha_2}, \tag{A.3}$$

where:

$$
\begin{aligned}
c_1 &= 9(\sin^2\gamma\cos^4\gamma + \cos^2\gamma), & c_2 &= 6(1 + \cos^6\gamma - 2\cos^4\gamma),\\
c_3 &= -9(\sin^2\gamma\cos^2\gamma - 2), & c_4 &= \sin^6\gamma,\\
c_5 &= -3(\cos^4\gamma - 1), & c_6 &= 3\cos^2\gamma,\\
c_7 &= 9(\sin^2\gamma\cos^4\gamma - \cos^2\gamma), & c_8 &= 6\sin^4\gamma\cos^2\gamma,\\
c_9 &= -9(\cos^4\gamma + \cos^2\gamma), & c_{10} &= \sin^4\gamma,\\
c_{11} &= 9\cos^4\gamma, & c_{12} &= 3(2\sin^2\gamma\cos^2\gamma + 1),\\
c_{13} &= \sin^4\gamma\cos^2\gamma, & c_{14} &= 9(\cos^6\gamma + 1),\\
c_{15} &= 3(2\sin^2\gamma\cos\gamma^4 + \cos\gamma^2 + 1).
\end{aligned}
\tag{A.4}
$$

A.2 Triangular lattice with longitudinal springs

Here the computation of the Principle of the Virtual Works is specified with reference to the triangular lattice with longitudinal springs schematized in Fig. A.2.

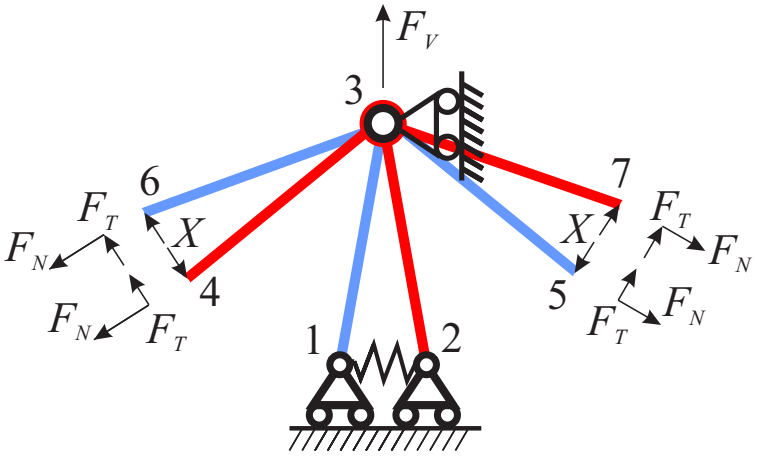

FIGURE A.2: Simplified triangular structure for the application of the Principle of Virtual Work.

In the Table A.2 are shown the internal actions of each beam.

Beam	**Axial force N**	**Bending moment M**
23	$N_0 = \frac{(2\cos^2\gamma)F_N+F}{\sin\gamma}$ $N_1 = -2\cos\gamma$	$M_0 = 2\,F_N\cos\gamma\,x$ $M_1 = -2\sin\gamma\,x$
34	$N_0 = F_T\cos\gamma + F_N\sin\gamma$ $N_1 = \cos\gamma$	$M_0 = -F_T\sin\gamma\,x + F_N\cos\gamma\,x$ $M_1 = -\sin\gamma\,x$
37	$N_0 = -F_T\cos\gamma + F_N\sin\gamma$ $N_1 = \cos\gamma$	$M_0 = -F_T\sin\gamma\,x - F_N\cos\gamma\,x$ $M_1 = \sin\gamma\,x$
13	$N_0 = \frac{F_N(\cos 2\gamma+1)+F}{\sin\gamma}$ $N_1 = -2\cos\gamma$	$M_0 = 2\,F_N\cos\gamma\,x$ $M_1 = -2\sin\gamma\,x$
36	$N_0 = -F_T\cos\gamma + F_N\sin\gamma$ $N_1 = \cos\gamma$	$M_0 = -F_T\ \sin\gamma\,x - F_N\cos\gamma\,x$ $M_1 = \sin\gamma\,x$
35	$N_0 = F_T\cos\gamma + F_N\sin\gamma$ $N_1 = \cos\gamma$	$M_0 = -F_T\sin\gamma\,x + F_N\cos\gamma\,x$ $M_1 = -\sin\gamma\,x$
Spring force S		
$S_0 = \frac{F\cos\gamma+2\,F_N\cos\gamma}{\sin\gamma}$	$S_1 = -2$	

TABLE A.2: Internal actions in the triangular lattice.

The unknown X of eqn. (1.42) is:

$$X = \frac{(3\cos^2\gamma\alpha_1 - \alpha_1 + sin^2\gamma\alpha_2 + 2)F_N + (1+\alpha_1)F}{\sin^2\gamma\alpha_2 + 3\cos^2\gamma\alpha_1 + 3}\text{cotg}\gamma. \tag{A.5}$$

The external applied forces F_T, F_N and F are:

$$F_T = \frac{3}{4}\frac{k_L p\sqrt{3}\sin\gamma(\varepsilon_{22}-\varepsilon_{11})}{\sin^2\gamma\alpha_2 + 3\cos^2\gamma\alpha_1}, \tag{A.6}$$

$$\begin{aligned} F_N = {} & \frac{k_L p\sin\gamma}{4}\frac{(3c_1\alpha_1^2 + 3c_2\alpha_1\alpha_2 + c_3\alpha_1 + 3c_4\alpha_2 + c_1)\varepsilon_{11}}{\alpha_2\alpha_1^2 + 3c_2\alpha_1^2 + 2c_1\alpha_2\alpha_1 + c_6\alpha_2 + 3c_4\alpha_1} + \\ & + \frac{k_L p\sin\gamma}{4}\frac{(-3c_1\alpha_1^2 + c_2\gamma\alpha_1\alpha_2 + c_5\alpha_1 + c_4\alpha_2 - c_1)\varepsilon_{22}}{\alpha_2\alpha_1^2 + 3c_2\alpha_1^2 + 2c_1\alpha_2\alpha_1 + c_6\alpha_2 + 3c_4\alpha_1}, \end{aligned} \tag{A.7}$$

$$\begin{aligned} F = {} & \frac{k_L p\sin\gamma}{2}\frac{(3c_1\alpha_1^2 + 2c_2\alpha_1\alpha_2 + c_7\alpha_1 + 2c_4\alpha_2 + 3c_1)\varepsilon_{22}}{\alpha_2\alpha_1^2 + 3c_2\alpha_1^2 + 2c_1\alpha_2\alpha_1 + c_6\alpha_2 + 3c_4\alpha_1} - \\ & - \frac{k_L p\sin\gamma}{2}\frac{-3(c_1\alpha_1^2 + 2c_1\alpha_1 + c_1)\varepsilon_{11} +}{\alpha_2\alpha_1^2 + 3c_2\alpha_1^2 + 2c_1\alpha_2\alpha_1 + c_6\alpha_2 + 3c_4\alpha_1}, \end{aligned} \tag{A.8}$$

where:

$$
\begin{aligned}
c_1 &= \cos^2\gamma, & c_2 &= \sin^2\gamma,\\
c_3 &= (9\cos^4\gamma - 12\cos^2\gamma + 9), & c_4 &= \sin^2\gamma\cos^2\gamma,\\
c_5 &= 3(\cos^4\gamma - 4\cos^2\gamma + 1), & c_6 &= \cos^4\gamma,\\
c_7 &= 6(\cos^4\gamma + \sin^2\gamma). & &
\end{aligned} \tag{A.9}
$$

Appendix B

Data processing

The Poisson's ratio values $\nu(t_i, p_j)$ in each of the 16 points p_j, see Fig. B.1, and for each of the 14 time instants t_i are given in Table B.1 and Table B.2.

	Points							
$\mathbf{t}_i$	**1**	**2**	**3**	**4**	**5**	**6**	**7**	**8**
1	-	-	-	-	-	-	-	-
2	-1,0043	-0,8905	-0,9531	-0,9419	-0,9945	-0,9863	-1,0600	-0,9100
3	-0,9841	-0,9847	-0,8904	-1,0549	-1,0501	-0,9951	-1,0248	-1,0103
4	-0,9920	-1,0198	-0,9564	-1,0375	-1,0473	-1,0034	-1,0707	-1,0457
5	-1,0247	-0,9928	-0,9260	-1,0272	-0,9921	-0,8506	-1,0021	-0,9567
6	-1,0513	-0,9397	-0,9686	-0,9675	-0,9230	-1,0659	-0,9901	-0,9932
7	-1,0022	-0,9189	-1,0226	-1,0048	-0,9875	-0,9281	-1,1420	-0,9345
8	-1,0011	-0,9820	-0,9495	-1,0619	-1,0239	-0,9960	-1,0637	-1,07459
9	-1,0281	-0,9724	-0,9639	-0,9831	-0,9691	-1,0639	-1,0141	-1,0100
10	-1,0361	-1,0083	-0,9301	-1,0554	-1,0184	-1,0563	-0,9722	-0,9692
11	-1,0122	-0,9858	-0,9838	-0,9904	-0,9778	-0,9405	-1,0284	-1,0186
12	-1,0014	-0,9833	-0,9944	-0,9959	-1,0028	-0,9675	-1,0349	-1,0321
13	-0,9898	-0,9878	-1,0012	-1,0280	-0,9670	-0,9786	-1,0130	-0,9531
14	-0,9778	-0,9455	-1,0221	-1,0548	-0,9531	-0,9489	-1,0305	-1,0371

TABLE B.1: Experimental Poisson's ratio values $\nu(t_i, p_i)$ from point 1 to point 8.

In Table B.1 the values of $\nu(t_i, p_i)$ refer to the points from 1 to 8, whereas in Table B.2 from 9 to 16. The time t_1 represents the un-deformed configuration, before the application of the load.

	Points							
$\mathbf{t}_i$	**9**	**10**	**11**	**12**	**13**	**14**	**15**	**16**
1	-	-	-	-	-	-	-	-
2	-1,0670	-1,0895	-1,0485	-0,9769	-1,0743	-1,0056	-0,9842	-0,9105
3	-0,9567	-1,0874	-1,0567	-1,0234	-1,0805	-0,9856	-0,9912	-0,9504
4	-0,9265	-1,0620	-1,0394	-0,9458	-1,0598	-0,9834	-0,9754	-0,8956
5	-0,9287	-0,9750	-1,0267	-1,0973	-1,0387	-1,0366	-0,9820	-0,8673
6	-0,8800	-1,0118	-1,0698	-0,9567	-0,9604	-1,0127	-0,9468	-0,9010
7	-1,0641	-0,9808	-0,9941	-0,9943	-0,9377	-0,9660	-0,9658	-0,8719
8	-0,9126	-0,9867	-1,0653	-0,9326	-0,9523	-1,0165	-0,9759	-0,9329
9	-0,9331	-0,9429	-1,0212	-0,9706	-0,9682	-0,9639	-1,0188	-0,9691
10	-0,9647	-0,9540	-1,0432	-1,0064	-0,9642	-0,9722	-0,9900	-0,9954
11	-0,9811	-0,9653	-1,0154	-0,9940	-0,9705	-0,9681	-1,0232	-0,9895
12	-0,9802	-0,9678	-1,0307	-0,9698	-0,9856	-1,0096	-0,9978	-0,9793
13	-0,9948	-0,9811	-1,0135	-0,9739	-0,9992	-1,0227	-0,9768	-0,9700
14	-1,0381	-0,9844	-1,0303	-0,9568	-1,0132	-1,0417	-0,9590	-0,9765

TABLE B.2: Experimental Poisson's ratio values $\nu(t_i, p_i)$ from point 9 to point 16.

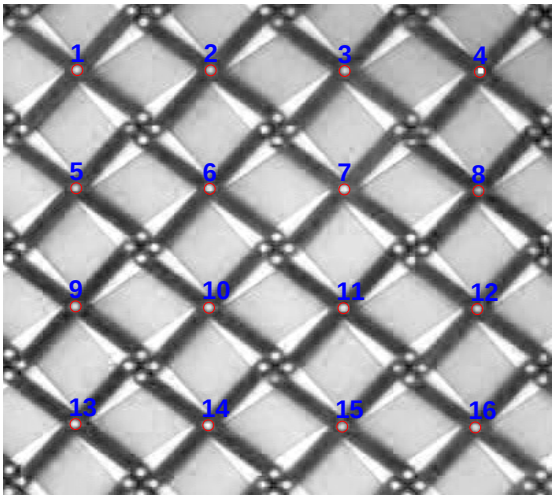

FIGURE B.1: 16 joint points of the lattice of which were calculated the displacements.

The values of the sample mean of $\nu(t_i, p_j)$ at any time t_i obtained from eqn. (1.73), the sample standard deviation $\sigma_\nu(t_i)$ obtained from eqn. (1.74), the standard error of the mean $\delta_\nu(t_i)$ obtained from eqn. (1.75), and the weights ω_i obtained from eqn. (1.77), are shown in Table B.3.

$\mathbf{t}_i$	$\bar{\nu}(t_i)$	$\sigma_\nu(t_i)$	$\delta_\nu(t_i)$	ω_i
1	-	-	-	-
2	-0.9936	0.0622	0.0155	4135,6102
3	-1.0079	0.0518	0.0130	5959.3943
4	-1.0038	0.0529	0.0132	5719.5737
5	-0.9828	0.0648	0.0162	3806.0803
6	-0.8648	0.4737	0.1184	71.3050
7	-0.9822	0.0627	0.0157	4067.5228
8	-0.9955	0.0522	0.0130	5877.6290
9	-0.9870	0.0351	0.0088	13006.6051
10	-0.9960	0.0381	0.0095	11037.8243
11	-0.9903	0.0242	0.0060	27429.2531
12	-0.9958	0.0222	0.0055	32555.4600
13	-0.9907	0.0212	0.0053	35475.0027
14	-0.9981	0.0389	0.0097	10598.0213

TABLE B.3: Statistic parameters: sample mean, sample standard deviation, standard error and weights.

Bibliography

[1] R.S. Lakes. Foam structure with a negative poisson's ratio. *Science*, 235: 10348–1040, 1987.

[2] K.E. Evans. Auxetic polymers: a new range of materials. *Endeavour*, 15(4): 170–174, 1991.

[3] K.E. Evans, M.A. Nkansah, I.J. Hutchinson, and S.C. Rogers. Molecular network design. *Nature*, 353(124), 1991. doi: 10.1038/353124a0.

[4] G.W. Milton. Composite materials with poisson's ratio close to -1. *Journal of the Mechanics and Physics of Solids*, 40(5):1105–1137, 1992.

[5] E.A. Friis, R.S. Lakes, and J.B. Park. Negative poisson's ratio polymeric and metallic materials. *Journal of Materials Science*, 23:4406–4414, 1988.

[6] A.Y. Haeri, D.J. Weidner, and J.B. Parise. Elasticity of α-cristobalite: a silicon dioxide with a negative poisson's ratio. *Science*, 257:650–652, 1992.

[7] R.H. Baughman, J.M. Shacklette, A.A. Zakhidev, and S. Stafström. Negative poisson's ratio as a common feature of cubic metals. *Nature*, 392: 362–365, 1998.

[8] L.J. Hall, V.R. Coluci, D.S. Galvão, M.E. Kozlov, M. Zhang, S.O. Dantas, and R.H. Baughman. Sign change of poisson's ratio for carbon nanotube sheets. *Science*, 320(5875):504–507, 2008. doi: 10.1126/science.1149815.

[9] R.S. Webber, K.L. Alderson, and K.E. Evans. A novel fabrication route for auxetic polyethylene part 2: mechanical properties. *Polymer Engineering & Science*, 48(7):351–1358, 2008.

[10] R.S. Lakes and K.E. Elms. Indentability of conventional and negative poisson's ratio foams. *Journal of Composite Materials*, 27(12):1193–1202, 1993.

[11] N. Chan and K.E. Evans. Indentation resilience of conventional and auxetic foams. *Journal of Cellular Plastics*, 34(3):231–260, 1998.

[12] T. Rouxe. Elastic properties and short-to-medium range order in glasses. *Journal of the American Ceramic Society*, 90:3019–3039, 2007.

[13] T. Rouxel, H. Ji, T. Hammouda, and A. Moreac. Poisson's ratio and the densification of glass under high pressure. *Physical Review Letters*, 100(225501), 2008.

[14] A. Bezazi and F. Scarpa. Mechanical behaviour of conventional and negative poisson's ratio thermoplastic polyurethane foams under compressive cyclic loading. *International Journal of Fatigue*, 29(5):922–930, 2007. doi: 10.1016/j.ijfatigue.2006.07.015.

[15] A. Alderson, J. Rasburn, S. Ameer-Be, P.G. Mullarkey, W. Perrie, and K.E. Evans. An auxetic filter: A tuneable filter displaying enhanced size selectivity or defouling properties. *Industrial & Engineering Chemistry Research*, 39:654–665, 2000. doi: 10.1021/ie990572w.

[16] J. Rasburn, P.G. Mullarkey, K.E. Evans, A. Alderson, S. Ameer-Beg, and W. Perrie. Auxetic structures for variable permeability systems. *AIChE Journal*, 47(11):2623–2626, 2001. doi: 10.1002/aic.690471125.

[17] J.B. Choi and R.S. Lakes. Design of a fastener based on negative poisson's ratio foam. *Cellular Polymers Journal*, 10(3):205–212, 1991.

[18] G.E. Stavroulakis. Auxetic behaviour: appearance and engineering applications. *Physica status solidi B*, 242(3):710–720, 2005. doi: 10.1002/pssb.200460388.

[19] M. Bianchi, F.L. Scarpa, and C.W. Smith. Shape memory behaviour in auxetic foams: mechanical properties. *Acta Materialia*, 58(3):858–865, 2010. doi: 10.1016/j.actamat.2009.09.063.

[20] B. Howell, P. Prendergast, and L. Hansen. Examination of acoustic behavior of negative poisson's ratio materials. *Applied Acoustics*, 43(2):141–148, 1994. doi: 10.1016/0003-682X(94)90057-4.

[21] F. Scarpa, L.G. Ciffo, and J.R. Yates. Dynamic properties of high structural integrity auxetic open cell foam. *Smart Materials and Structures*, 13(1): 49–56, 2004.

[22] M. Burke. A stretch of the imagination. *New Scientist*, 154(2085):36–39, 1997.

[23] C.P. Chen and R.S. Lakes. Dynamic wave dispersion and loss properties of conventional and negative poisson's ratio polymeric cellular materials. *Cellular Polymers Journal*, 8(5):343–369, 1989.

[24] M. Ruzzene. Vibration and sound radiation of sandwich beams with honeycomb truss core. *Journal of Sound and Vibration*, 277(4-5):741–763, 2004.

[25] F. Scarpa, F. Dallocchio, and M. Ruzzene. Identification of acoustic properties of auxetic foams. *Proceedings SPIE, Smart Structures and Materials: Damping and Isolation*, 5052:468–474, 2003. doi: 10.1117/12.487559.

[26] K.F. Tee, A. Spadoni, F. Scarpa, and M. Ruzzene. Wave propagation in auxetic tetrachiral honeycomb. *Journal of Vibration and Acoustics*, 132(3), 2010. doi: 10.1115/1.4000785.

[27] A.E.H. Love. A treatise on the mathematical theory of elasticity. *Dover Publications, New York (4th ed.)*, 1944.

[28] D.D. Gunton and G. A. Saunders. The young's modulus and poisson's ratio of arsenic, antimony and bismuth. *Journal of Materials Science*, 7(9):1061–1068, 1972.

[29] Y. Li. The anisotropic behavior of poisson's ratio, young's modulus, and shear modulus in hexagonal materials. *Physica status solidi A*, 38(1):171–175, 1976.

[30] C. Lees, J.F. Vincent, and J.E. Hillerton. Poisson's ratio in skin. *Bio-Medical Materials and Engineering*, 1(1):19–23, 1991.

[31] J.L. Williams and J.L. Lewis. Properties and an anisotropic model of cancellous bone from the proximal tibial epiphysis. *Journal of Biomechanical Engineering*, 104(1):50–56, 1982.

[32] R.F. Almgren. An isotropic three-dimensional structure with poisson's ratio=-1. *Journal of Elasticity*, 15(4):427–430, 1985. doi: 10.1007/BF00042531.

[33] A.G. Kolpakov. Determination of average characteristic of elastic frameworks. *Journal of Applied Mathematics and Mechanics*, 49(6):739–745, 1985.

[34] K.E. Evans and A. Alderson. Auxetic materials: Functional materials and structures from lateral thinking! *Advanced Materials*, 12(9):617–628, 2000. doi: 10.1002/(SICI)1521-4095(200005)12:9⟨617::AID-ADMA617⟩3.0.CO;2-3.

[35] G.N. Greaves, A.L. Greer, R. Lakes, and T. Rouxel. Poisson's ratio and modern materials. *Nature Materials*, 10:823–837, 2011. doi: 10.1002/(SICI)1521-4095(200005)12:9⟨617::AID-ADMA617⟩3.0.CO;2-3.

[36] Y. Prawoto. Seeing auxetic materials from the mechanics point of view: A structural review on the negative poisson's ratio. *Computational Materials Science*, 58:140–153, 2012. doi: 10.1016/j.commatsci.2012.02.012.

[37] L.J. Gibson and M.F. Ashby. Cellular solids: Structure and properties. *Cambridge University Press (2nd ed.)*, 1997.

[38] K.E. Evans, M.A. Nkansah, and I.J. Hutchinson. Auxetic foams: Modelling negative poisson's ratios. *Acta Metallurgica et Materialia*, 42(4):1289–1294, 1994.

[39] J.B. Choi and R.S. Lakes. Nonlinear analysis of the poisson's ratio of negative poisson's ratio foams. *Journal of Composite Materials*, 29(1):113–128, 1995.

[40] J.B. Choi and R.S. Lakes. Analysis of elastic modulus of conventional foams and of re-entrant foam materials with a negative poisson's ratio. *International Journal of Mechanical Sciences*, 37(1):5159, 1995. doi: 10.1016/0020-7403(94)00047-N.

[41] E.G. Master and K.E. Evans. Models for the elastic deformation of honeycombs. *Composite Structures*, 35(4):403–422, 1996.

[42] N. Chan and E. Evans. Microscopic examination of the microstructure and deformation of conventional and auxetic foams. *Journal of Materials Science*, 32(21):5725–5736, 1997. doi: 10.1023/A:1018665617008.

[43] R. Blumenfeld. Auxetic strains–insight from iso-auxetic materials. *Molecular Simulation*, 31(13):867–871, 2005. doi: 10.1080/08927020500295044.

[44] Z.X. Lu, Q. Liu, and Z.Y. Yang. Predictions of young's modulus and negative poisson's ratio of auxetic foams. *physica status solidi B*, 248(1):167–174, 2011. doi: 10.1002/pssb.201046120.

[45] F. Dos Reis and J.F. Ganghoffer. Equivalent mechanical properties of auxetic lattices from discrete homogenization. *Computational Materials Science*, 51 (1):314–321, 2012. doi: 10.1016/j.commatsci.2011.07.014.

[46] M.S. Rad, Y. Prawoto, and Z. Ahmad. Analytical solution and finite element approach to the 3d re-entrant structures of auxetic materials. *Mechanics of Materials*, 74:76–87, 2014. doi: 10.1016/j.mechmat.2014.03.012.

[47] C.W. Smith, J.N. Grima, and K.E. Evans. A novel mechanism for generating auxetic behavior in reticulated foams: missing rib foam model. *Acta materialia*, 48:43494356, 2000.

[48] D. Prall and R.S. Lakes. Properties of a chiral honeycomb with a poisson's ratio of $\nu = -1$. *International Journal of Molecular Sciences*, 39(3):305–314, 1996.

[49] A. Spadoni and M. Ruzzene. Elasto-static micropolar behavior of a chiral auxectic lattice. *Journal of the Mechanics and Physics of Solids*, 60:156–171, 2011. doi: 10.1016/j.jmps.2011.09.012.

[50] X.N. Liu, G.L. Huang, and G.K. Hua. Chiral effect in plane isotropic micropolar elasticity and its application to chiral lattices. *Journal of the Mechanics and Physics of Solids*, 60(11):1907–1921, 2012. doi: 10.1016/j.jmps.2012.06.008.

[51] A. Bacigalupo and L. Gambarotta. Homogenization of periodic hexa- and tetrachiral cellular solids. *Composite Structures*, 116:461–476, 2014. doi: 10.1016/j.compstruct.2014.05.033.

[52] J.N. Grima, A. Alderson, and K.E. Evans. Auxetic behaviour from rotating rigid units. *Physica status solidi B*, 242(3):561–575, 2005. doi: 10.1002/pssb.200460376.

[53] J.N. Grima and K.E. Evans. Auxetic behaviour from rotating triangles. *Journal of Materials Science*, 41(10):3193–3196, 2005. doi: 10.1007/s10853-006-6339-8.

[54] J.N. Grima and D. Attard. Auxetic behaviour from rotating rhombi. *Physica status solidi B*, 245(11):2395–2404, 2008. doi: 10.1002/pssb.200880269.

[55] J.N. Grima, V. Zammit, R. Gatt, D. Attard, C. Caruana, and T.G.C. Bray. On the role of rotating tetrahedra for generating auxetic behavior in nat and related systems. *Journal of Non-Crystalline Solids*, 354(35-39):4214–4220, 2008. doi: 10.1016/j.jnoncrysol.2008.06.081.

[56] T. Bückmann, R. Schittny, M. Thiel, M. Kadic, G.W. Milton, and M. Wegener. On three-dimensional dilational elastic metamaterials. *New Journal of Physics*, 16(033032), 2014. doi: 10.1088/1367-2630/16/3/033032.

[57] S. Babaee, J. Shim, J.C. Weaver, N. Patel, and K. Bertoldi. 3d soft metamaterials with negative poisson's ratio. *New Journal of Physics*, 25(36): 5044–5049, 2013. doi: 10.1002/adma.201301986.

[58] R.J. Bathurst and L. Rothenburg. Micromechanical aspects of isotropic granular assemblies with linear contact interactions. *Journal of Applied Mechanics*, 55(1):1723, 1988.

[59] R.J. Bathurst and Leo Rothenburg. Note on a random isotropic granular materials with negative poissons ratio. *International Journal of Engineering Science*, 26(4):373383, 1988.

[60] K.W. Wojciechowski. Two-dimensional isotropic system with a negative poisson ratio. *Physics Letters A*, 137(1-2):60–64, 1989. doi: 10.1016/0375-9601(89)90971-7.

[61] M.A. Koenders. Constitutive properties of contacting materials with a finite-sized microstructure. *Molecular Simulation*, 31(13):873–882, 2005.

[62] N. Gaspar. A granular material with a negative poisson's ratio. *Mechanics of materials*, 42:673–677, 2010.

[63] B.D. Caddock and K.E. Evans. Micropourus materials with negative poisson's ratios: Microstructure and mechanical properties. *Journal of Physics D: Applied Physics*, 22:1877–1882, 1989.

[64] Y. Liu and H. Hu. A review on auxetic structures and polymeric materials. *Scientific Research and Essays*, 5(10):1052–1063, 2010.

[65] P.S. Theocaris, G.E. Stavroulakis, and P.D.Panagiotopoulos. Negative poisson's ratios in composites with star-shaped inclusions: a numerical homogenization approach. *Archive of Applied Mechanics*, 67(4):274–286, 1997.

[66] R.S. Lakes. Materials with structural hierarchy. *Nature*, 361:511–515, 1993.

[67] U.D. Larsen, O. Sigmund, and S. Bouwstra. Design and fabrication of compliant micromechanisms and structures with negative poisson's ratio. *Journal of Microelectromechanical Systems*, 6(2):99–106, 1997.

[68] O. Sigmund. Tailoring materials with prescribed elastic properties. *Mechanics of Materials*, 20(4):351–368, 1995. doi: 10.1016/0167-6636(94)00069-7.

[69] F. Wang, O. Sigmund, and J.S. Jensen. Design of materials with prescribed nonlinear properties. *Journal of the Mechanics and Physics of Solids*, 69(4): 156–164, 2014. doi: 10.1016/j.jmps.2014.05.003.

[70] H. Mitschke, J. Schwerdtfeger, F. Schury, M. Stingl, C. Körner, R.F. Singer, V. Robins, K. Mecke, and G.E. Schröder-Turk. Finding auxetic frameworks in periodic tessellations. *Advanced Materials*, 23:2669–2674, 2011.

[71] G.W. Milton and A.V. Cherkaev. Which elasticity tensors are realizable? *Journal of Engineering Materials and Technology*, 117(4):483–493, 1995. doi: 10.1115/1.2804743.

[72] G.W. Milton. The theory of composites. *Cambridge University Press*, 2002.

[73] G.W. Milton. Complete characterization of the macroscopic deformations of periodic unimode metamaterials of rigid bars and pivots. *Journal of the Mechanics and Physics of Solids*, 61(7):1543–1560, 2013.

[74] G.W. Milton. Adaptable nonlinear bimode metamaterials using rigid bars, pivots, and actuators. *Journal of Mechanics and Physics of Solids*, 61(7): 1561–1568, 2013.

[75] J. Patel and G.K. Ananthasuresh. A kinematic theory for radially foldable planar linkages. *International Journal of Solids and Structures*, 44(18,19): 6279–6298, 2007.

[76] Z. You and S. Pellegrino. Foldable bar structures. *International Journal of Solids and Structures*, 34(15):1825–1847, 1997. doi: 10.1016/S0020-7683(96)00125-4.

[77] C. Kittel. Introduction to solid state physics (7th ed.). *New York: John Wiley & Sons*, 1996.

[78] O. Belluzzi. Scienza delle costruzioni (11th ed.). *Vol. 1. Zanichelli, Bologna*, 1975.

[79] A.J. Wang and D.L. McDowell. In-plane stiffness and yield strength of periodic metal honeycombs. *Journal of Engineering and Manufacturing Technology*, 126(2):137–156, 2004.

[80] A.J. Wang and D.L. McDowell. Yield surfaces of various periodic metal honeycombs at intermediate relative density. *Yield surfaces of various periodic metal honeycombs at intermediate relative density*, 21(2):285–320, 2005. doi: 10.1016/j.ijplas.2003.12.002.

[81] D. Attard and J.N. Grima. A three-dimensional rotating rigid units network exhibiting negative poissons ratios. *Physica status solidi B*, 249(7):13301338, 2012. doi: 10.1002/pssb.201084223.

[82] A. Alderson and K.E. Evans. Rotation and dilation deformation mechanisms for auxetic behaviour in the α-cristobalite tetrahedral framework structure. *Physics and Chemistry of Minerals*, 28(10):711–718, 2001.

[83] A. Alderson and K.E. Evans. Molecular origin of auxetic behavior in tetrahedral framework silicates. *Physical Review Letters*, 89(225503), 2002.

[84] A. Alderson and K.E. Evans. Deformation mechanisms leading to auxetic behaviour in the α-cristobalite and α-quartz structures of both silica and germania. *Journa of physics: condensed matter*, 21(025401), 2009. doi: 10.1088/0953-8984/21/2/025401.

[85] T. Bückmann, N. Stenger, M. Kadic, J. Kaschke, A. Frölich, T. Kennerknecht, C. Eberl, M. Thiel, and M. Wegener. Tailored 3d mechanical metamaterials made by dip-in direct-laser-writing optical lithography. *Advanced Materials*, 24:27102714, 2012. doi: 0.1002/adma.201200584.

[86] T.C.T. Ting. Poisson's ratio for anisotropic elastic materials can have no bounds. *The Quarterly Journal of Mechanics and Applied Mathematics*, 58 (1):7382, 2005. doi: 10.1093/qjmamj/hbh021.

[87] A. Cazzani and M. Rovati. Extrema of young's modulus for cubic and transversely isotropic solids. *International Journal of Solids and Structures*, 40(7):17131744, 2003.

[88] A.N. Norris. Poissons ratio in cubic materials. *Proceedings of the Royal Society of London A*, 462:33853405, 2006. doi: 10.1098/rspa.2006.1726.

[89] G. Gurtner and M. Durand. Stiffest elastic networks. *Proceedings of the Royal Society of London A*, 470, 2014.

[90] T.A. Mary, J.S.O. Evans, T. Vogt, and A.W. Sleight. Negative thermal expansion from 0.3 to 1050 kelvin in zrw_2o_8r. *Science*, 272(5258):154159, 1996. doi: 10.1126/science.272.5258.90.

[91] C. Martinek and F.A. Hummel. Linear thermal expansion of three tungstates. *Journal of the American Ceramic Society*, 51(4):227–228, 1968. doi: 10.1111/j.1151-2916.1968.tb11881.x.

[92] J.S.O. Evans. Negative thermal expansion materials. *Journal of the Chemical Society, Dalton Transactions*, 19:33173326, 1999. doi: 10.1039/A904297K.

[93] P.C. Schultz and H.T. Smyth. In amorphous materials edited by r. douglas and b. ellis. *Wiley, New York*, 453-461, 1972.

[94] H.M. Kagaya and T. Soma. Compression effect on specific heat and thermal expansion of si and ge. *Solid State Communications*, 85(7):617–621, 1993.

[95] G. Hausch, R. Bacher, and J. Hartmann. Influence of thermomechanical treatment on the expansion behavior of invar and superinvar. *Physica B: Physics of Condensed Matter*, 161(1-3):22–24, 1989.

[96] R. Lakes. Cellular solid structures with unbounded thermal expansion. *Journal of Materials Science Letters*, 15:475–477, 1996.

[97] J. Lehman and R. Lakes. Stiff lattices with zero thermal expansion. *Journal of Intelligent Material Systems and Structures*, 23(11):1263–1268, 2012.

[98] G. Jefferson, Triplicane A. Parthasarathy, and R. J. Kerans. Tailorable thermal expansion hybrid structures. *International Journal of Solids and Structures*, 46:23722387, 2009.

[99] J.N. Grima, P. Farrugia, R. Gatt, and V. Zammit. A system with adjustable positive or negative thermal expansion. *Proceedings of the Royal Society of London A*, 463:15851596, 2007. doi: DOI:10.1098/rspa.2007.1841.

[100] W. Miller, D.S. Mackenzie, C.W. Smith, and K.E. Evans. A generalized scale-independent mechanism for tailoring of thermal expansivity: Positive and negative. *Mechanics of Materials*, 40:351–361, 2008. doi: doi:10.1016/j.mechmat.2007.09.004.

[101] Teik-Cheng Lim. Negative thermal expansion structures constructed from positive thermal expansion trusses. *Journal of Materials Science*, 47:368373, 2012. doi: DOI10.1007/s10853-011-5806-z.

[102] J.N. Grima, P. Farrugia, R. Gatt, and V. Zammit. Connected triangles exhibiting negative poissons ratios and negative thermal expansion. *Journal of the Physical Society of Japan*, 76(2), 2007. doi: 10.1143/JPSJ.76.02500.

[103] J.N. Grima, L. Oliveri, B. Ellul, R. Gatt, D. Attard, G. Cicala, and G. Recca. Adjustable and negative thermal expansion from multilayered systems. *Physica status solidi B*, 4:133–135, 2010. doi: 10.1002/pssr.201004076.

[104] J.N. Grima, B. Ellul, D. Attard, R. Gatt, and M. Attard. Composites with needle-like inclusions exhibiting negative thermal expansion: A preliminary investigation. *Composites Science and Technology*, 70:22482252, 2010.

[105] J. Lehman and R. Lakes. Stiff, strong zero thermal expansion lattices via the poisson effect. *Journal of Materials Research*, 29:2499–2508, 2013. doi: 10.1557/jmr.2013.154.

[106] J. Lehman and R. Lakes. Stiff, strong, zero thermal expansion lattices via material hierarchy. *Composite Structures*, 107:654–663, 2014.

[107] N.M.A. Palumbo, C.W. Smith, W. Miller, and K.E. Evans. Near-zero thermal expansivity 2-d lattice structures: Performance in terms of mass and mechanical properties. *Acta Materialia*, 59:23922403, 2011.

[108] A. Versluis, W.H. Douglas, and R.L. Sakaguchi. Thermal expansion coefficient of dental composites measured with strain gauges. *Dental Materials*, 12(5):290–294, 2009.

[109] R. Lakes. Cellular solids with tunable positive or negative thermal expansion of bounded magnitude. *Applied Physics letters*, 90(221905):475–477, 2007.

[110] O. Sigmund and S. Torquato. Composites with extremal thermal expansion coefficients. *Applied Physics Letters*, 69(21):3203–3205, 1996. doi: 10.1002/pssr.201004076.

[111] R.H. Baughman and D.S. Galvão. Crystalline networks with unusual predicted mechanical and thermal properties. *Nature*, 365(6448), 1993. doi: 10.1038/365735a0.